# SELECTIVE ENCODING THROUGH NUTATION AND FINGERPRINTING (SENF): A GRADIENT-FREE QUANTITATIVE RF ENCODING TECHNIQUE

By

Christopher Elliot Vaughn

Dissertation
Submitted to the Faculty of the
Graduate School of Vanderbilt University
In partial fulfillment of the requirements
for the degree of

DOCTOR OF PHILOSOPHY
in
Biomedical Engineering
August 9, 2024
Nashville Tennessee

Approved:
William A Grissom, Ph.D.
Mark A Griswold, Ph.D.
Mark D Does, Ph.D.
Adam W Anderson, Ph.D.
Xinqiang Yan, Ph.D

**ACKNOWLEDGEMENTS**

I would like to start by thanking my advisor, Will Grissom for his patience and support throughout my doctoral studies. I'm thankful for the opportunity to work on such an interesting project that broadened my understanding of MRI. This work would not have been possible without the countless discussions, guidance, and encouragement from Will, and for that I am grateful. Will's passion for science is infectious, and it motivates and inspires me and anyone fortunate enough to work with him. Will, thank you for your kindness and mentorship throughout the years, and I look forward to continuing to work with you.

I would like to thank Mark Griswold and Will for conceptualizing SENF and allowing me to work on its development. I thank Mark for sharing his vast knowledge and offering valuable insights whenever I encountered obstacles, without which this work would not have been possible. I would like to thank Adam Anderson, who took the time to show me around his lab and answer all my questions when I was visiting schools for undergraduate studies, helping foster my passion for science. I would also like to thank Adam for his mentorship in the classroom and as a committee member. I thank Mark Does for providing honest feedback and asking questions that help me refine my understanding of MRI. I would like to thank Xinqiang Yan for sharing his knowledge on low-field hardware.

I would like to thank Larry Wald for giving me the opportunity to work on MRI hardware and low-field systems at Martinos. Without this I would never have discovered my passion for MRI, and would not be where I am today. I thank Clarissa Cooley for her mentorship and the opportunity to help with the development of a low-field system, without which I would not be working on low-field MRI today. I would like to thank Jason Stockmann for his kindness and for his helpfulness during my time at Martinos. I would like to thank Cris LaPierre for his kindness and for mentoring me and helping involve me in so many projects at Martinos. I thank Boris Keil and Thomas Witzel for teaching me so much about MRI hardware.

I would like to thank my amazing labmates. Charlotte, thank you for being so thoughtful and helpful over the years at Martinos and Vanderbilt, and for encouraging me to join the lab. Abitha, I'm thankful to have had someone to work on the low-field scanner with, and thank you for all the enjoyable conversations. Jonathan, thank you for encouraging me to join the lab and all the interesting projects and conversations. I would like to thank Matt for his help with hardware design and working with me on interesting projects. I want to thank Huiwen, Madison, Antonio, Sarah and Kristen for making the lab a friendly and enjoyable place. I would also like to thank Jessie Sun for her invaluable help with writing my dissertation.

Lastly I would like to thank my parents and grandparents for their unconditional love and support, without which I would never have made it to where I am today. Dad, thank you for always pushing me to do bigger and better things, and supporting me all the way. Mom, thank you for all your love and for nurturing me. I want to thank my brother for his encouragement and friendship. I want to thank my grandfather for all his advice and guidance throughout my life, and I know he would be proud of where I am today.

Christopher Elliot Vaughn

## TABLE OF CONTENTS

## LIST OF FIGURES

# CHAPTER 1: INTRODUCTION

## 1.1 Overview of Conventional MRI

Medical imaging allows for the detection and diagnosis and monitoring of disease inside the human body that likely would otherwise not be discovered. Without medical imaging, physicians relied on a physical examination (using the human senses of sight, smell, hearing and touch) as well as chemical and cellular analysis of blood and tissues to arrive at a disease diagnosis. While such examinations can provide important information for the detection and diagnosis of disease, these approaches can, at best, only give a partial picture of the scope and extent of the disease process in a patient. For example, visual examination of a patient was limited to the surface of the body, just using their eyes and the visible light spectrum. On the other hand, using other forms of radiation, one can interrogate tissues within the body to enhance the accuracy, precision of a diagnosis and the extent of a disease process. Some examples of the use of different types of radiation include: high energy electromagnetic radiation for X-ray and CT for diagnosing broken bones and stroke (Bercovich, 2018); ultrasonic radiation for ultrasound used for imaging vascular structures of tumors (Bercovich, 2018) or monitoring fetal development (Whitworth et al., 2015); positron emissions for Positron Emission Tomography (PET) for monitoring elevated metabolism in tumors (Bercovich, 2018). Such medical imaging modalities have many other applications (Kasban et al., 2015) and also have important limitations. For example, the high energy electromagnetic radiation used for X-ray and CT and positrons for PET emits ionizing radiation that damages DNA with potentially carcinogenic effects (Burgio et al., 2018), especially with repeated or prolonged use. Ultrasound has limited penetration depth, making imaging of deeper structures difficult, especially in obese and muscular patients (Lento, 2008). Additionally, some medical imaging is limited by the nature of the human anatomy, as is seen

when the skull distorts ultrasonic radiation (Riss et al., 2022), making imaging of the brain with ultrasound difficult. With cancer being the second highest cause of death in the US, as reported by the American Cancer Society (American Cancer Society, 2022), and the obesity rate in the US at 42.4%, as reported by the NIH (NIH, 2021), a non-invasive imaging modality with high resolution and imaging depth, as well as excellent soft-tissue contrast, is needed. Magnetic resonance imaging (MRI) addresses these needs.

MRI is a non-invasive imaging modality that uses static and radiofrequency (RF) electromagnetic fields to stimulate protons within the human body, that can then be imaged as the protons return to equilibrium. These static magnetic fields and RF fields easily permeate throughout the body with minimal attenuation, allowing for high resolution imaging at any depth, even within the brain. An MRI scanner consists of a main magnetic field, which is what is responsible for establishing a net-polarized equilibrium condition. Radiofrequency (RF) coils are used to transmit radio waves that stimulate these protons out of equilibrium and subsequently receive the signals from these protons through Faraday induction. Finally, gradient coils are used to produce linear changes in the main magnetic field, causing the precession frequency of the protons to vary across space, enabling spatial encoding and image reconstruction with the Fourier transform.

The human body is made up of 60% water and MRI images the protons present in this water within a variety of tissues. The signals created by these protons have different behaviors, depending on the tissue in which they are present. These properties include $T_1$ relaxation, which is the rate at which the protons return to equilibrium, and $T_2$ relaxation, which is the rate at which spins dephase due to interactions between spins. Adjusting timings within an MRI sequence, such as the echo time (TE), which is the time between the excitation RF pulse and a signal echo,

or repetition time (TR), which is the time between excitation RF pulses, generates contrast in the final image, related to the $T_1$ and $T_2$ relaxation times (Preston, 2016). $T_1$ weighted imaging is useful for diagnosing diseases with changes to water content or other molecular changes, such as fibrosis within the heart or liver (Serai, 2022). $T_2^*$ relaxation refers to the rate at which spins dephase due to spin-spin interactions ($T_2$), as well as macroscopic magnetic field inhomogeneities, like field distortions caused by iron in deoxyhemoglobin, and can be used to create contrast for measuring things like iron content in the liver (Serai, 2022). Functional MRI (fMRI) uses blood oxygen level dependent (BOLD) contrast, which is produced by changes in the relative concentrations of oxyhemoglobin and deoxyhemoglobin, which then lead to changes in $T_2$* that depend on brain metabolism as a proxy for neural activity. Diffusion of water within the tissues can be leveraged to produce contrast within the image using a gradient field to dephase protons, producing lower signal levels in locations with higher diffusion coefficients. This is useful in diagnosing diseased tissues that would have changes to the tissues' diffusion coefficients, such as what occurs in ischemic stroke (Preston, 2016). Many other clinical applications of MRI related to the diagnosis of conditions affecting soft tissues like those mentioned previously have been realized within the brain, lungs, liver, prostate, breast and musculoskeletal system. However, MRI is not without its limitations.

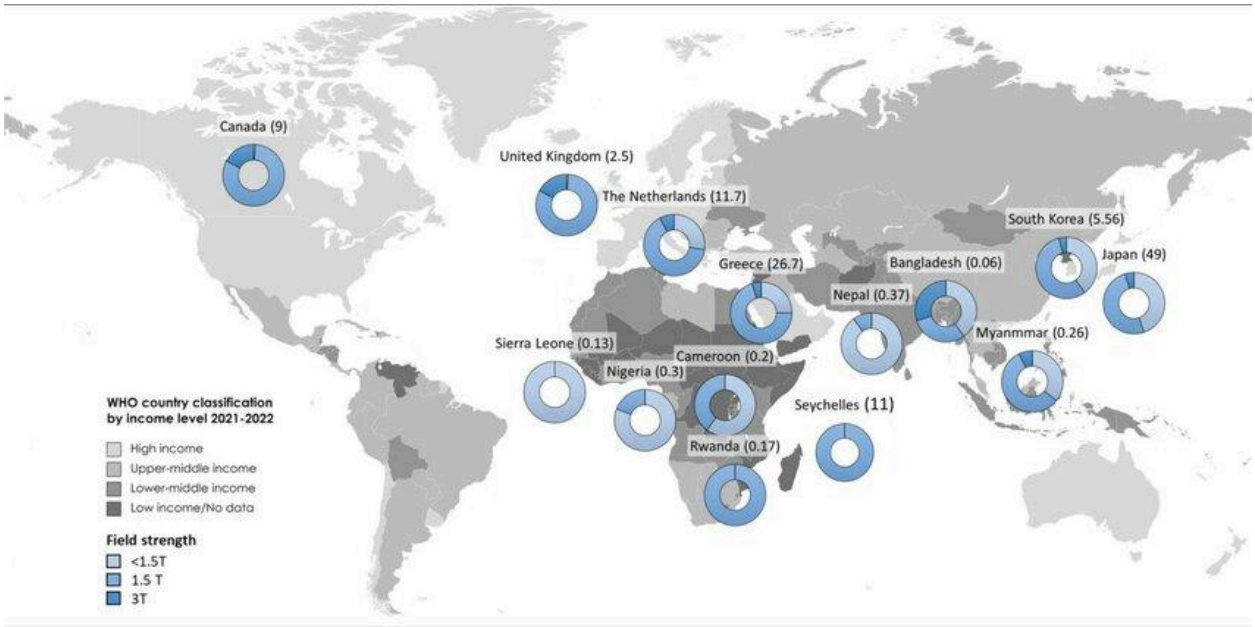


Figure 1.1: Figure from Jimeno et. al, depicting the distribution of MRI scanner field strengths across the world. The grayscale indicates the WHO country classification by income level. The blue wheel indicates the proportion of different scanner strengths within the country. The number in parenthesis is the number of MRI scanners per 1 million inhabitants.

Some major limitations of MRI are its availability, size and cost. Clinical MRI scanners have field strengths that range from 1-3 Tesla (T) with a cost of around $1 million per Tesla (Sarracanie et al., 2015). The strong magnetic fields require the scanner to be sited far from surrounding equipment to prevent interference and potential safety hazards. Specifically, all ferromagnetic objects will be accelerated toward the scanner center, if the objects are brought within the 5-Gauss exclusion zone. An area that can extend several feet or more from the magnet itself, depending on the magnet's field strength and shielding. Also, an MRI scanner requires an RF-shielded room to prevent interference from outside signals. Consequently, MRI scanners require significant dedicated and separated facility space. Additionally, most main field magnets are made of superconducting materials that need to be kept cool with liquid helium. All of these

factors make the cost and availability of MRI prohibitive to any non-hospital setting, such as out-patient clinics, low resource areas or military applications (Cooley et al., 2015). These limitations to accessibility of MRI can be addressed to a large extent, with low-field MRI.

## 1.2 Low-Field MRI Motivation

### 1.2.1 Accessibility

Despite the diagnostic power of MRI, and the health benefits of its widespread use, MRI has poor accessibility. Improved accessibility of MRI could enable the earlier detection of cancer and other diseases, which have greatly improved outcomes with early detection, this topic will be discussed further in the clinical applications section. Higher-income countries have one MRI scanner for every 25,000 people while other countries have a 50-times smaller scanner-per capita ratio (Ogbole et al., 2018). Furthermore, MRI scanner systems are typically limited to urban areas. Biases also appear in neuroimaging initiatives towards higher education socioeconomic demographics (Fry et al., 2017; Garavan et al., 2018; Smith, 2018; Deoni et al., 2022), making them less relevant towards the general population. MRI's vast use cases make it a vital imaging modality for diagnosis and treatment monitoring, and making MRI more accessible has a clear benefit for patients. The next two sections will discuss low-field MRI's unique ability to overcome the portability and cost limitations of conventional MRI.

#### 1.2.1.1 Portability

Making MRI portable helps bring scanners to areas with low accessibility to MRI, like low- or mid-income countries and non-urban settings. The main hindrance to portability is the siting requirements of a conventional MRI scanner. The field strength of the main magnetic field is the

first major concern. The 5 Gauss exclusion zone is the area around the scanner with field strengths greater than 5 Gauss. Within this exclusion zone, ferromagnetic material is at risk of becoming a projectile, and implanted devices such as a pacemaker may have hindered functionality (Mittendorff et al., 2022). These risks can be mitigated with magnetic shielding (Whelan et al., 2018); however, the 5 Gauss exclusion zone also reduces in size with low-field MRI due to the overall reduction in field strength. This means low-field scanners can be more easily placed in proximity to other medical equipment and ferromagnetic objects.

In addition, the materials used for the main magnet are a hindrance to portability. Typical magnets for MRI are made of superconducting materials. These materials must be kept cool with liquid helium to maintain a low resistance, in order to sustain the magnetic field created by the current flowing through the superconductor. On the other hand, low-field magnets can be constructed using permanent magnets made from special alloys that are ferromagnetic and several alloys of rare-earth metals (Cooley et al., 2015; Deoni et al., 2022). These magnets have a persistent magnetic field and do not require a flowing current or liquid cooling.

Another siting requirement of a conventional MRI scanner is the shielded room to mitigate electromagnetic interference (EMI). If EMI is not mitigated, artifacts appear within the image, such as overall SNR reduction or banding (Whelan et al., 2018), that make images harder to interpret. Low-field scanners additionally have lower SNR due to weaker polarization and weaker Faraday induction, which will be discussed in Chapter 2. Therefore at low-field strengths it is necessary to use several methods for noise mitigation that also reduces the need for shielded rooms. Local shielding can be used within the scanner to mitigate noise. This could be Electromagnetic Interference (EMI) shielding placed around the main magnet itself or around the patient. The patient is either shielded within the main magnet by surrounding shielding or by

local shielding within, if it is an open magnet design. Copper sheets or other flexible shielding can be used in addition to rigid local shielding. Using gradiometer coil geometries mitigates noise by constructing the detector coil, such that uniform fields including distant interference fields are self-canceled within the coil itself (Seton et al., 2022). Active EMI suppression can be used alongside the passive shielding. Active shielding typically uses EMI detectors such as RF coils placed around the scanner, which are used to detect noise. A pre-calibration technique can be used to measure noise before a scan and that noise can be removed from the data in post-processing. This method is insensitive to EMI fluctuations during the scan. These fluctuations can be better addressed with dynamic methods, such as EDITER (Srinivas et al., 2022), which simultaneously acquires data during regular acquisition windows on the EMI detectors to remove noise in post-processing. Low-field scanners have several solutions to the

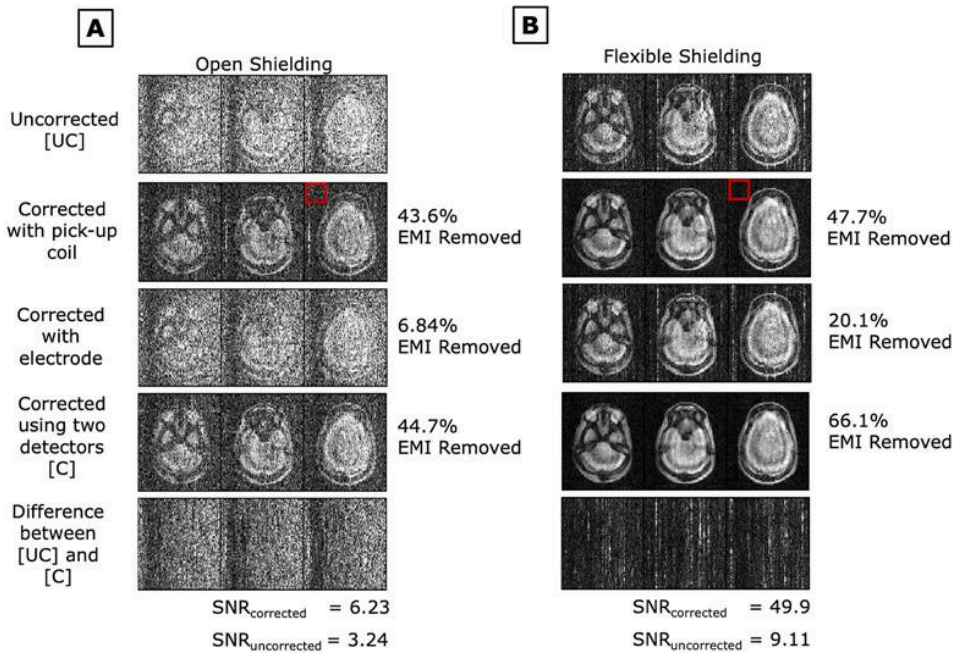


Figure 1.2: From Srinivas et. al, showing EMI reduction and SNR improvements using EDITER for head phantom images on a 47.5 mT scanner using A) open rigid local EMI shielding and B) flexible EMI shielding. The region of interest outlined in red was used to measure the standard deviation of EMI in the images to determine the percent EMI removed.

typical siting restrictions of conventional MRI. Eliminating these siting requirements facilitates the portability of the scanner allowing for use in non-hospital settings, including military, sports or low-resource environments.

#### 1.2.1.2 Cost

Conventional MRI systems cost $1.5-$3 million dollars (Sarracanie et al., 2015) due to the siting requirements for the scanner and the scanner cost itself. As explained in the previous section, low-field scanners minimize or eliminate the siting requirements that plague conventional MRI. Constructing these systems with permanent magnets and no special siting requirements lowers the cost of the scanner to between tens of thousands to hundreds of thousands of dollars (Cooley et al., 2015). Examples of this are the Hyperfine bedside scanner that costs a few hundred thousand dollars (Deoni et al., 2022) to purchase. The combination of the lower cost and portability makes low-field scanners ideal for improving MRI accessibility.

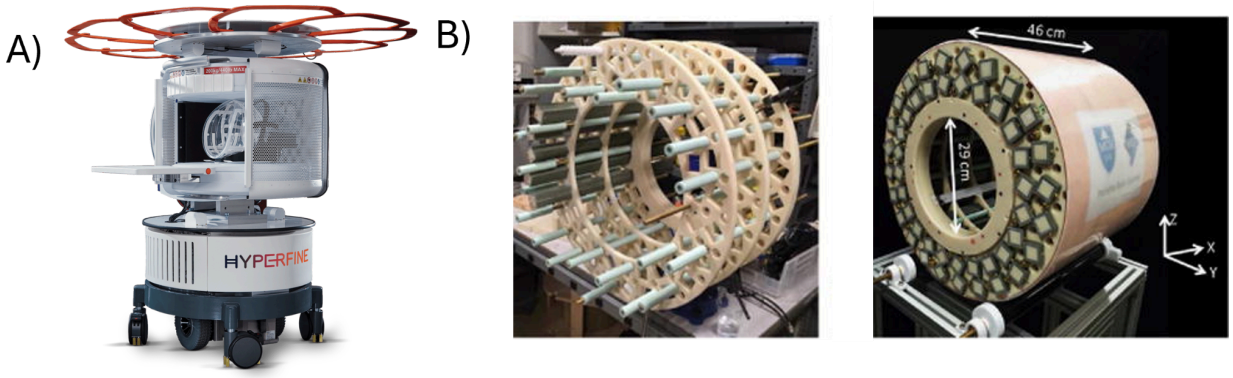


Figure 1.3: A) Wheeled Hyperfine 64 mT portable scanner. B) MGH 80 mT Halbach magnet, 46 cm in length weighing <100 kg on a wheeled chart.

### 1.2.2 Specific Absorption Rate (SAR)

Specific absorption rate (SAR) is a metric of RF power deposition in Watts per kilogram (W/kg) of tissue. The RF fields used to excite protons in MRI generate electrical currents in tissues within the body which convert to heat in the resistive tissue. This heating can cause permanent damage to the tissue, especially in areas of the body that cannot dissipate heat quickly, like the eyes, or organs more sensitive to temperature, like the brain. The International Electrotechnical Commission (IEC) and the US Food and Drug Administration (FDA) place limits on SAR; the FDA limits SAR to 4 W/kg for the whole body averaged over 15 minutes and 3 W/kg for the head averaged over 10 minutes (FDA, 1998). SAR in a continuous irradiation mode is calculated with the following formula:

$$SAR = \frac{\sigma|E|^2}{\rho}, \tag{1.1}$$

where $\sigma$ is the electrical conductivity of the tissue, $\varrho$ is the density of the tissue and $E$ is the electric field. The $E$ field is related to the time derivative of the magnetic field by the Maxwell-Faraday equation. In the Fourier domain the time-varying $B_1$ field can be described by a phasor with the magnitude of the $B_1$ field, oscillating at frequency ω. Therefore, $E$ scales with the product of ω and $|B_1|$. The RF frequency used for the SAR calculation is the Larmor frequency, due to the narrow bandwidth of frequencies used for MRI. The Larmor frequency is proportional to the $B_0$ field strength,

$$\omega = \gamma B_0, \tag{1.2}$$

where γ is the gyromagnetic ratio. Therefore, SAR is proportional to the field strength squared.

SAR limits are addressed with sequence design by reducing RF power and the transmit duty cycle. Techniques such as RF encoding and sequences with high RF duty cycles such as turbo spin echo pose SAR concerns that are typically addressed by minimizing power (e.g., by

reducing flip angles in refocusing trains) and increasing scan time to reduce the duty cycle. However, low-field scanners can implement sequences and techniques with high RF power or duty cycle requirements, without reaching SAR limits, due to SAR varying with the square of $B_0$

.

### 1.2.3 Clinical Applications

$T_1$ and $T_2$ relaxation rates converge at lower field strengths, resulting in lower contrast levels between tissues, making low-field less suitable for brain applications like cancer imaging. Low-field is more suited to imaging pathologies, where $T_1$ and $T_2$ relaxation rates vary significantly between healthy tissues and diseased tissues. Examples include diagnosis of acute diseases such as stroke, hemorrhage, or edema, where changes in intracellular and extracellular fluid content significantly alter $T_1$ and $T_2$. Strokes have an annual mortality rate of 6.5 million annually worldwide (Feigin et al., 2017). Patients with these diseases are typically too ill to be safely transported to an imaging suite for the current standard of care CT and high-field MRI. The ability for low-field MRI to be used as a point-of-care imaging modality reduces the risk of moving the patient and the time it takes to diagnose the stroke as either ischemic or hemorrhagic. This is vital as the treatment for one would result in death for the other. The faster the correct treatment is administered, the better the patient outcome (Nogueira et al., 2018). Low-field MRI has been applied to this problem with 97% accuracy for stroke detection (Sheth et al., 2020). Mobile stroke units using an ambulance CT scanner (Parker et al., 2015) have been deployed to drastically reduce diagnosis time. These could feasibly be replaced with mobile low-field MRI systems (Deoni et al., 2022) in the future.

The improved accessibility of low-field MRI has also been leveraged for outpatient neuro-imaging. Multiple sclerosis (MS) is a disease that results in the demyelination of neurons

in the brain affecting nearly 2.5 million people globally (Tullman, 2013). Early detection of MS can help with delayed disease progression and reduced severity (Noyes, 2013). Early detection could be enhanced by increasing accessibility to diagnosis using low-field MRI. The detection of multiple sclerosis lesions has been done using the 64mT Hyperfine system with 94% accuracy (Mateen et al., 2021; Arnold et al., 2022). Another use of neuro-imaging at low-field is the detection of hydrocephalus, the abnormal enlargement of the ventricles in the brain that carry cerebral spinal fluid (CSF). This is diagnosed by imaging the increased ventricle size, which has been accurately performed on the 64mT Hyperfine scanner (Arnold et al., 2023).

Prostate cancer is the second most deadly cancer type in men worldwide (Bray et al., 2018). Prostate imaging can be done at low-field strengths to view tumors or other abnormalities intraoperatively to assist in biopsies and resections. Promaxo has developed a prostate MRI system for intraoperative procedures using a single-sided low-field magnet with a built in gradient (Nasri et al., 2021; Chiragzada et al., 2021). This system has 510k clearance and insurance reimbursement, as a replacement for ultrasound-MR fusion for guided biopsies with a full MR protocol. The low-field Promaxo system replaces the endorectal ultrasound probe with an external MRI system for surgical guidance. This system has the advantage of registering MRI images together rather than registering images gathered by different imaging modalities, providing improved accuracy in registration, translating to better-targeted biopsies.

Low-field MRI also excels at pediatric and neonatal imaging. Point-of-care imaging helps reduce patient risk by alleviating the need to transport patients to imaging suites, which is especially useful for neonatal patients, where the standard of care is CT and high-field MRI (Wood et al., 2021). Ultrasound is a point-of-care imaging modality used in pediatric and neonatal imaging, but has worse contrast and resolution when compared to CT and MRI. Aspect

Imaging developed the Embrace Neonatal MRI system, used for point-of-care imaging of congenital anomalies and developmental disorders (Thiim et al., 2022). The ability to create open scanner designs, as well as reduced auditory noise, also helps with pediatric patient compliance, reducing the need for sedation (Raschle et al., 2012). There is also potential for outpatient pediatric imaging with increased accessibility, as demonstrated by the use of the 64mT Hyperfine scanner to track neurodevelopment in children (Deoni et al., 2021).

With improvements to low-field MRI, interest in its use for orthopedic and musculoskeletal imaging continues to increase because of its ability to image in the presence of metallic implants, which would otherwise cause image artifacts of safety issues in high-field MRI. Flexible magnet design can allow for imaging in more comfortable and diagnostically relevant positions, such as upright spinal imaging (Baker, 2020). However, limitations due to reduced image quality from lower SNR and resolution at low-field are still an issue for orthopedic imaging, as well as reduced soft tissue contrast. A study has been performed with the 64mT Hyperfine scanner for knee imaging that shows some promise in imaging certain tendons and ligaments (Watchmaker et al., 2022). Additionally, the reduced chemical shift and reduced relaxation rate differences between fat and water make fat suppression at low-field challenging, which is common practice for orthopedic imaging (Guerini et al., 2015).

Breast cancer is the leading cause of cancer death in women worldwide (Ferlay et al., 2020). The current standard of care is mammography, which uses ionizing radiation. Ultrasound and MRI are alternative imaging modalities, however they suffer from accuracy and accessibility, similarly to previous imaging applications. Nevertheless, the improved accessibility of low-field MRI has the potential to be used as a breast cancer screening tool. Reduced susceptibility effects at low-field strengths, again, enable image guided biopsies (Pääkkö et al.,

2005). Although limitations in spatial resolution at low-field strengths limit the detection of small lesions in breast cancer imaging, a study by Dean et al has been done evaluating ultra low-field breast tumor imaging at 0.02 Tesla, where 19 out of 23 carcinomas detected by mammography were also detected by MRI (83% sensitivity) and only one in four benign cases were identified as pathologies (75% sensitivity) (Dean, 1994).

### 1.2.4 Weaknesses of low-field MRI and potential mitigation strategies

Low-field MRI has some distinct differences from high-field MRI, some of which are disadvantages that can be mitigated and some advantages to be leveraged. Shorter $T_1$'s allow for shorter repetition times (TR) and the longer $T_2$'s allow for longer echo trains, both of which can be leveraged to gather more data quickly for averaging to alleviate the reduction in SNR (Arnold et al., 2023). However, this means $T_1$ and $T_2$ relaxation times will become similar, causing the loss of some contrast in tissues, for example white and gray matter in the brain. This reduction in contrast can make diagnosis of certain diseases more difficult, for example demyelination from multiple sclerosis (MS) with reduced contrast between white and gray matter. Lower $B_0$ field strengths have weaker polarization, meaning fewer spins are aligned or anti-aligned with the $B_0$ field, resulting in lower NMR signal levels. The lower $B_0$ field strengths also result in lower electromotive force by the spins onto a receive coil via Faraday induction. The rate at which the magnetic flux through the coil is changing is slower, due to the smaller Larmor frequency. These concepts will be covered further in Chapter 2.

Deep learning has also been used for low-field MRI reconstruction to help reduce noise in the k-space data and improve image SNR (Zhu et al., 2018). Hyperpolarized imaging is done by increasing the polarization of an endogenous molecule like $^{13}$C-pyruvate, far beyond typical

thermal equilibrium of hydrogen typically imaged in MRI at low-field strengths. This is on the order of 20-40% polarization versus the 0.0003% polarization of hydrogen per Tesla at room temperature (Miloushev et al., 2016). This results in, not only much higher SNR, but also, the ability to image metabolism, allowing tumor imaging at low-field strengths (Miloushev et al., 2016). The main downside of this is the hyperpolarization is transient on the order of 20-30 seconds requiring efficient imaging techniques (Zaccagna et al., 2018), and the additional hardware required to hyperpolarize the agent. Low-field MRI has reduced susceptibility effects allowing for imaging of patients with metal implants such as cochlear implants or aneurysm clips that produce significant image artifacts or pose significant risk to the patient at higher field strengths (Hori et al., 2021).

### 1.2.5 Introduction to SENF

As low-field MRI increases accessibility to MRI, its usability must also become more accessible. If MRI only produces contrast-weighted images that require trained radiologists to interpret and make diagnoses from, it would limit the impact the improved accessibility has on health outcomes. Quantitative MRI aims to produce objective measures through parameters such as $T_1$, $T_2$, $T_2^*$, apparent diffusion coefficient (ADC), and susceptibility to provide objective quantitative data of the tissues being imaged. Magnetic Resonance Fingerprinting (MRF) takes this a step further, by collecting a single data set from which multiple parametric maps can be reconstructed simultaneously (Ma et al., 2013). Having multiple quantitative parameters provides objective measurements allowing for diagnosis of diseased tissues to be less subjective and more consistent. These fingerprints have been shown to be robust between multiple scanners and data sets (Dupuis et al., 2024).

This thesis proposes the Selective Encoding through Nutation and Fingerprinting (SENF) method. SENF is a fundamentally new way to encode MRI data, that like MRF measures multiple quantitative parameters simultaneously, while also performing spatial encoding through RF gradient methods. SENF could remove the need for $B_0$ gradients, allowing for low-cost systems to be built that do not require $B_0$ gradient amplifiers, coils or cooling systems, while improving patient comfort by removing auditory noise produced by gradients during switching due to Lorentz forces. SENF can be used with a wide variety of $B_1$ fields, which allows for flexibility in scanner design. As a quantitative imaging method, SENF could provide more objective and consistent metrics for identifying diseased tissues than conventional contrast imaging. SENF, like MRF, could be more time-efficient than the multiple image acquisitions required for conventional quantitative MRI.

SENF has four core components: an inhomogeneous $B_1$ field, pulses that create $B_1$-dependent effects, an MRF-type sequence and a dictionary reconstruction that simultaneously extracts quantitative and spatial information. The inhomogeneous $B_1$ field can be produced by existing RF coils, such as a parallel transmit (pTx) array, and pulses can be transmitted through the RF coil that create $B_1$-dependent amplitude and phase effects on the magnetization of the spins. Using a set of pulses with varying $B_1$-dependent effects creates a set spatially dependent amplitude or phase effects that are used as spatial encoding patterns. Implementing these pulses within an MRF-type sequence causes magnetization from adjacent spins to quickly become incoherent, creating unique signals for different spatial locations and quantitative parameters. A Bloch simulation is performed to produce all possible signals over a range of spatial locations and quantitative parameters, and these signals are used to populate a signal dictionary. A regularized pseudoinverse is taken from this dictionary and applied to a combined measured

signal to produce coefficients for each unique spatial location and quantitative parameter combination. The largest coefficients for each quantitative parameter combination at each spatial location are taken, and that material is designated to that spatial location, with the exception of coefficients that do not surpass a threshold, which are rejected and the spatial location is designated as air. Using prior knowledge of the materials quantitative parameters, multiple quantitative parametric maps are then constructed simultaneously from the single combined measured data.

The goal of SENF is to provide a method like MRF that can create multiple parametric maps simultaneously, that can be implemented on low-cost low-field MRI systems with improved accessibility. SENF aims to combines objective, easily interpretable results and improved accessibility of low-field MRI to further improve health outcomes.

### 1.3 Thesis Outline

This section is an overview of the structure and aims of this dissertation.

*Chapter 2: Background and Significance*

Chapter 2 provides relevant background for Selective Encoding through Nutation and Fingerprinting (SENF) and its significance as a quantitative and gradient-free imaging method. This chapter provides: 1) a background on the physics underpinning MR imaging; 2) a discussion of RF hardware and the considerations needed for high and low-field strengths, with an overview of parallel imaging and parallel transmit arrays; 3) a review of conventional quantitative MRI sequences and how they encode their respective parameters along with a review of Magnetic Resonance Fingerprinting (MRF) and its clinical applications; and 4) an overview of current RF encoding techniques differentiated by $B_1$ amplitude and phase methods; 6) a section on how SENF capitalizes on these techniques.

*Chapter 3: Selective Encoding through Nutation and Fingerprinting (SENF)*

Chapter 3 introduces and validates SENF as a gradient-free quantitative MRI imaging technique and compares three different SENF sequences. Chapter 3 provides: 1) an introduction to SENF and its components that enable simultaneous spatial and quantitative encoding, along with three distinct pulse sequence embodiments we have developed; 2) a 2D feasibility simulation which serves to validate the basic function of the method in a digital brain slice phantom; and 3) a comparison of the advantages and disadvantages among the three SENF sequences in simulation with each other and with conventional $T_1$ and $T_2$ mapping. The quantitative comparisons made will be minimum SNR and resolution.

*Chapter 4: Hardware Design for Experimental Validation of SENF on a 47.5 mT Low-Field Scanner*

Chapter 4 describes a complete RF transmit and receive system for experimental implementation of 1D SENF on a 47.5 mT low-field scanner. The chapter covers: 1) the development of EMI shielding for SENF experiments for noise reduction and facilitation of experimental protocol; 2) the designs of a loop and variable pitch solenoid used for $B_1^+$-selective pulse experiments on the low-field scanner; and 3) the design and optimization of an RF solenoid with variable winding density to transmit. The solenoid includes a nested saddle coil to receive, as well as a former and holders that position the coils and phantoms for the first SENF experiments on a 47.5 mT scanner.

*Chapter 5: Implementation of SENF on a 47.5 mT Low-Field Scanner*

Chapter 5 is a case-study of the practical implementation of SENF on a 47.5 mT low-field scanner. This chapter includes: 1) The implementation of the $B_1^+$-selective pulses on a 47.5 mT low-field scanner, starting with verification of a $B_1^+$-selective pulse excitation profile, then using

$B_1^+$-selective pulses with $B_0$ gradients for 3D imaging, and finally a 1D experiment using $B_1^+$-selective pulses for spatial encoding with a dictionary based reconstruction. Limitations of the implementation of this SENF sequence due to RF fidelity are also discussed; 2) the implementation of the hard pulse-based SENF sequence, including 1D two material SENF experiments.; 3) Discussion of the limitations of optimizing the spatial and quantitative independently; 4) the implementation of the quadratic phase Bloch-Siegert (qRF-BS) SENF sequence is reported first showing the ability to independently adjust spatial and quantitative encoding; and 5) a single material 1D SENF experiment is shown.

*Chapter 6: Contributions and Future Work*

Chapter 6 discusses the contributions of SENF, a discussion of future SENF experiments and potential clinical applications of SENF. Hardware development of amplifiers with improved RF fidelity and simultaneous receive will facilitate 2D SENF imaging using the $B_1^+$-Selective sequence on a forthcoming 0.1 T scanner. Improvements will also be made to all three SENF sequences in terms of their encoding power and experimental implementation.

# CHAPTER 2: BACKGROUND AND SIGNIFICANCE

## 2.1 Discussion: Building up to SENF

Selective Encoding through Nutation and Fingerprinting (SENF) draws on the different background sections discussed in this chapter. SENF is a $B_0$ gradient-free RF encoding technique that simultaneously encodes spatial and quantitative information. Current RF encoding techniques as well as $B_o$ gradient encoding were discussed in this chapter to provide background on existing encoding techniques. Conventional qMRI and MRF were discussed to provide background on existing quantitative encoding techniques. SENF builds on MRF in the sense that they both use varying sequence parameters, such as flip angle and TR, to encode information into the signals, making the signals unique for different tissues. SENF, however, takes this a step further by using RF gradient encoding techniques to encode spatial information into the signals as well. The hardware section discussed relevant RF coil components that are used for experimental coils developed in Chapter 4, as well as pTx arrays and parallel imaging which are used in a proof of concept simulation in Chapter 3. The differences between low-field and high-field MRI in terms of hardware considerations were discussed to provide context for the experimental implementation of SENF on a low-field system, beyond motivations discussed in Chapter 1.

## 2.2 MRI Physics

Magnetic Resonance Imaging (MRI) has three main components: a static magnetic field ($B_0$), a radiofrequency field ($B_1$), and gradient magnetic fields ($\vec{G} \cdot \vec{x}$). Using the principle of nuclear magnetic resonance (NMR) these three components, along with the Fourier Transform, allow for

image reconstruction. This section will provide a brief overview of the basic physics of these three components and the simplest image reconstruction technique.

### 2.2.1 $B_0$ Field

When protons are placed within a static magnetic field, they will align or anti-align with that field. As the strength of the $B_0$ field increases, more protons will align with the field. The more protons that align with the field, the greater the net magnetization ($M_0$). Therefore, the $M_0$ of the protons increases with $B_0$ field strength,

$$\frac{N^+}{N^-} = e^{-E/kT}, \tag{2.1}$$

where $N^+$ are the aligned spins and $N^-$ are anti-aligned spins, $E$ is the energy level between the spin states, $k$ is the Boltzmann constant and $T$ is the temperature. This ratio of spin states is representative of the net magnetization $M_0$. A stronger $B_0$ field increases the energy level ($E$) between the spins states, resulting in stronger net magnetization ($M_0$). Within the $B_0$ field, the protons precess at the Larmor frequency, which is proportional to the $B_0$ field strength and the gyromagnetic ratio γ of a proton (Eq. 1.2).

Increasing precession frequency with increasing $B_0$ field strengths result in larger electromotive force (ε) by the spins onto a multi-turn coil, due to the increased rate of change of magnetic flux ($\frac{\Delta\Phi}{\Delta t}$), by Faraday's Law,

$$\varepsilon = -N\frac{\Delta\Phi}{\Delta t}, \tag{2.2}$$

where $N$ is the number of wire loops through which the magnetic flux passes. Therefore, signal strength increases with $B_0$ both due to increased polarization ($M_0$) and increased Faraday induction.

### 2.2.2 RF Transmit and Receive

Nuclear magnetic resonance (NMR) is the principle used for signal generation in MRI. A radiofrequency (RF) field $B_1^+$ is transmitted through a resonant coil in the transverse (xy) plane, perpendicular to the $B_0$ field (z). The frequency of this field is set to the Larmor frequency of the proton, which allows the $B_1^+$ field to flip the proton out of alignment with the $B_0$ field at an angle, known as the flip angle (Eq. 2.3).

$$\alpha = \gamma B_1 t \tag{2.3}$$

The net magnetization following the application of the $B_1^+$ field can be solved with the Bloch Equations, simplified by a rotating frame of reference at the Larmor frequency.

$$\frac{d}{dt}\begin{bmatrix} M_x' \\ M_y' \\ M_z' \end{bmatrix} = \begin{bmatrix} -\frac{1}{T_2} & \Delta & -\varepsilon \\ -\Delta & -\frac{1}{T_2} & \varepsilon \\ -\varepsilon & -\varepsilon & -\frac{1}{T_1} \end{bmatrix} \begin{bmatrix} M_x' \\ M_y' \\ M_z' \end{bmatrix} + \begin{bmatrix} 0 \\ 0 \\ \frac{M_0}{T_1} \end{bmatrix}$$

$$\varepsilon = \gamma B_1 \text{ and } \Delta = \gamma B_0 - \omega \tag{2.4}$$

If the frequency of the $B_1$ field is off-resonant from the Larmor frequency, the spin's precession frequency is shifted. This phenomenon is known as the Bloch-Siegert shift. Transmitting a pulse of amplitude $\omega_{B1}$ with an off-resonance of $\Delta\omega_{RF}$ causes spins to accrue phase $\varphi_{BS}$.

$$\varphi_{BS} = \int_0^\tau \omega_{BS}(t)\, dt = \int_0^\tau \frac{\omega_{B1}^2}{2\Delta\omega_{RF}(t)}\, dt \tag{2.5}$$

A resonant coil that has a $B_1^-$ receive field is aligned perpendicular to the $B_0$ field. Once the proton is flipped out of alignment with the $B_0$ field, its precession causes the resonant coil to experience a changing magnetic field, inducing a current in the coil due to Faraday induction. This current produces the signal that is acquired and used for image reconstruction.

### 2.2.3 Spatial Encoding with Gradient Fields

Linearly varying magnetic fields, known as gradient fields, are used for spatially encoding signals in MRI. As shown in Equation 1.2, the precession frequency of the proton is proportional to the strength of the static magnetic field $B_0$. Gradient fields are used to intentionally vary the strength of the magnetic field linearly along three orthogonal directions (*x, y, z*) to create varying precession frequencies across space (Eq. 2.6), which establishes a one-to-one mapping between temporal frequency and spatial location, enabling the localization of the signal at a spatial location based on its frequency.

$$\omega = \gamma|B_0 + B_0(r)\ | \tag{2.6}$$

The signal equation for a particular position and gradients ($G_x$, $G_y$, $G_z$) with durations ($t$, $\tau$, $\xi$) is,

$$S(G_x, G_y, G_z) = \int\int\int \rho(x,y,z) e^{-i\gamma G_x t} e^{-i\gamma G_y \tau} e^{-i\gamma G_z \xi} dxdydz \tag{2.7}$$

This can be rewritten with $k_x$, $k_y$, $k_z$ to allow for the data to be assigned to k-space, a domain used for simpler image reconstruction,

$$S(k_x, k_y, k_z) = \int\int\int \rho(x,y,z) e^{-2\pi i k_x x} e^{-2\pi i k_y y} e^{-2\pi i k_z z} dxdydz \tag{2.8}$$

$$k_x = \frac{\gamma}{2\pi} G_x t; k_y = \frac{\gamma}{2\pi} G_y \tau; k_z = \frac{\gamma}{2\pi} G_z \xi \tag{2.9}$$

These equations are for phase encoding gradients. For frequency encoding gradients, the dwell time of each sample for the acquisition is used, instead of the entire duration of the gradient.

For cartesian k-space sampling, two conventional $B_0$ gradient encoding methods are phase encoding and frequency encoding. A frequency encoding gradient is pulsed during an acquisition window, allowing for the acquisition of a full k-space line, provided a pre-phasor lobe is pulsed to begin the acquisition at the edge of k-space. A phase encoding gradient is pulsed before an acquisition to traverse a single point in k-space and can be used alongside a frequency encoding gradient to change the initial position in k-space of a collected k-space line. Frequency encoding gradients are used to encode the largest k-space dimension, as multiple points are acquired each TR. Phase encoding gradients are used for the remaining two dimensions for full 3D encoding.

### 2.2.4 Image Reconstruction

The k-space domain is used for image reconstruction in MRI. To acquire signals to fill k-space, a range of gradient strengths must be used to acquire all unique combinations of $k_x$, $k_y$, and $k_z$. Performing RF transmit and receive while transmitting these gradients is known as a pulse sequence. Once k-space is filled, the inverse Fourier transform can be used to create an image from the k-space data.

## 2.3 RF Hardware at different field strengths

### 2.3.1 RF coil overview

An RF coil is made up of a few basic components. The first component is the inductive ($L$) wire windings, which produce a magnetic field when current flows through. According to Ampere's Law,

$$\oint B \cdot dl = \mu_0 I \,, \tag{2.10}$$

where $B$ is the magnetic field produced, $dl$ is a segment of a closed loop path the magnetic field travels, $\mu_0$ is the permeability of free space and $I$ is the current enclosed by the magnetic field. When an RF current flows in these windings, an oscillating magnetic field is produced at the frequency of the current, known as the $B_1$ field. The $B_1$ field has two counter rotating components: a $B_1^+$ field that rotates in the same direction as the spin precession, and a $B_1^-$ field that rotates opposite spin precession. The RF frequency is set to the Larmor Frequency, as discussed previously, to induce excitations with the $B_1^+$ subfield and receive a signal from protons with the $B_1^-$ subfield. The second component of an RF coil is tuning capacitance. To allow for unimpeded flow of RF current at a specific frequency, a resonant circuit must be constructed, requiring a capacitance and inductance:

$$f_0 = \frac{1}{\sqrt{LC}} \tag{2.11}$$

The tuning capacitance serves as the main component of this capacitance, and the inductance is provided by the wire windings, but can be supplemented with a series inductor. The third component is matching capacitance, which is used to match the impedance to the coil to the power amplifier or receiver it is connected to, which is typically 50 Ω. This is done for maximum

power transfer according to Jacobi's law, which states matching resistance and opposite reactance for a reactive circuit maximizes power transfer.

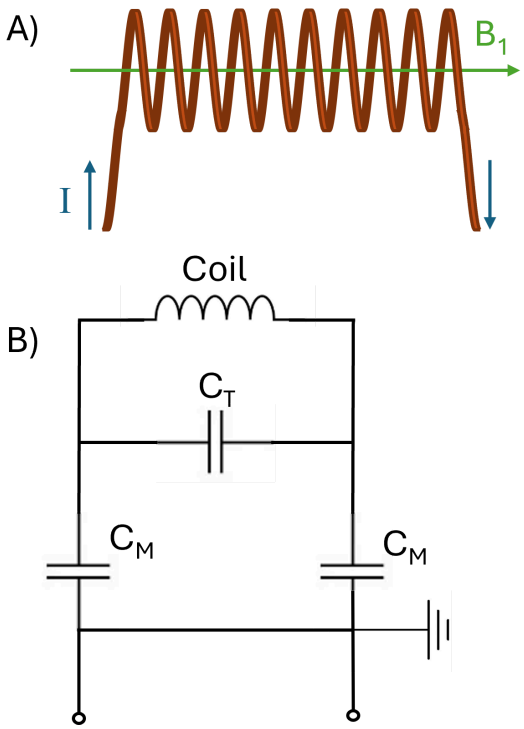


Figure 2.1: A) Diagram of a simple solenoid coil and B) a simple tune and match circuit, where $C_T$ is the tuning capacitance and $C_M$ are the matching capacitors.

The winding patterns for RF coils can take many forms. In this work, we used three patterns: a loop coil, a solenoid coil and a saddle coil (Figure 2.2). The loop coil is wound in a planar circular shape and can consist of single or multiple windings. The $B_1$ fields produced by these coils are inhomogeneous across space, so they are typically laid out in an array on a cylinder, such that the superpositions of all of the coils' $B_1$ fields can produce a homogeneous $B_1$ field over the imaging volume. A solenoid is composed of multiple windings around a cylindrical former, and therefore by the right hand rule, produces a magnetic field along the long

axis of the cylinder. This $B_1$ field is homogeneous toward the center of the windings if the windings are spaced evenly. If the gaps between each winding is varied, then a $B_1$ field following a linear or other target pattern can be achieved. A saddle coil consists of two planar square windings that are aligned, but separated by a gap. Each of these planar windings produces a magnetic field perpendicular to it, and these two fields sum between the two planar windings to produce a homogeneous $B_1$ field between them.

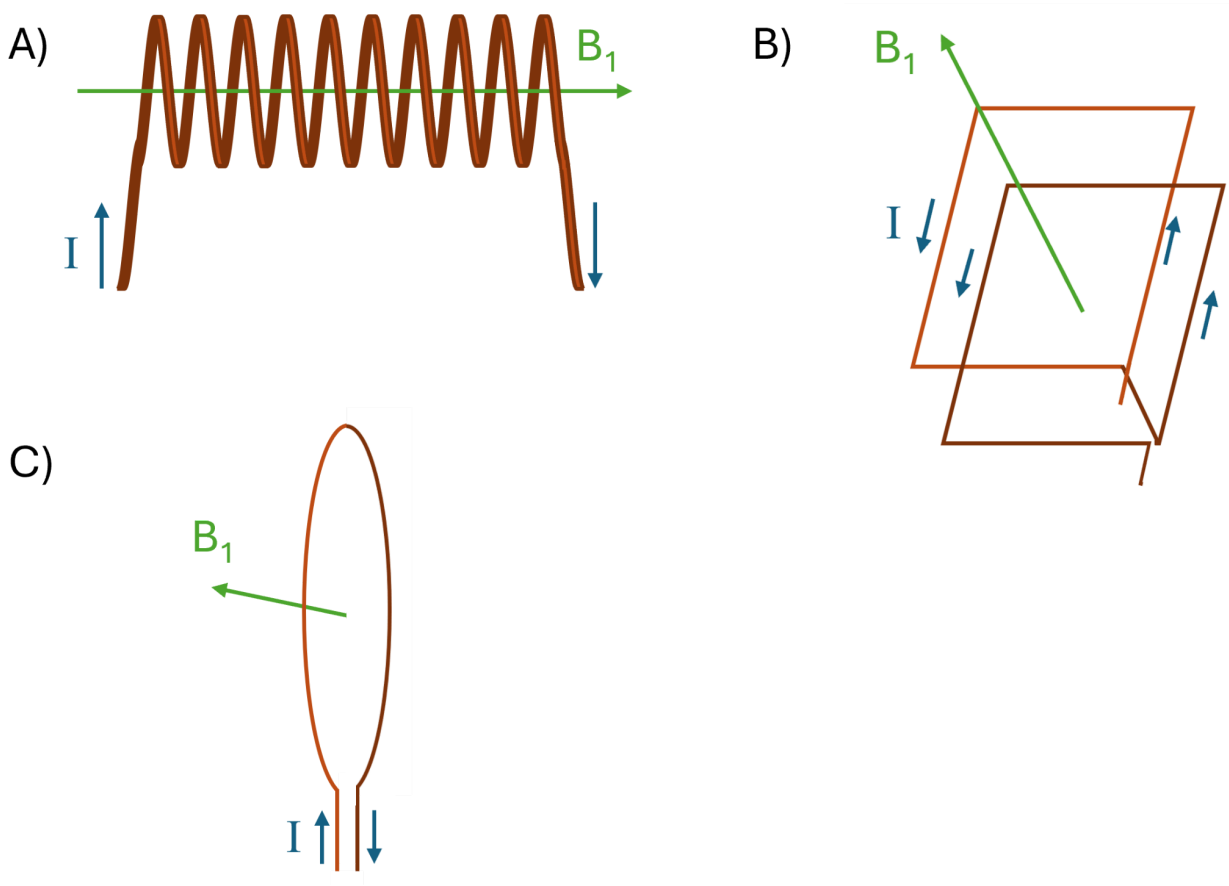


Figure 2.2: Diagrams of different coil winding patterns; A) solenoid, B) saddle, and C) loop coil, showing the main $B_1$ field direction for a given current flow $I$.

### 2.3.2 Parallel imaging

Parallel imaging uses an array of resonant coils, which could be for RF receivers that are placed around a sample like, for example, the array of loop coils described above. Each coil within this

array can receive data that can be used to reconstruct a fully-sampled image. Each of these coils ( $l = 1 \ldots L$) has a sensitivity map $c_l$ proportional to their $B_1^-$ field and is dependent on their placement around the sample. The fully-sampled image reconstructed using data from a single coil in the array, would be shaded based on the sensitivity map of the coil. The reconstructed image would have low signal regions within the sample, resulting in a low signal-to-noise ratio (SNR) in that region. Low SNR regions would likely result in a diagnostically inadequate image. The data measured on $L$ coils $m_s$ ($Lx1$ vector) is a combination of the coil sensitivity maps $c$ ($Lx1$ vector) and noise $n$ ($Lx1$ vector) for data $m$ ($1x1$ vector) for voxel $\vec{x}_p$.

$$m_s(\vec{x}_p) = c(\vec{x}_p)m(\vec{x}_p) + n \tag{2.12}$$

The signal from multiple coils can be combined using a minimum variance estimate to estimate the complex image data $\widehat{m}$ for voxel $\vec{x}_p$, which can then be combined to form an image with high signal, throughout the volume covered by the elements' sensitivities (2.13).

$$\widehat{m}(\vec{x}_p) = (c^H \psi^{-1} c)^{-1} c^H \psi^{-1} m_s(\vec{x}_p) \tag{2.13}$$

Parallel imaging techniques use additional encoding provided by coil sensitivity maps. The sensitivity maps act as multiplied weights to data in the image domain. Therefore, they act as a convolution in k-space, by the convolution property of the Fourier transform. This means for a single point in k-space, data for local k-space centered around that point are also collected based on the sensitivity map. The sensitivity maps are typically measured at high-field strengths for each patient as the magnetic fields are distorted by the frequency dependent effects of permittivity and conductivity of tissues. These effects are minimal at low-field, allowing for a single calibration measurement of the sensitivity maps.

The MRF-type sequence used for SENF produces signals that are unique across different spatial locations and relaxation rates, which populate a dictionary used for reconstructing spatially resolved quantitative maps. To incorporate the encoding provided by the coil sensitivity maps, the dictionary entries are weighted by the coil sensitivity maps for each coil ($l = 1 \ldots L$) in the array to produce $L$ signals for each entry, as if they were received on each coil in the array. These $L$ signals are then concatenated for each unique spatial location and relaxation rate entry within the dictionary to incorporate the additional encoding provided by the coil sensitivity maps into the dictionary.

### 2.3.3 Parallel Transmit (pTx) Array

Parallel transmit (pTx) arrays consist of multiple independent coil elements that are driven simultaneously to produce desired excitation patterns (Katscher, 2006; Webb, 2010). These coil elements have independent RF sources that are weighted differentially in amplitude and phase to modulate their individual contributing $B_1^+$ fields. These individual $B_1^+$ fields are superimposed when multiple coil elements are transmitting simultaneously, producing a target $B_1^+$ field, which is typically a homogeneous field over the imaging region of interest. A particular set of amplitude and phase weights for each coil is known as a coil mode.

Targeting a particular $B_1^+$ field across a region of interest is known as RF shimming. RF shimming is similar to $B_0$ shimming, where DC current is driven through shim coils to produce static $B_0$ shim fields that correct for signal loss causing $\Delta B_0$ inhomogeneities through $T_2^*$ and unwanted effects on RF pulses. $B_0$ shimming is typically performed with three orthogonal $B_0$ shim fields, generated with DC offset currents on the gradient coils and with second order shim

fields from additional coils (de Graaf, 2016). Higher order $B_0$ shim hardware has also been developed, using arrays of coils analogous to RF shimming (Stockmann, 2018).

RF shimming is not limited to targeting homogeneous $B_1^+$ fields. An arbitrary $B_1^+$ field can be targeted using a particular coil mode. The RF shim can be kept constant throughout a scan or varied dynamically by adjusting the coil mode during the scan, or even within a pulse to achieve complicated excitation patterns. SENF uses several different coil modes of a pTx array, in combination with pulses that create $B_1$ dependent effects, to produce unique excitation patterns over the imaging region of interest. The coil mode and pulses are pseudo-randomly varied at each TR within a sequence, such that magnetization for adjacent spins within the imaging region of interest quickly becomes incoherent. These excitation patterns create a modular imaging and spatial encoding system for SENF.

### 2.3.4 Low-field vs high-field coil considerations

Resonant RF coils are used for transmitting and receiving in MRI as described previously. Considerations differ when constructing these coils for low-field and high-field MRI. The resonant frequency of RF coils is set to the Larmour frequency (Eq. 1.2) of the protons within the $B_0$ field, for which the coil is designed. This frequency or the resonant circuit is determined by Equation 2.11. The inductance $L$ is determined by the geometry and number of windings of the coil, which is typically a loop coil or a solenoid. Additional inductance can be added with a series inductor; however, adding a significantly large inductor without a ferrite core that is not too bulky is not realistic. Therefore, a large capacitance must be used to produce a low enough frequency for a low-field scanner; specific examples are given below. Using a large capacitance causes decoupling issues when using multiple coils that are not completely orthogonal, causing

most coils to be used in transceiver mode. This configuration requires using an external transmit-receive (TR) switch to isolate the transmit power from the RF receiver.

A single 20 gauge wire loop with a diameter of 10 cm has an inductance of 0.307 $\mu$H. For a 47.5 mT scanner, the proton Larmor frequency is 2.02 MHz, requiring a large (for RF) capacitance of 20.221 nF. For a 3 T scanner, the Larmor frequency would be 127.74 MHz, requiring a capacitance of 5 pF. For example, if the coil now has 5 turns of wire, the inductance becomes 7.69 $\mu$H. This would require a capacitance of 0.803 nF for the 47.5 mT scanner and 0.20186 pF for the 3 T scanner. Non-magnetic capacitors are available in the pF range, so single turn coils require a large amount of parallel capacitors to achieve the desired resonant frequency at low-field. The capacitance for a multi turn coil at high-field is extremely low, at only a fraction of a pF. The parasitic capacitance of the coil becomes higher than this value, causing self-resonance within the coil at an undesired frequency. Multi-turn coils at low-field still require much larger capacitances and self-resonance is not typically a concern.

A tuning and matching circuit is used with the coil to achieve the desired resonant frequency and power transmission (Figure 2.1). A parallel capacitor is used mainly to tune the resonance frequency to the desired value, while a series capacitor is used to match the impedance of the coil to the impedance of the transmit amplifier and RF receiver (typically 50 Ω) for maximum power transmission. A series spoil resistor can also be used to increase the bandwidth of the coil at the cost of SNR and power efficiency, which can be a necessary trade off using wideband transmit pulses or with an inhomogeneous $B_0$ field. Lower field strengths also result in much longer wavelengths of the RF currents used to generate $B_1^+$ and receive proton signals. At high-field strengths, the much shorter wavelengths require that coils and their circuits be carefully constructed. This construction must account for, among other things, trace lengths and

widths. Such considerations are not relevant for low-field coils due to the longer wavelengths. The shorter wavelengths also cause inhomogeneities in the $B_1$ field across the imaging volume, since the wavelengths are shorter than the width of the imaging volume. The wavelengths are many times longer than the imaging volume at low-field, allowing for Biot-Savart calculations (Eq. 2.10) to be used to simulate $B_1$ fields with high accuracy.

## 2.4 Quantitative MRI

### 2.4.1 Conventional Quantitative MRI (qMRI)

Quantitative MRI (qMRI) allows for the mapping of parameters such as $T_1$ and $T_2$ relaxation times. These quantitative parameters can be used as biomarkers to detect and monitor diseases such as cancer or ischemic stroke. The main component of qMRI is the pulse sequence, which is designed to sensitize the NMR signal to a particular parameter allowing for the calculation of a parametric map from the signal rather than a typical contrast image.

For $T_1$ mapping, an inversion recovery (IR) sequence is most commonly used. An inversion pulse is used to invert the magnetization of the proton that will return to equilibrium at a rate determined by the $T_1$ relaxation time of the tissue the proton is in. The time between the inversion pulse and an excitation pulse (the inversion time) is varied over multiple acquisitions. Following each inversion time, the signal is acquired. Full gradient encoding is performed for each inversion time to produce a full image. The voxel amplitudes across images (inversion times) are then fit to a (usually) monoexponential Eq. 2.14 to calculate a $T_1$ map,

$$S = S_0(1 - 2e^{-TI/T_1}), \tag{2.14}$$

where $S$ is the signal in a voxel, $S_0$ is an initial signal level of the voxel and $TI$ is the inversion time. Practically, $S_0$ and $T_1$ are fit simultaneously with measured images $S$ and corresponding

inversion times $TI$. Biexponential models have also been implemented (Rioux et al., 2016), which assume a slow and fast $T_1$ caused by free water and macromolecule hydrogens in tissues.

For $T_2$ mapping, a multi spin-echo sequence is most commonly used. A 90° excitation pulse is used to flip the magnetization into the transverse plane and is followed by a train of refocusing pulses with flip angles of 180° and separated by an echo time ($TE$). Full gradient encoding is performed so that an image is obtained for each $TE$. The voxel amplitudes across images (echo times) are then fit to a monoexponential Eq. 2.15 to calculate a single $T_2$ map image,

$$S = S_0 e^{-TE/T_2}, \tag{2.15}$$

where $S$ is the signal in a voxel, $S_0$ is an initial signal level of the voxel and $TE$ is the echo time. Practically, $S_0$ and $T_2$ are fit simultaneously with measured images $S$ and corresponding echo times $TE$. Biexponential models have also been implemented (Sharafi et al., 2018), which assume a slow and fast $T_2$ caused by free water and macromolecule hydrogens in tissue. Multiexponential models have also been proposed for slow, intermediate and fast $T_2$ components (Does, 1995; Does, 1996). Biexponential and multiexponential models of relaxation parameters provide intravoxel information related to physiological factors. MRI can also be used to quantify many other physiological parameters including: diffusion, magnetic susceptibility, tissue elasticity, metabolite concentrations, fat fraction, and blood flow (Keenan et al., 2017). In this thesis, SENF is proposed for encoding spatial information and $T_1$ and $T_2$ relaxation parameters, specifically a single $T_1$ and $T_2$ per voxel.

### 2.4.2 MRF

Magnetic resonance fingerprinting (MRF) is an imaging technique that uses the variation of sequence parameters, such as the flip angle and phase of excitation pulses, TR and TE in a inversion recovery balanced steady state free precession (IR-bSSFP)-like sequence (Figure 2.3A) to produce unique signal evolutions for different combinations of MR parameters such as $T_1$, $T_2$ and $\Delta B_0$. Fast Imaging with Steady State Precession (FISP) sequences are used in MRF currently as they are more robust (Jiang et al., 2014). These unique signal evolutions are called 'fingerprints' of a specific combination of MR parameters (Ma et al., 2013). Using a priori knowledge of system parameters and prescribed set of MR parameters, a dictionary of fingerprints are simulated using the Bloch equations. A pattern matching algorithm is used to

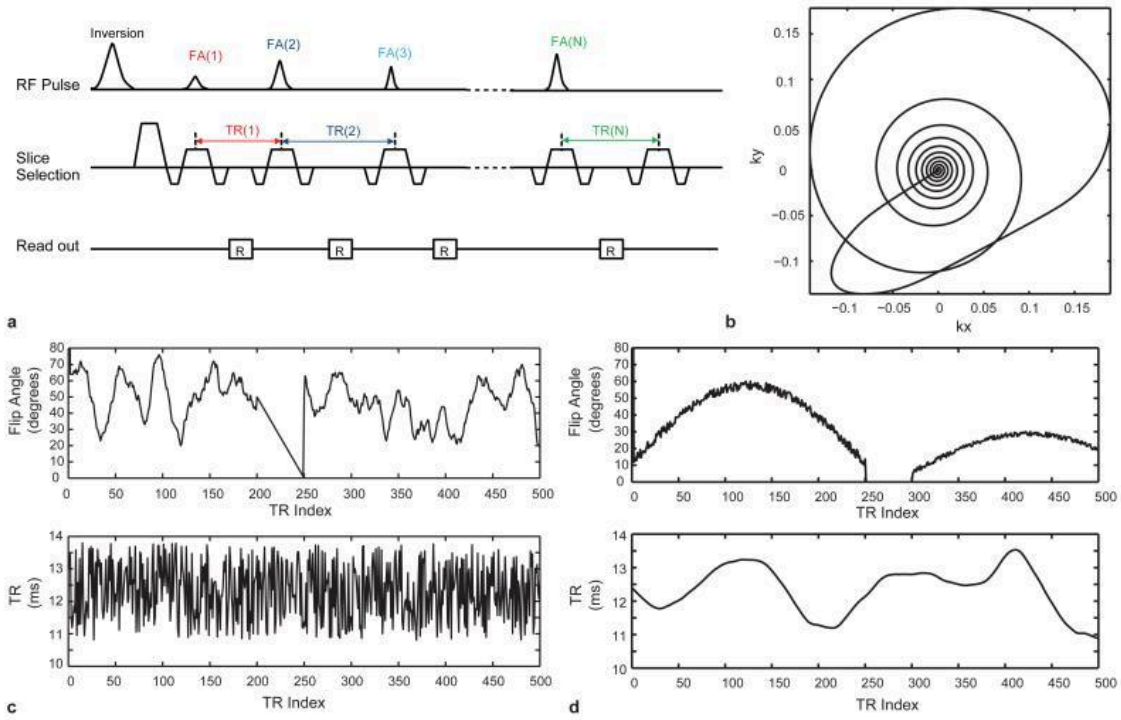


Figure 2.3: From Ma et al., A) a modified inversion recovery balanced steady state free precession (IR-bSSFP) sequence using B) one of the variable density spiral readouts, which was rotated at each TR. C) and D) are examples of the variation of the flip angle and TR length used for the first 500 samples.

reconstruct parameter maps from measured signals, i.e. by identifying which 'fingerprint' (Figure 2.4) best resembles the signal at each voxel. In this way, MR fingerprinting is capable of producing quantitative maps of more than one MR parameter from a single acquisition.

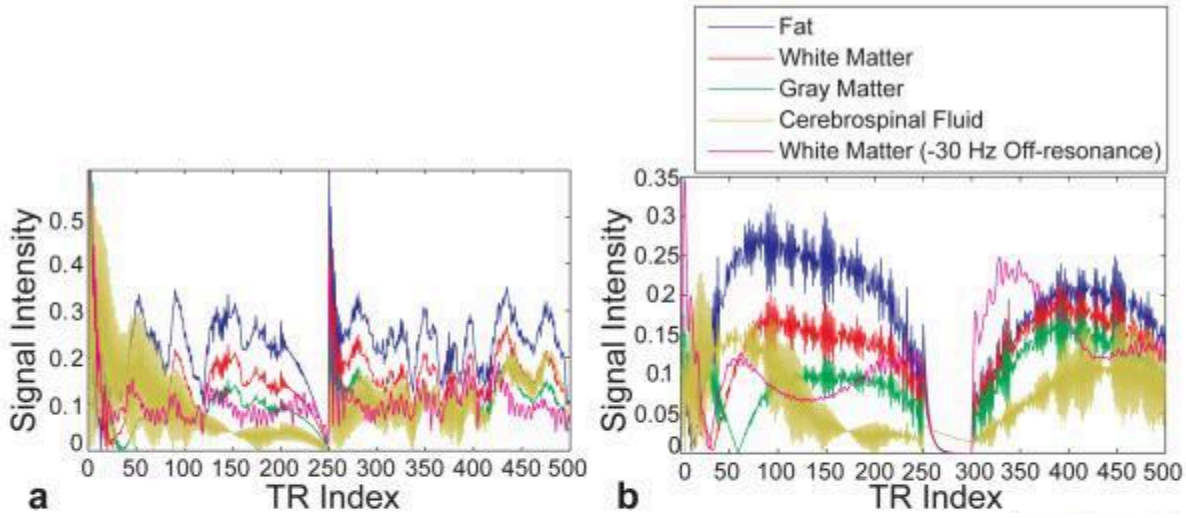


Figure 2.4: Modified from Ma et al., A) five different fingerprints of brain tissues produced by parameter variations shown in Figure 2.3C B) and Figure 2.3D.

It is important to note, that MRF sequences continuously vary sequence parameters to prevent a steady state from being reached, allowing for unique information to be encoded into the signal evolutions as the sequence progresses. Conventional quantitative MRI techniques require multiple images to fit an MR parameter as discussed previously, while MRF can reconstruct multiple parameters simultaneously, making MRF a more time efficient technique. Scan time is further reduced in MRF by using undersampled k-space trajectories, such as spirals (2D) and stack-of-spirals (3D). This is possible due to the insensitivity of the pattern matching algorithm to undersampling errors in the data, so long as those errors manifest approximately as stationary zero-mean noise. Tissue fingerprints consist of multiple MR parameters, which could be used together to assist in the detection of different diseased tissues such as cancer.

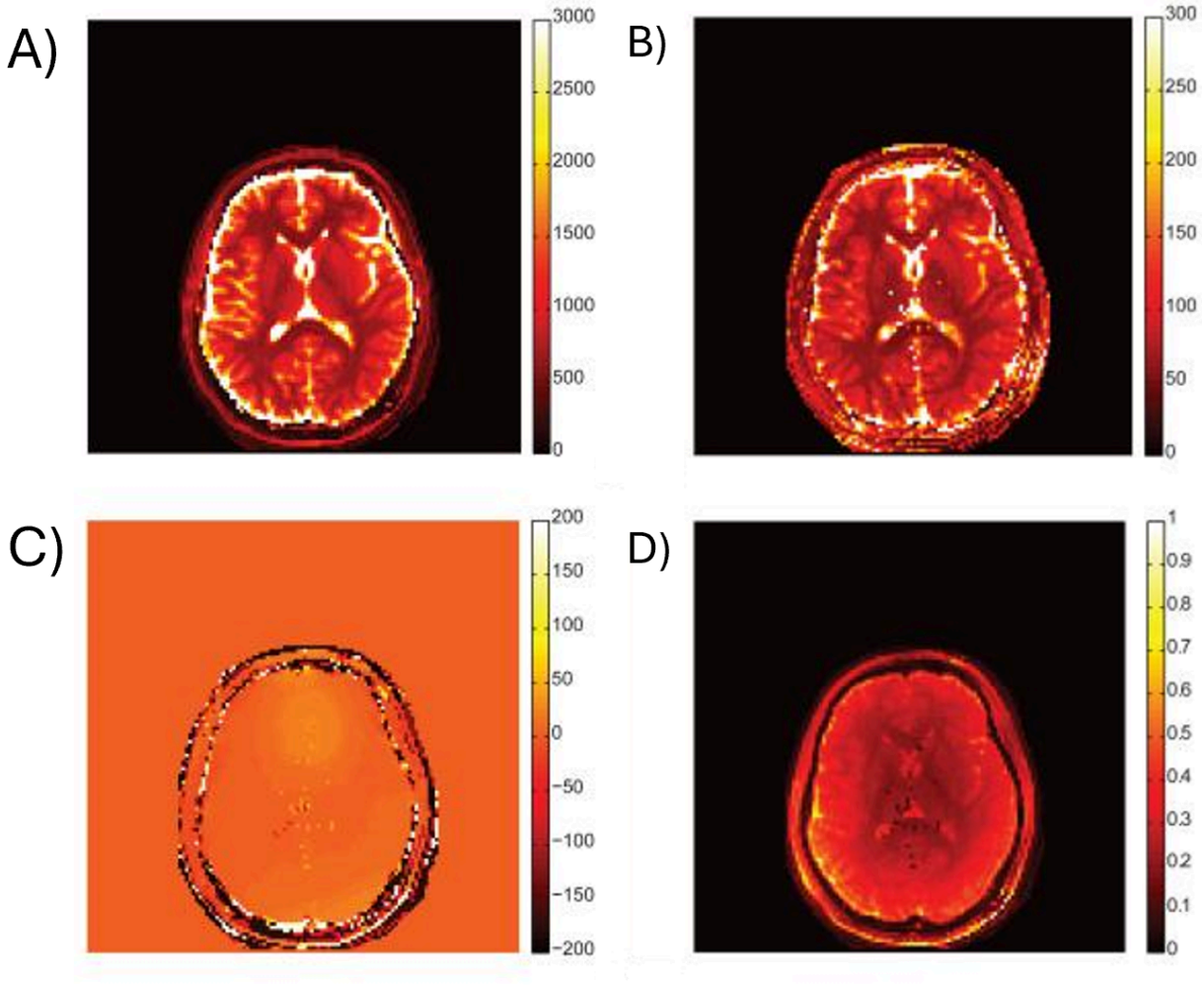


Figure 2.5: Modified from Ma et al. Reconstructed parameter maps using MRF: A) a $T_1$ map, B) a $T_2$ map, C) an off-resonance ($\Delta B_0$) map and D) a proton density map.

Conventional quantitative imaging has poor reproducibility of MR parameters between different scanners due to variations in sequence parameters used, such as TI or TE choice, and hardware differences such as the transmit and receive coils used. MRF, however, has robust reproducibility and precision between different scanners ($\sigma$=2.21 for $T_1$ (%), $\sigma$=3.89 for $T_2$ (%)) and acquisitions ($\sigma$=1.90 for $T_1$ (%), $\sigma$=3.2 for $T_2$ (%)), outpreforming MPRAGE ($\sigma$=6.04 for $T_{1W}$ (%)) and turbo spin echo sequences ($\sigma$=5.66 for $T_{2W}$ (%)) (Körzdörfer et al., 2019; Dupuis et

al., 2024). MRF has seen clinical use in cancer detection and treatment monitoring for brain tumors (Badve et al., 2015; Badve et al., 2017), breast cancer (Panda et al., 2017) and prostate cancer (Panda et al., 2019). MRF has also been used for ejection fraction quantification in cardiac imaging (Hamilton et al., 2020; Jaubert et al., 2020).

### 2.5 RF Encoding

Radiofrequency (RF) encoding is a technique where traditional $B_0$ gradient encoding is replaced by $B_1$ amplitude or phase gradients. This can potentially reduce the power requirements and cost of an MRI system and is ideally suited for low-field due to reduced SAR constraints as discussed in Chapter 1.

#### 2.5.1 $B_1$ Amplitude Methods

The Rotating Frame Imaging (RFI) RF gradient encoding method proposed by David Hoult requires a $B_{1y}$ pulse played through an RF amplitude gradient coil with a spatial $B_1$ gradient along y to produce spatially dependent flip angle along y. The magnetization $M_0$ in this case nutates in the xz-plane. A 90° $B_{1x}$ pulse is played in the x direction to flip the magnetization into the xy-plane, where the magnetization is allowed to evolve, resulting in a spatially dependent phase to be encoded into the FID. This method is simple to implement, but in practice, the need to produce a phase gradient in a longitudinal plane would lead to complicated signal contrast and is only capable of phase encoding, making multi-dimensional imaging very slow. RFI would also be sensitive to confounding dephasing caused by off-resonance during signal evolution after spins are excited into the transverse plane. For the practical experiment, a $B_1$ gradient in the x-direction was created using a saddle coil with lopsided windings with a nested solenoid receive

coil. No 90° pulse was used to flip the magnetization into the xy-plane; instead, a $B_0$ gradient along the z-direction was pulsed. Several acquisitions are performed for different pulse lengths of the $B_{1x}$ gradient and the Fourier transform of the first acquisition is taken and phase corrected. The remaining acquisitions are transformed with the same phase correction to build a matrix of absorption spectra with rows corresponding to $B_{1x}$ pulse lengths and columns corresponding to z position. The sine Fourier transform of each column is then taken to produce an image.

Single Echo Acquisition (SEA), proposed by Steven M Wright and Mary Preston McDougall in 2009, uses the receive coil sensitivities of a custom 64-element 1D parallel transmit array to fully encode a single dimension, allowing for a full image to be constructed with a single k-space line acquisition using a conventional $B_0$ gradient. This 64-element array uses narrow coils, each with receive sensitivities over a long narrow stripe across the imaging volume. A 1D Fourier transform is performed on the echo, received by each of the 64 coils and each of these are stacked to form a 2D image.

In reference (Katscher et al., 2010), Katscher et al. proposed using spatially non-linear RF fields as spatial encoding functions for full 2D RF spatial encoding. These spatial encoding functions were produced by the superposition of coil sensitivities of RF coils in an 8-channel parallel transmit array.

### 2.5.2 Phase-Based Methods

Transmit Array Spatial Encoding (TRASE), introduced by Jonathon Sharp and Scott King in 2010, uses two RF phase gradient coils with opposing linear phase gradients. To traverse k-space with TRASE, refocusing pulses in a multi-spin echo sequence are transmitted alternatively

between the two coils, allowing for spins to accumulate phase each time a refocusing pulse is applied.

The Bloch-Siegert (BS) shift is a phenomenon in which an off-resonance RF pulse causes protons to precess at a shifted frequency. The shift in precession is proportional to the $B_1$ field amplitude squared. Therefore, if a square root $B_1$ gradient coil is used to vary the field strength across space, the protons would have a linearly varying precession frequency across space, analogous to traditional $B_0$ gradients. Hence, the BS shift is a potential phase-based RF encoding method when paired with RF gradient coils ( Hasselwander, 2017; Srinivas et al., 2022). BS shift has been principally investigated as a means of phase encoding (Srinivas et al., 2022), and more recently, frequency encoding using the BS shift has been achieved (Srinivas et al., 2023; Srinivas, 2023). This particular setup used a custom gradient solenoid, optimized to produce a square root $B_1^+$ field to produce a linear phase gradient along with a nested saddle receive coil.

In reference (Torres et al., 2022), Torres et. al. developed the RF encoding method: frequency-modulated Rabi-encoded echos (FREE). FREE uses adiabatic full passage pulses and an RF gradient field to produce spatially dependent phase analogous to a conventional $B_0$ phase gradient. The RF gradient field was produced by a single elliptical loop coil, which was also used as a receive coil for experimental implementation.

Each of these RF gradient methods used different and custom RF coils to produce RF amplitude and phase gradients with different spatial structures. Each was developed specifically for its method to take advantage of the principles of that method that allow for spatial encoding within that particular field structure.

## 2.6 Summary

In this chapter, first, an overview of MRI physics was discussed, reviewing the components required for conventional MRI including: a main $B_0$ field, RF transmit and receive, $B_0$ encoding gradients and image reconstruction. Cartesian sampling gradient-recalled echo (GRE) sequences, which operate on these principles, are used to measure $B_1^+$-selective pulse excitation profiles, create control images for $B_1^+$-selective encoding experiments and measure susceptibility parameters for more accurate dictionary simulations, which are discussed in Chapter 5. The Bloch-equation (Eq. 2.4) is used for dictionary simulations for a 2D SENF feasibility simulation discussed in Chapter 3 and for SENF experiments performed on a 47.5 mT scanner discussed in Chapter 5. Next, RF hardware is discussed, providing an overview of RF coils and considerations between high-field and low-field RF hardware designed, which is relevant to the coils constructed, discussed in Chapter 4, for the experimental implementation of SENF on a 47.5 mT scanner. Parallel imaging and parallel transmit arrays (pTx) were discussed as these principles were used in the 2D SENF feasibility simulation discussed in Chapter 3. Next, conventional quantitative MRI and MRF were discussed to show existing quantitative encoding techniques. In particular, MRF shares many principles with SENF necessary to understanding the SENF encoding process, mainly sequence parameter variation of simultaneous encoding of multiple quantitative parameters and the simultaneous reconstruction of multiple parametric maps. Finally, existing RF encoding methods are discussed to provide context for the RF encoding used with SENF for spatial encoding. In the following chapter, the full SENF encoding process will be discussed, along with a feasibility simulation and the introduction and comparison of multiple SENF sequences.

# CHAPTER 3: SELECTIVE ENCODING THROUGH NUTATION AND FINGERPRINTING (SENF)

## 3.1 Introduction

Conventional MRI uses $B_0$ gradients to perform spatial encoding. These $B_0$ gradients are produced by gradient coils. The construction of these coils increases the building costs of an MRI scanner, as well as the operation costs of the scanner through increased power consumption and cooling systems. Additionally, they take up space within the scanner bore that could otherwise be used for additional RF coils or to provide more flexibility in magnet design, space to perform image-guided interventions or to improve patient comfort. During scans, $B_0$ gradients produce auditory noise due to Lorentz forces and can induce peripheral nerve stimulations, reducing patient comfort. Other spatial encoding techniques have been proposed, including parallel imaging, which uses coil sensitivity maps for additional encoding power. RF gradient techniques have also been proposed, which remove the need for $B_0$ gradients, but to date, are slow for multidimensional encoding and have complicated contrasts that are difficult to interpret (Hoult, 1979; Wright, 2009; Sharp, 2010; Katscher et al., 2010; Torres et al., 2022).

Quantitative MRI (qMRI) is useful for producing parametric maps that are quantitatively interpretable, rather than subjective interpretations of contrast images that must be performed by trained radiologists. MRF has the capability to produce multiple parametric maps simultaneously, leading to more time efficient acquisitions than conventional qMRI, which requires acquisition of multiple images to fit quantitative models. However, MRF still uses $B_0$ gradients for spatial encoding.

In this chapter a new method of encoding MRI data is proposed: Selective Encoding through Nutation and Fingerprinting (SENF). SENF is a $B_0$ gradient-free quantitative RF

encoding technique that simultaneously encodes spatial and quantitative information, removing the need for $B_0$ gradients and producing quantitatively interpretable results in a time-efficient manner. SENF uses inhomogeneous $B_1$ fields and pulses that create $B_1$-dependent effects to produce multiple encoding patterns, which are used in an MRF-type sequence to create incoherent signals between different spatial locations and tissues. To reconstruct the data, a signal dictionary was simulated across spatial locations and tissue parameters. A regularized pseudoinverse of the dictionary was taken and applied to the measured data to produce coefficients for all spatial locations and tissue parameters. The largest coefficients are chosen across all spatial locations to assign tissues to each and using prior knowledge of tissue parameters, multiple parametric maps are simultaneously reconstructed.

In this chapter, the SENF encoding process and its components are discussed. Following this, a proof of concept feasibility simulation is presented, wherein a 2D brain slice phantom was encoded and reconstructed using a simulated idealized SENF implementation. Finally, three different SENF sequences are introduced: $B_1^+$-selective SENF, hard pulse SENF and qRF-BS SENF. These sequences were compared in simulation between each other and conventional $T_1$ IR and $T_2$ spin echo sequences, in terms of spatial resolution and minimum SNR.

## 3.2 Methods

### 3.2.1 SENF Encoding Process

SENF is achieved with four components: a variable $B_1$ field, pulses that create $B_1$-dependent effects within this field, a Magnetic Resonance Fingerprinting (MRF) type sequence and a combined MRF and image reconstruction. In the following section, we discuss each of these components.

#### 3.2.1.1 Variable $B_1$ Field

A spatially varying $B_1$ field can be achieved with many configurations or winding patterns of RF coils. This can be achieved with existing RF coils like pTx arrays that are already used for RF transmit in conventional MRI. It can also be achieved with simple winding patterns, such as a gradient solenoid with a linearly increased gaps between windings or a single loop coil. An inhomogeneous $B_1$ field is desired, so that pulses with $B_1$-dependent effects can be used to produce spatially varying effects on the spins to allow for spatial localization. A parallel transmit array is preferred, as it provides the ability to produce a large variety of inhomogeneous $B_1$ fields by using different coil modes. These coil modes are produced by adjusting the relative phases and amplitudes of the pulses that are input to each coil element in an array as they are transmitted through simultaneously (Figure 3.2). Because the $B_1$ fields of the different coil elements will combine with different amplitudes and phases in different modes, the total $B_1$ fields of different modes will have low correlation to each other, which creates the opportunity to leverage the different modes for spatial encoding.

#### 3.2.1.2 $B_1$-dependent Pulse Effects

The spatial inhomogeneity of $B_1$ fields is taken advantage of using pulses that create $B_1$ -dependent, and therefore spatially dependent effects to differentiate signals across space for spatial encoding. More specifically, the $B_1$-dependent effects produce spatially varying magnitude or phase changes to the spins present within the $B_1$ field. Different pulses are used to produce different spatial patterns of magnitude or phase changes that vary significantly from one another. Spatial resolution and minimum SNR quantify the achievable spatial and quantitative

encoding power of the encoding patterns used within a SENF sequence. This causes the signal for a particular spatial location to vary significantly from all others when these excitation patterns are played sequentially. This results in each spatial location having a unique signal, much like how MRF differentiates quantitative parameters for a single voxel.

#### 3.2.1.2.1 Hard Pulses

$B_1$ dependent amplitude effects can be achieved with a simple hard pulse, which has a $B_1$ -dependent flip angle (Eq. 2.3). Therefore, in a spatially varying $B_1$ field there will be spatially dependent flip angles applied to the spins. Spins that are flipped near multiples of 90° will be strongly excited, while spins that are flipped near multiples of 180° will be nulled (Figure 3.1). This causes a signal banding pattern across a $B_1$ gradient that allows the differentiation of adjacent spins and is the basis of RF spatial encoding with hard pulses.

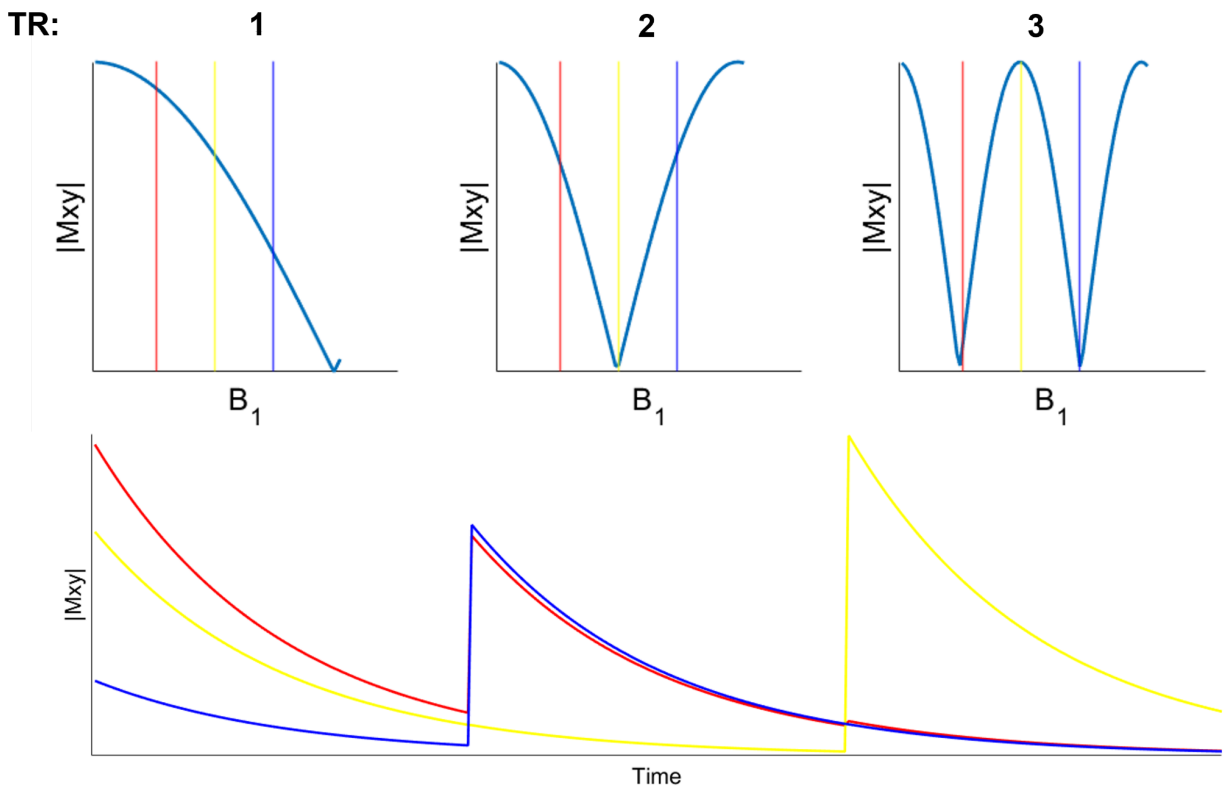


Figure 3.1: The first row shows the resulting $|M_{xy}|$ for spins excited from rest by a $B_1$ field gradient, produced from a hard pulse transmitted through a linear solenoid. Flip angles that are multiples of 90° produce a high signal. Flip angles that are multiples of 180° produce a null signal. The columns 1, 2 and 3 indicate the TR number in a sequence. Three positions are highlighted in red, yellow, and blue. The signs for each position are shown in the second row, as each $B_1$ gradient field strength is used for 3 TRs. Three unique signals are produced for three different spatial locations.

With hard pulse excitations, the widths of the lobes in the banding pattern are proportional to the local gradient of the $B_1$ field. The $B_1$ field would be linear for a simple linear gradient solenoid, resulting in spatially uniform lobe widths and consequently uniform encoding resolution. The different modes of a pTx array will produce $B_1$ fields with more complex multidimensional spatial structures that will have spatially varying feature widths, resulting in spatially non-uniform encoding resolution. An example of these excitation patterns is shown in Figure 3.2, where a 32-subband Hadamard $B_1^+$-selective pulse was transmitted through 64

different modes of an 8-coil pTx array to illustrate the complexity of the excitation patterns that can be achieved. This particular pulse was designed to have uniform $B_1$ band widths within a linear $B_1$ field analogous to a hard pulse with a peak flip angle at the highest $B_1$ field strength being several multiples of 90°. Here, the banding patterns oscillate faster with higher local $B_1$ field gradients close to the coils around the edge of the FOV, while the banding patterns towards the center of the FOV oscillate much slower due to the lower local $B_1$ field gradient. As these banding patterns are the basis for spatial encoding, the spatial resolution of this encoding is dependent on the widths of these bands within the banding patterns. Therefore the achieved spatial resolution is proportional to the local $B_1$ field gradient and varies across space. Each of these excitation patterns will be implemented in a TR within a SENF sequence, and the acquired signal from that TR is the integral of the transverse magnetization over the imaging volume.

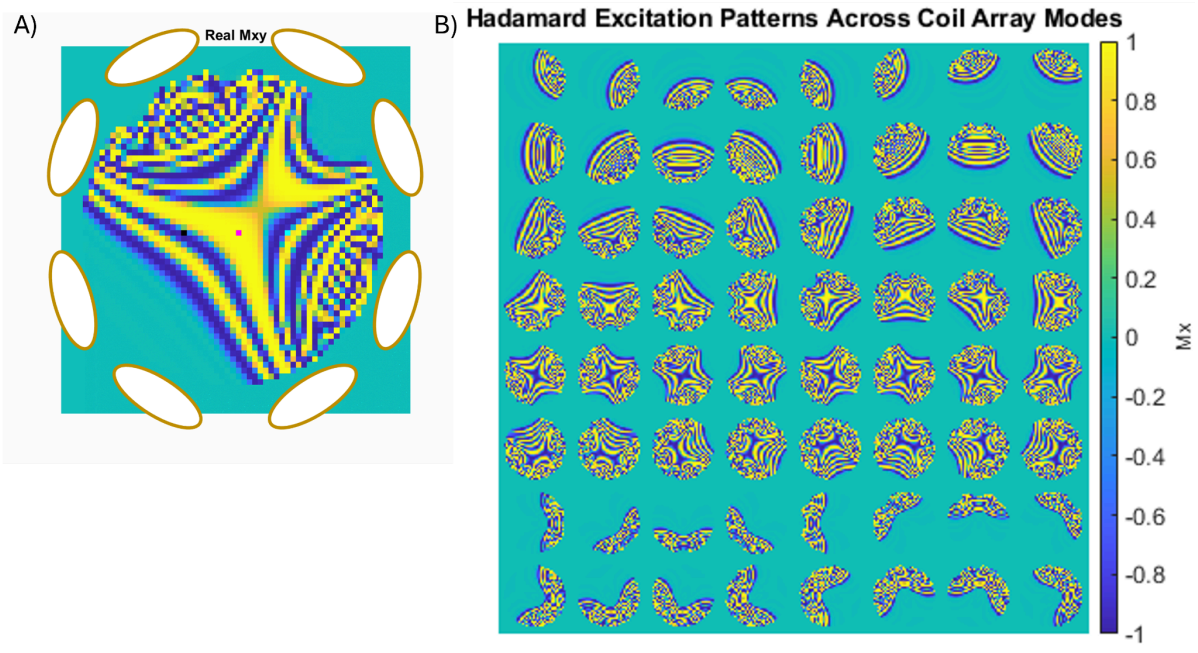


Figure 3.2: A) Excitation pattern of a 32 sub-band $B_1^+$-Selective Hadamard pulse transmitted through a particular mode of an 8 coil parallel transmit array. B) Excitation patterns of a 32-subband Hadamard $B_1^+$-selective pulse transmitted through 64 modes of an 8 coil pTx array with the same coil placement. The color scale indicates the magnitude and sign of the $M_x$ excitation of spins from rest produced by transmitting the pulse through the different modes.

#### 3.2.1.2.2 $B_1^+$-selective pulses

$B_1^+$-selective pulses (Grissom et al., 2014) can be designed using the Shinnar-Le Roux algorithm to produce slice-selective excitations with uniform flip angles over desired $B_1$ ranges. The flip angle of the excitation can be controlled by scaling the frequency waveform of the pulse without changing the excitation band position or width. This allows for independent control over tissue parameter encoding and spatial encoding. These pulses allow for selective excitation within the inhomogeneous $B_1$ produced by modes of a pTx array. For higher SNR efficiency, to excite the full range of $B_1$, while also differentiating adjacent spins, Hadamard $B_1^+$-selective pulses can be used (Figure 3.3).

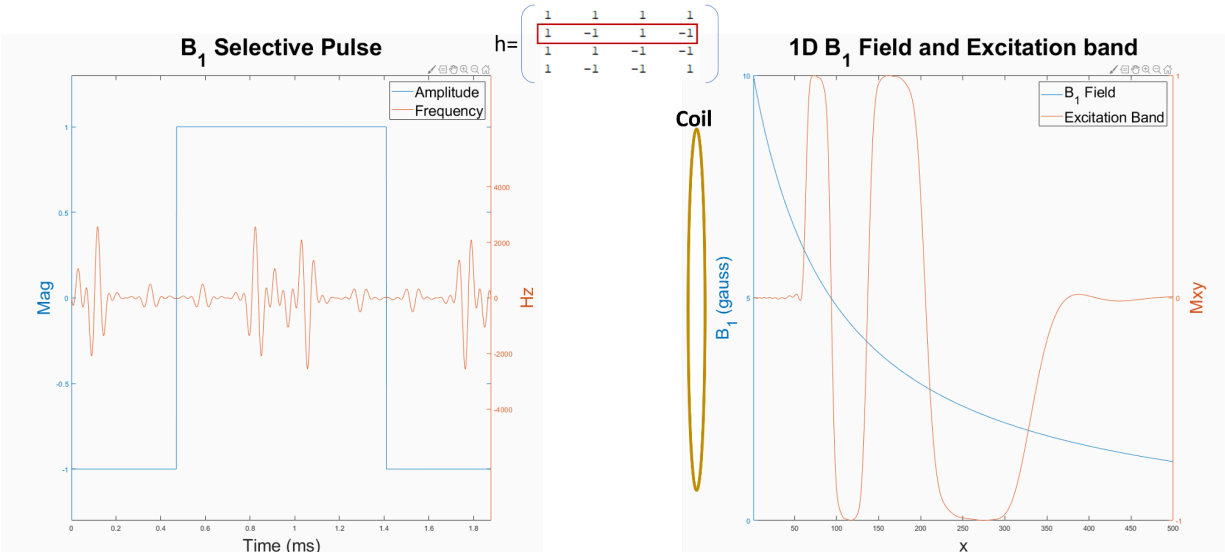


Figure 3.3: A 4-subband 2 ms-long $B_1^+$-Selective Hadamard pulse (left) which has a constant amplitude and is frequency modulated. The excitation pattern produced by the pulse was simulated in a 1/x $B_1$ field like that produced by a loop coil (right).

These pulses allow for uniform excitation over the full range of $B_1$, but produce positive and negative excitation within subbands following a Hadamard matrix. Using all pulses with excitation patterns corresponding to the entries in each row of the Hadamard matrix, the space

can be fully encoded. The Hadamard $B_1^+$-selective pulses can be designed so that the subbands have constant width across a non-linear $B_1$ field, to achieve more uniform resolution across the entire FOV (Figure 3.4).

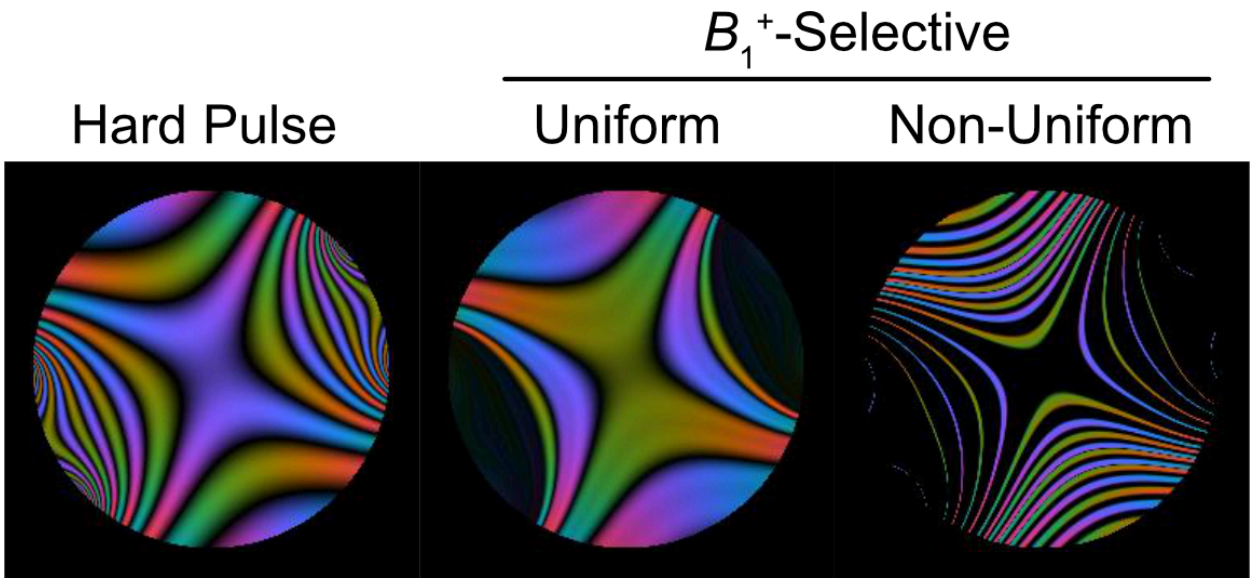


Figure 3.4: A single coil mode used to transmit a hard pulse, a uniform Hadamard $B_1^+$-selective pulse and a non-uniform Hadamard $B_1^+$-selective pulse. The hard pulse and uniform Hadamard $B_1^+$-selective pulse create banding patterns with varying widths across the FOV, while the non-uniform Hadamard $B_1^+$-selective pulse produces bands of approximately constant width across the FOV. This allows for uniform resolution over non-linear $B_1$ fields.

#### 3.2.1.2.2.1 Hadamard Pulse Design

To design these $B_1^+$-selective pulses, a modified version of the Shinnar-Le Roux (SLR) algorithm (Grissom et al., 2014) was developed. The SLR algorithm conventionally designs a transverse RF waveform and a constant gradient waveform that can be transmitted simultaneously to perform slice selection. The problem is cast in the rotating frame conventionally used to analyze adiabatic pulses and it is further rotated, so that the transverse RF waveform becomes a frequency modulation waveform $\Delta\omega_{RF}(t)$ and the gradient waveform is replaced by a pre-defined

amplitude waveform $A(t)$ of the RF pulse. These two RF pulse components combine to form an overall RF pulse as:

$$\vec{B}_1(t) = |B_1^+|\, A(t)(\hat{x}cos(\phi(t) + \angle B_1^+) + \hat{y}sin(\phi(t) + \angle B_1^+)) \quad (3.1)$$

$$\phi(t) = \int_0^t \Delta\omega_{RF}(t')dt' \quad (3.2)$$

This reframing is possible by rotating the pulse spinor parameter $\alpha$ to represent rotations about the x-axis instead of the z-axis, and rotating the pulse spinor parameter □ to represent rotations about a field with z and/or y components rather than the x and y components of a transverse field. The desired magnetization profile is then related to the spinor parameters whose inverted DFT coefficients represent the RF pulse needed to produce them.

$$M_x^+ = -\,2(\alpha_R\beta_R - \alpha_I\beta_I) \quad (3.3)$$

$$M_y^+ = -\,2(\alpha_R\alpha_I - \beta_R\beta_I) \quad (3.4)$$

The subscripts R and I represent real and imaginary components of the spinor parameters. The pulses are designed to produce constant phase, such that $M_y^+ = 0$ and $A(t)$ waveforms with zero integrated area so that $\alpha$ is only real valued, such that $M_x^+ = -\,2\beta_R$. Therefore $\beta_R$ can be designed as a filter to produce a desired $M_x^+$ profile. The β filters cannot be centered around $B_1$=0 Gauss because there is no excitation with zero RF field, and the β filter cannot be frequency modulated to shift the slice profile as this results in a complex $\Delta\omega_{RF}(t)$. The $\beta_R$ is designed as an odd dual-band filter, such that its DFT coefficients are purely imaginary and therefore produce a real-valued odd $\Delta\omega_{RF}(t)$. The β filter is then divided by the dwell time and scaled to the desired flip angle for the excitation band.

To design Hadamard pulses, a β filter is designed for a $M_x$ profile with multiple subbands with either a + or - sign, following the entries of a Hadamard matrix. To fully encode the $B_1$ range of the $M_x$ profile, each row of the Hadamard matrix is used to define the $M_x$ subbands within the $B_1$ range, producing a set of pulses equal to the size of the Hadamard matrix. For example, designing an 8-subbands $B_1^+$-selective pulse would require eight different pulses to be designed for full encoding. An example of the β filter for a single band and Hadamard $B_1^+$-selective pulse is shown in Figure 3.5.

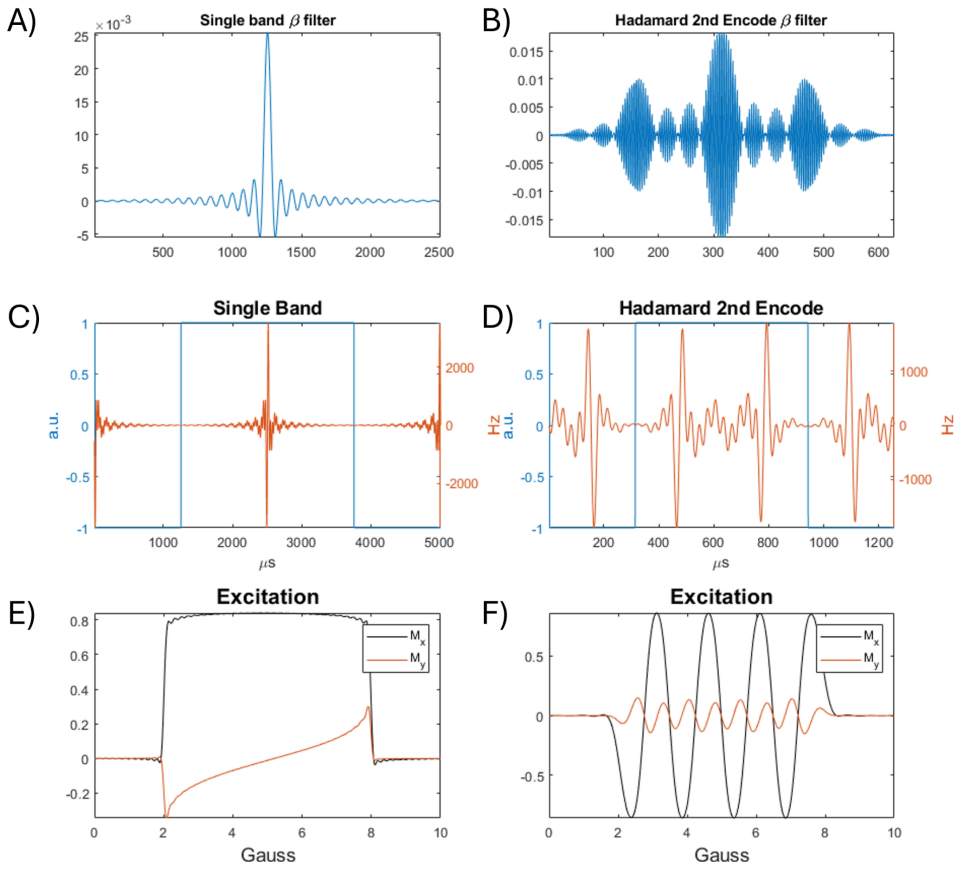


Figure 3.5: Single band excitation pulse 5 ms-long, with a passband center of 5 Gauss and a passband width of 6 Gauss. A) β filter for the single band pulse, C) amplitude and frequency waveforms for the single band pulse, and E) $M_x$ excitation profile of the single band pulse. Second encoded 8-subband Hadamard excitation pulse 1.25 ms-long, with a passband center of 5 Gauss and a passband width of 6 Gauss. B) β filter for the 8-subband pulse, C) amplitude and frequency waveforms for the 8-subband pulse, and E) $M_x$ excitation profile of the 8-subband pulse.

If a map of the inhomogeneous $B_1$ field to be used is known or can be approximated, the individual subbands of the pulses can be designed with variable $B_1$ band widths to achieve more uniform spatial encoding within that $B_1$ field. This is done by using a vector of relative subband widths in $B_{1,}$ that are proportional to the $B_1$ field gradient across space, to determine the $\beta$ filter bounds that produce uniform excitation band widths in space. The excitation patterns produced by the subbands are the basis for spatial encoding, as this creates unique signals between adjacent spins. Designing these subbands to have uniform width in space within an inhomogeneous $B_1$ allows for more uniform resolution for spatial encoding over the region of interest.

#### 3.2.1.2.2.1 $B_1^+$-selective Half-pulse

For $B_1^+$-selective pulses, the $A(t)$ waveform must have zero integrated area as mentioned above. To allow for robust excitation bands at higher flip angles, the frequency waveform created from the β filter is split and reflected creating a -/+/- $A(t)$ waveform. The length of these pulses is on the order of 3-10 ms, and because of this, is susceptible to RF waveform distortions that will be discussed in Chapter 5. To combat this, half-pulses were designed for a -/+ $A(t)$ waveform, and the frequency waveform was simply split (Figure 3.6).

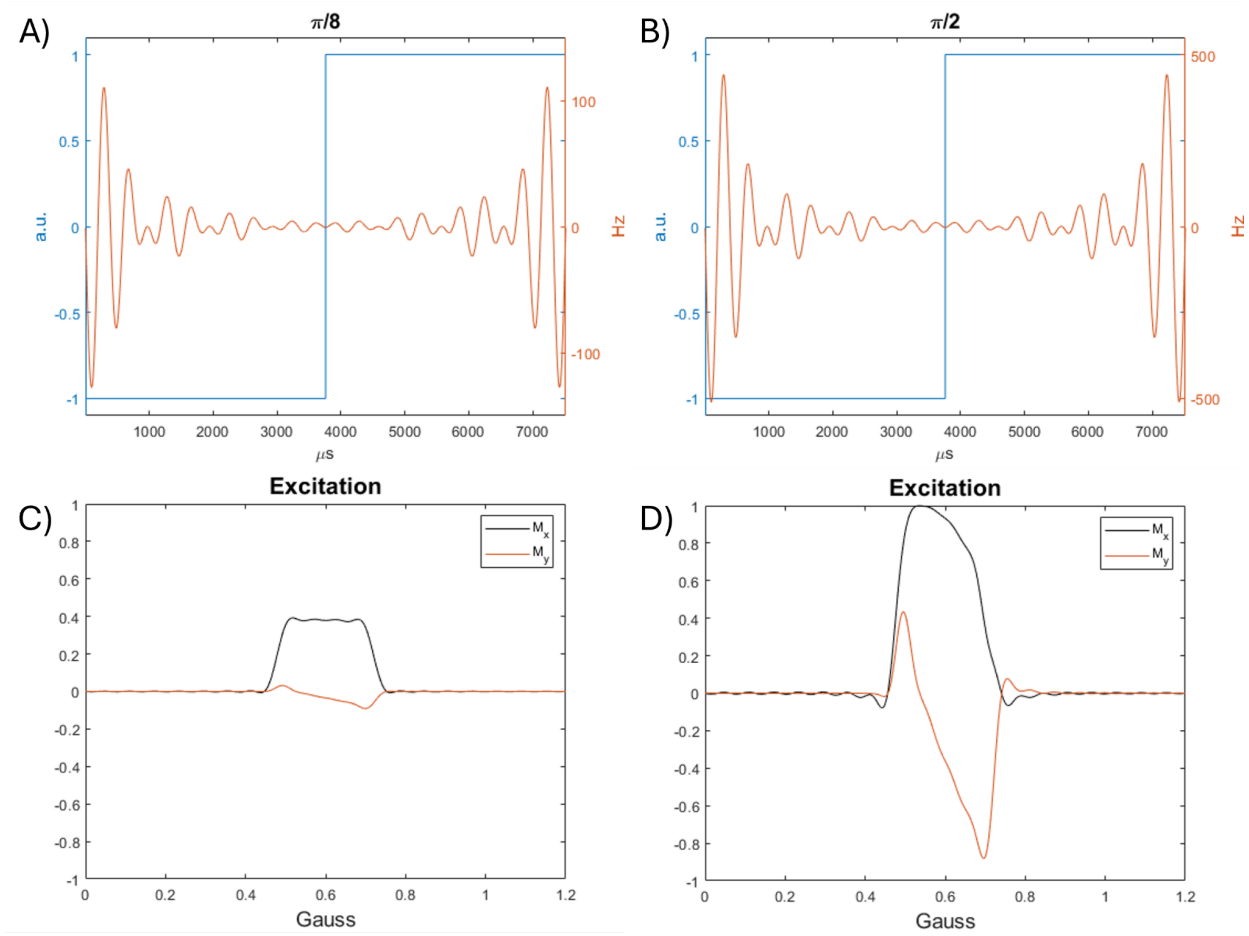


Figure 3.6: Amplitude and frequency waveform plots of a 7.5 ms-long single band $B_1^+$-selective half pulse with a passband center of 0.6 Gauss and a passband width of 0.25 Gauss with a flip angle of A) $\pi/8$ and B) $\pi/2$. $M_x$ and $M_y$ are plotted for the C) $\pi/8$ and D) $\pi/2$. The unwanted $M_y$ component becomes much larger for the $\pi/2$ flip angle, causing a distortion in the $M_x$ profile.

At higher flip angles $\alpha_I$ increases, creating unwanted $M_y^+$, breaking the $M_y^+ = 0$ assumption. For the -/+/- $A(t)$ waveform, the frequency waveform can be split and reflected, and played during the pre- and rewinding lobes of the $A(t)$ waveform, allowing the amplitude of the frequency waveform to be halved, minimizing the unwanted $M_y^+$ component. With the shorter -/+ $A(t)$ waveform, the amplitude of the frequency waveform can only be reduced by lowering the

flip angle, thus minimizing the unwanted $M_y^+$ component. These pulses will have distorted excitation bands at higher flip angles, but the pulses used were in the low flip angle regime. Since the excitations are performed in rapid succession, higher flip angles are not desirable because smoother flip angle schedules are less prone to errors between experiments and dictionary simulations.

#### 3.2.1.2.2.2 Bloch-Siegert Selective Excitation (BSSE)

A frequency selective pulse and an off-resonant Bloch-Seigert pulse can be combined to produce a $B_1^+$-selective excitation pulse (Martin et al., 2022). The resulting pulse works by using the off-resonance pulse to produce a frequency shift across an inhomogeneous $B_1$ range via the Bloch-Siegert shift, and the frequency selective pulse component then produces a frequency dependent excitation band which maps to the $B_1^+$ range. These two pulses are combined by simple summation, resulting in a Bloch-Siegert Selective Excitation (BSSE) pulse. An example pulse is shown in Figure 3.7, which is a 4.096 ms-long BSSE pulse with a 7 kHz BS off-resonance frequency, a passband center of 1.5 G and a passband width 0.5 G. The frequency selective component can be seen centered in the pulse causing oscillations on the flat amplitude portion of the off-resonance component pulse, which alone has a Fermi envelope shape. BSSE pulses are less sensitive to off-resonance than $B_1^+$-selective excitation pulses, but have around double the duration of the $B_1^+$-selective pulses proposed above. This increased duration is due to the need for a pre- and re-winder lobe to be added to the pulse for use in SENF so the accrued phase due to the off-resonant pulse component is rewound.

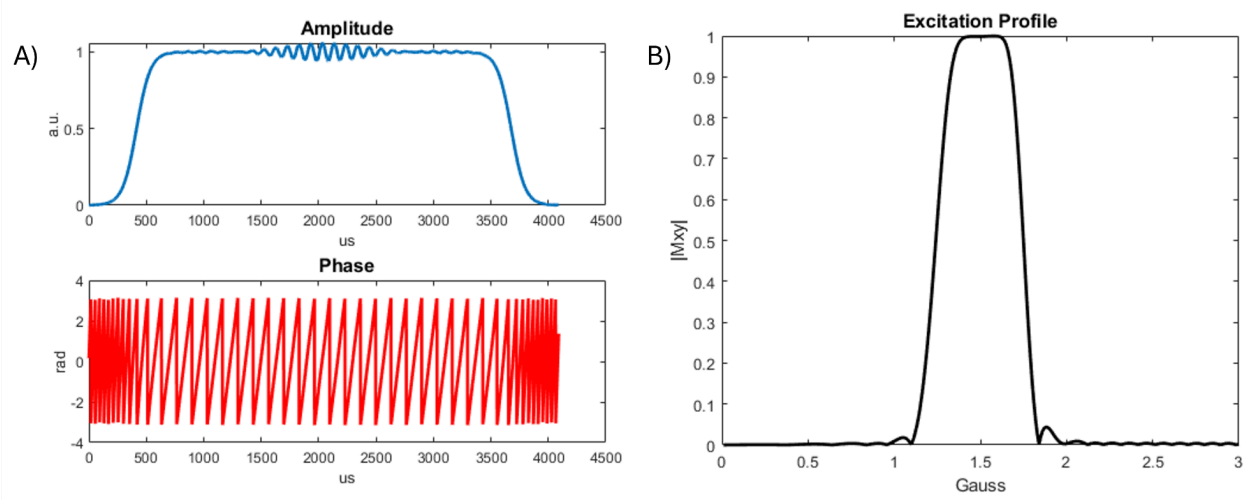


Figure 3.7: A) Amplitude and phase plots of a 4.096 ms-long BSSE pulse with a 7 kHz BS off-resonance frequency, a passband center of 1.5 G and a passband width 0.5 G. B) Excitation profile of the BSSE pulse.

#### 3.2.1.2.3 Off-resonance Bloch-Siegert pulses

Off-resonance Bloch-Siegert pulses can be used to induce spatially varying resonant frequency that induces a phase shift via the Bloch-Siegert shift along with an inhomogeneous $B_{1,}$ shown with Equation 2.5. Therefore, when transmitting an off-resonance pulse through an inhomogeneous $B_1$ field, a spatially dependent phase is accrued. If a square-root gradient solenoid is used, a linear phase gradient is produced across space, analogous to a traditional $B_0$ gradient (Srinivas et al., 2022). This phase gradient could be used to navigate k-space during data collection, like a traditional $B_0$ gradient. This phase gradient can also be used to encode spatial information into the time domain by quadratically sweeping the phase of an excitation pulse. This causes echoes to form at different times in the signal, depending on the spatial location within the phase gradient (Figure 3.8).

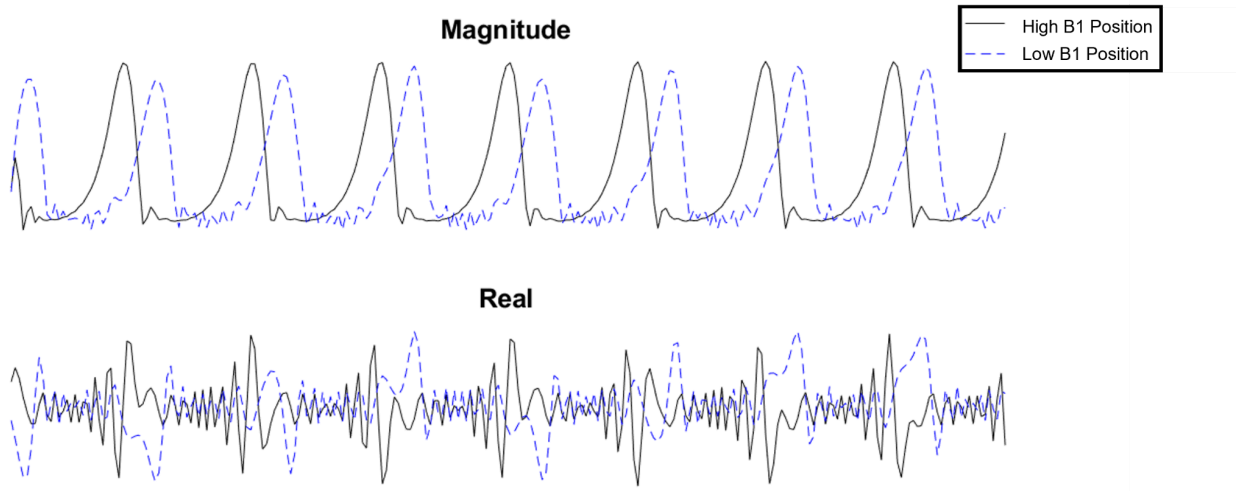


Figure 3.8: The magnitude and real components of signals for phantoms at two different $B_1$ field strengths for the qRF-BS SENF sequence. The two different $B_1$ field strengths are due to the phantoms being in two different positions within a linear gradient solenoid. The spins at the different positions have different frequencies due to the off-resonance pulse transmitted through the linear gradient solenoid due to the Bloch-Siegert shift. The phase of the excitation pulses used in the sequence is quadratically modulated so that echo peaks form in the signal at different times depending on the frequency of the spins. Therefore, the different spatial positions of the phantoms results in a time shift between the signals generated by those phantoms. The magnitude and real components are shown to highlight the time shift of the magnitude peaks and the difference in phase between two echo peaks that are adjacent in time.

#### 3.2.1.3 MRF-Type Sequence

Using multiple coil modes and at least one of the $B_1$-dependent pulse effects, spatial encoding can be achieved if these are implemented into an MRF-type sequence. These sequences consist of a rapid succession of excitations and acquisitions with varying parameters between each. These include flip angle, phase, and TR length for traditional MRF along with gradient encoding. For SENF, a unique coil mode and $B_1$ dependent pulse are used for each TR instead of gradient encoding. This provides the basis for the spatial encoding. At least one of the flip angles, phases and TR lengths are then varied to allow for additional encoding of quantitative information, such

as $T_1$ and $T_2$ relaxation and off-resonance. Figure 3.9 shows an example of a SENF sequence using 3 TRs. Two coils on the left and right side of the imaging ROI are used for transmitting one single band $B_1^+$-selective excitation pulse. The coil modes are varied by using one or both of the coils to transmit a pulse with the same amplitude weighting and without a phase weighting at each TR as follows: left coil only for the first TR, right coil only for the second TR, and both coils for the third TR. The $B_1^+$ fields and the excitation patterns for each TR are plotted in the top two rows. Three colored dots (red, yellow and blue) are overlaid onto the excitation pattern, indicating three voxels for which the signal will be monitored. The signal is plotted in the third row, showing that with a single pulse and three coil modes in a sequence with just 3 TRs, the signals for the three voxels are unique.

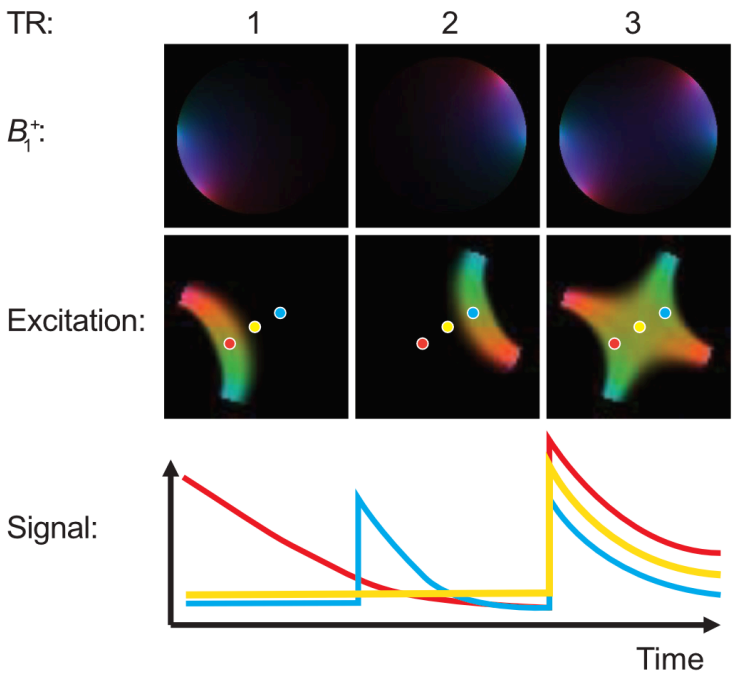


Figure 3.9: An example of the SENF encoding process for a two transmit coil setup for three voxels color coded in red, yellow and blue. The $B_1^+$ maps are shown in the first row, the excitation patterns in the second row, and time signals in the third row. A $B_1^+$-selective pulse is transmitted through the left coil, then the right coil, and finally both coils simultaneously. Each voxel has a unique signal after just three TRs.

#### 3.2.1.4 Quantitative and Spatial Reconstruction

The signals for different spatial locations and quantitative parameters are simulated using a Bloch simulation of the SENF sequence. The simulated signals are collected into a dictionary that spans both space and tissue parameters (Figure 3.10). A regularized pseudoinverse of the measured combined signal is performed with the dictionary to produce coefficients for each of the spatial location and quantitative parameter combinations. Coefficients below a certain threshold are rejected and the largest coefficient for each spatial location is chosen. These coefficients can be interpreted as being proportional to proton density. This was observed when reconstructing data for 1D experiments, where two phantoms with the same structure, but different relaxation parameters are reconstructed with similar coefficient magnitudes across multiple spatial positions. These reconstructions are discussed further in Chapter 5. The dictionary entry with the largest coefficient has an associated $T_1$ and $T_2$ value, which can be used to create quantitative parameter maps from a single acquisition and reconstruction. A regularized pseudoinverse and coefficient thresholding is not necessarily the best way the data could be reconstructed, but rather the first reconstruction technique used for the 2D SENF feasibility simulation and 47.5 mT 1D SENF experiments discussed in this thesis.

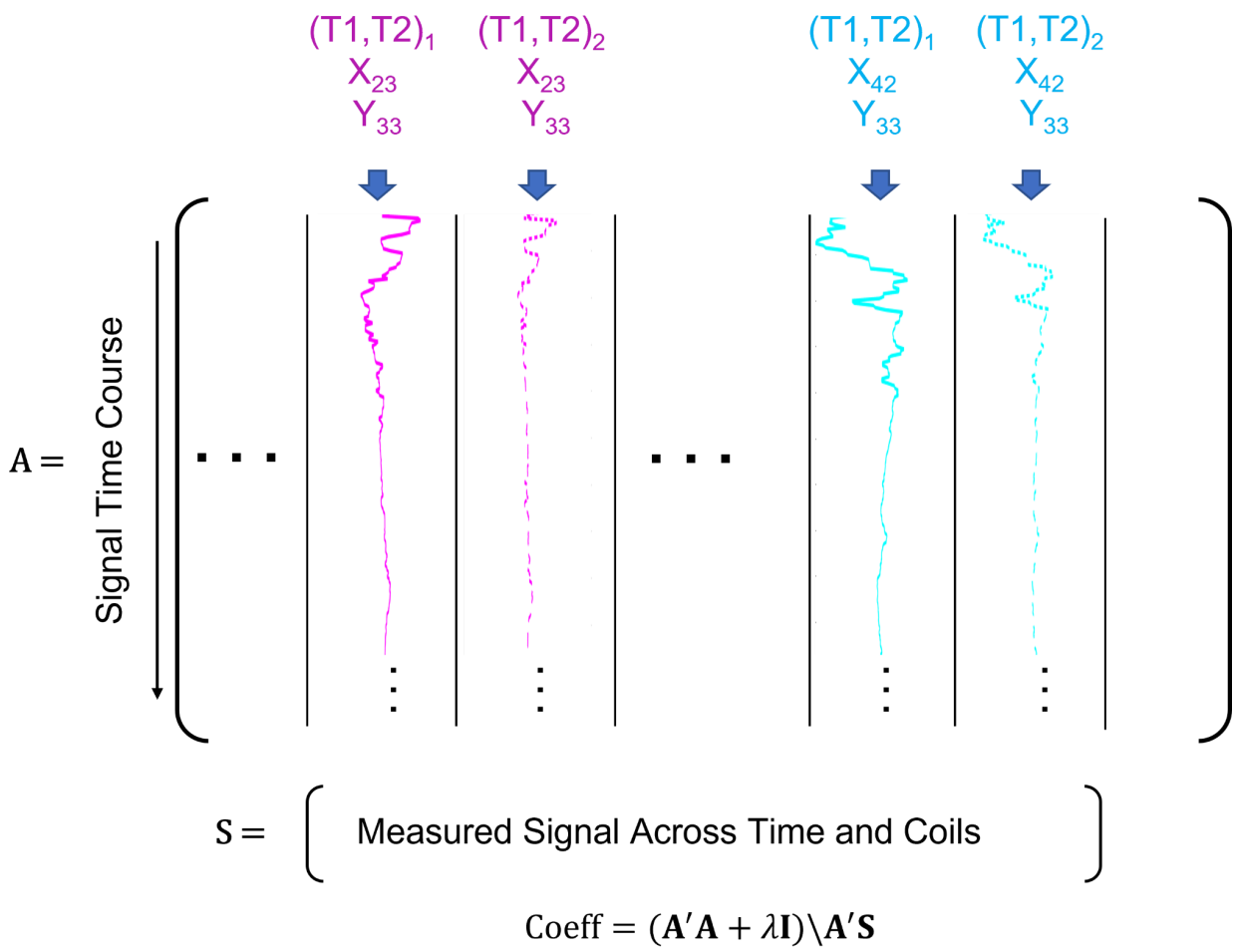


Figure 3.10: A SENF dictionary matrix. Its columns are the signals simulated for all possible spatial locations and $T_1/T_2$ value combinations. The rows are different time points. The regularized pseudoinverse used for reconstruction is shown.

### 3.2.2 2D Feasibility Simulation

#### 3.2.2.1 Overview

A 2D feasibility simulation was performed to validate the SENF concept by simulating signals from a 2D brain slice phantom, containing white matter, gray matter and CSF, and using a calculated $B_1$ map from an 8-coil pTx array used for conventional head imaging. This $B_1$ map produced an inhomogeneous $B_1$ and Hadamard $B_1^+$-selective pulses for an amplitude

$B_1$-dependent effect. The pTx array was chosen for producing inhomogeneous $B_1$ fields, to show SENF can be implemented with existing RF coils to produce complex excitation patterns. The $B_1^+$-selective pulses were chosen for SENF for the $B_1$ dependent effect, since they had been previously designed for RF encoding (Grissom et al., 2014). The sequence was designed with flip angle and TR schedules similar to those used in MRF to achieve quantitative encoding. The dictionary based reconstruction was inspired by MRF, with the addition of spatial location as another dimension in the dictionary and a simple regularized pseudoinverse was chosen as the reconstruction technique.

#### 3.2.2.2 Experimental setup

The $B_1$ fields of each coil on an existing 8-channel pTx in use on a conventional 3T MRI scanner were calculated with a Biot-Savart simulation. The $B_1$ field maps for each coil were modulated in amplitude and phase and superimposed on each other to create 64 different combined $B_1$ fields across the imaging volume. The amplitude and phase weights for the coils used to produce each unique combined $B_1$ field are referred to as coil modes. Hadamard $B_1^+$-selective excitation pulses with 32-subbands were designed to cover a 0 to 10 Gauss range of $B_1$ produced by the different combined $B_1$ fields. For Hadamard $B_1^+$-selective excitation pulses, a pulse was produced for each row of a Hadamard matrix and the sign of the excitation for each subband corresponded to the entries across the columns. Since Hadamard matrices are square, when designing 32-subbands, 32 unique pulses are produced to fully encode the passband. To cover a $B_1$ range of 0 to 10 Gauss the pulses were centered at 5 gauss with a passband width of 10 gauss total. A second set of 32 pulses was produced by shifting the passband center of the pulses by 0.15625 Gauss, or half of the subband width (10 Gauss/32 subbands = 0.3125 G) to cover 0.15625 to 10.15625 Gauss. This

was done with the intent of producing a superresolution effect, where spins experiencing $B_1$ values that differed in increments of 0.15625 Gauss or greater could be resolved, rather than the 0.3125 Gauss width of the subbands. The excitation patterns produced by the different pulse and coil mode combinations are shown in Figure 3.2B. Transmitting these pulses in a sequence caused adjacent magnetization, separated by $B_1$ field strengths of 0.15625 Gauss or greater, to produce incoherent, separable signals. The 4096 combinations of the 64 coil modes and the 64 Hadamard $B_1^+$-selective excitation pulses were shuffled randomly and each were used as an excitation within a simulated MRF-type sequence. A feature unique to $B_1^+$-selective excitation pulses is the ability to control the flip angle produced within the $B_1$ excitation band by scaling the frequency waveform of the pulse. This allows for independent control over the combined $B_1$ field produced and the flip angle produced within the $B_1$ excitation band. Using this independent control, the flip angle in each TR of the MRF-type sequence was varied according to a sine modulated flip angle schedule ranging from 0 to 90°s, while maintaining the encoding pattern produced by the coil mode and Hadamard $B_1^+$-selective excitation pulse for that TR. A flip angle schedule causes signals for different relaxation parameters to be incoherent and is used in MRF (Ma et al., 2013).

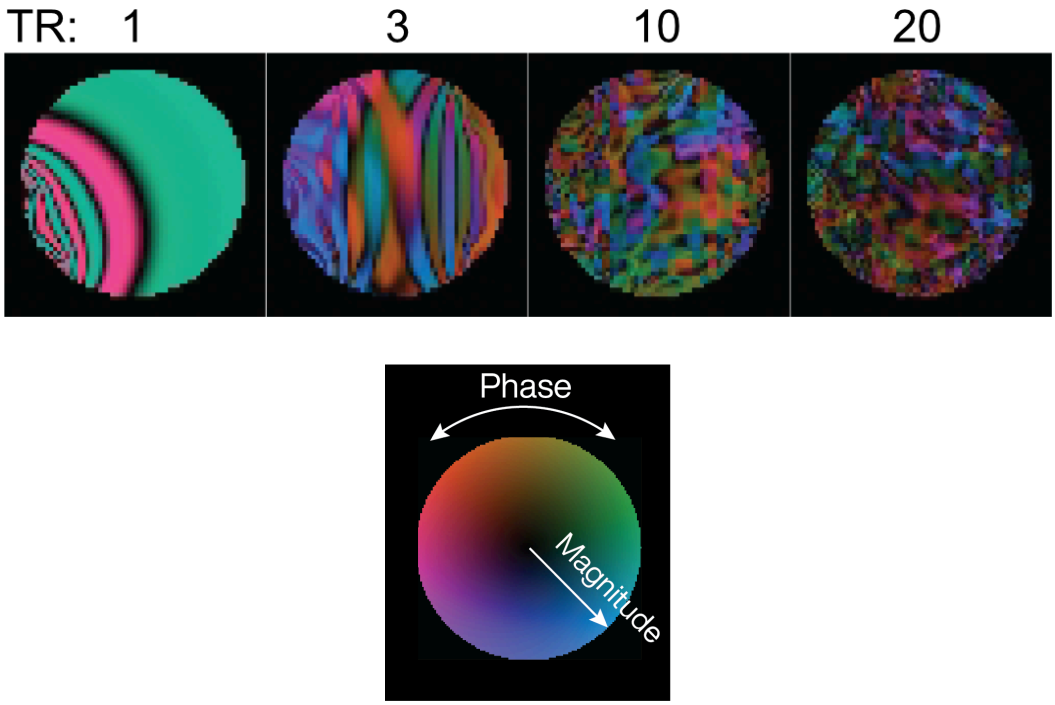


Figure 3.11: Magnetization ($M_{xy}$) of spins following 1, 3, 10 and 20 TRs of multi-band $B_1^+$-Selective Hadamard pulses played through different modes of the 8-channel transmit array from Figure 3.2. This magnetization is displayed here using a complex color wheel, showing how incoherence between voxels is quickly established.

To simulate measured data using this sequence, a digital brain slice phantom consisting of white matter ($T_1$=700 ms, $T_2$=60ms), gray matter ($T_1$=1000 ms, $T_2$=100 ms), and CSF ($T_1$=1800 ms, $T_2$=400 ms) voxels was centered within the 64 by 64 imaging FOV. A Bloch simulation was performed for each voxel of the brain slice phantom, using the relaxation parameters of the tissue present, the excitations it experienced in each TR and a single data point was collected at each TR, producing a signal with 4096 data points (equal to the number of voxels in the slice). The receive sensitivity maps of each of the 8 coils of the array were applied to the magnetization, each TR, to simulate receiving simultaneously with each coil of the array. This produced a measured signal vector 32,768 (4,096 TRs x 8 coils) data points in length.

The calculated $B_1$ map from an 8 coil pTx array was used for the simulation. The excitation patterns were made using 64 modes of the array, along with 64 $B_1^+$-selective pulses. These excitation patterns are the transverse magnetization of spins excited from equilibrium by a pulse and coil mode combination. An example of one of the 4096 complex excitation patterns is shown in Figure 3.2A.

#### 3.2.2.3 Image Reconstruction

A dictionary was simulated for each of the 64 by 64 voxels, for white matter, gray matter, CSF, and three confounding materials ($T_1$=400 ms, $T_2$=30 ms; $T_1$=1300 ms, $T_2$=100 ms; $T_1$=1700 ms, $T_2$=490 ms) amounting to 24,576 (64 x 64 voxels x 6 materials) signals. The signals were 4,096 data points in length and the sensitivity maps of the coils were, again, used to simulate the reception of the signal from the voxel onto each of the 8 coils, resulting in 32,768 data points for each signal. This amounted to a dictionary consisting of 32,768 rows by 24,576 columns. A regularized pseudoinverse of the dictionary was performed with the simulated measured signal to produce a vector of length 24,576 of coefficients for each combination of voxel and material. 64 by 64 coefficient maps of each of the six materials were made from this coefficient vector. A material was selected for each voxel based on the largest coefficient for that voxel. If the maximum coefficient for a voxel was below a threshold value, then the voxel was designated as air. Using the prior knowledge of the relaxation parameters of each material, along with the materials determined to be present at each voxel by the coefficients, $T_1$ and $T_2$ parametric maps were synthesized.

### 3.2.3 Comparison of three SENF sequences

#### 3.2.3.1 Introduction

*Overview*

Three SENF sequences were constructed in simulation using different $B_1$-dependent pulses: $B_1^+$-selective, hard pulse, and Bloch-Siegert for comparison against each other and against conventional $T_1$ and $T_2$ mapping methods. The SENF sequences were evaluated on two metrics: spatial resolution and minimum SNR. Spatial resolution was calculated by reconstructing a single delta function of mineral oil at a central position in the FOV and measuring the full width half max of a 1D reconstruction of each sequence's signal. The minimum SNR was defined as the SNR (Eq. 3.6) level required for an artifact-free reconstruction of a mineral oil and water ball phantoms placed adjacent to each other centered in the FOV. An artifact-free reconstruction was defined as a reconstruction with no coefficients above a defined threshold present outside of the expected bounds of the phantom. The threshold is defined as 20% of the peak coefficient amplitude. These metrics were also calculated for a $T_1$ inversion recovery sequence and a $T_2$ spin echo sequence using traditional $B_0$ gradients for comparison against traditional $T_1$ and $T_2$ mapping methods.

*Simulation Setup*

Each SENF sequence was designed for a scan time of ~2.3 seconds and a peak $B_1$ amplitude of 2 Gauss for scan time and power limits, respectively. A linear $B_1$ field over an 80 mm FOV was used for these simulations. A 1D simulation was performed for a 80 mm FOV at 1mm resolution for mineral oil and water materials and used to populate a signal dictionary. To synthesize experimental data for the minimum SNR metric, a 25 mm mineral oil ball centered at 25 mm and a 25 mm doped water ball centered at 50 mm were chosen as the phantom structure, similar to the experiments reported in Chapter 5. The entries corresponding to mineral oil ($T_1$=104 ms,

$T_2$=96ms) over the 12.5-37.5 mm range and gadolinium doped water ($T_1$=330 ms, $T_2$=220ms) over the 37.5-62.5 mm range were weighted by the expected spin density of the ball phantom shape and summed to synthesize the experimental data. Complex Gaussian white noise was added to the synthesized data at varying SNR levels, 1 to 100 in steps of 1, to produce multiple data sets.

$$SNR = \frac{S_p}{\sigma} \tag{3.5}$$

Here SNR is the signal to noise ratio, $S_p$ is the peak signal level in the data and σ is the standard deviation of the noise added. To reconstruct the data, a regularized pseudoinverse of the dictionary was applied to the synthesized data to produce coefficients for mineral oil and doped water for all spatial locations. Coefficients below 20% of the peak coefficient value were set to zero. The reconstructions were classified as artifact-free if no coefficients were present outside of the expected bounds of the phantoms.

For the resolution measurements, the mineral oil dictionary entry at the 25 mm position was used as the experimental data. A regularized pseudoinverse of the dictionary was applied to the data to produce coefficients for mineral oil and doped water over the 80 mm FOV. The full width half max of the mineral oil magnitude coefficient peak was measured as the resolution. The following sections will cover the SENF sequence designs that were used in the Bloch simulations of the signal dictionaries used for data synthesis and reconstructions.

#### 3.2.3.1 $B_1^+$-Selective SENF Sequence

The 2D feasibility simulation demonstrated the use of $B_1^+$-selective pulses for SENF. For this 1D simulation, a 3.76 ms-long 16-subband pulse with a passband center of 1 Gauss and a passband width of 2 Gauss was used, along with 16 more pulses produced by shifting the center of the

pulse by half of a subband width (passband center of 1.0625 Gauss). Eight different flip angles ranging from π/16 to π/2 radians were used. All permutations of the 32 pulses and 8 flip angles were randomly ordered to produce a sequence with 256 TRs 9.066 ms-long and a scan time of 2.3209 sec. A Bloch simulation of the sequence was performed to produce a signal dictionary and simulated experimental data as discussed above.

#### 3.2.3.2 Hard Pulse SENF Sequence

The hard pulse SENF sequence used hard pulse excitations, instead of $B_1^+$-selective pulses, to create a $B_1$ dependent amplitude effect on spin magnetization. High flip angle hard pulses are used to create banding patterns over the entire FOV and these patterns are modulated by changing the $B_1$ amplitude of the hard pulses. This is changed at each TR according to a flip angle schedule, which is the flip angle at the largest $B_1$ for the hard pulse used in each TR. For this simulation the hard pulse sequence used the flip angle schedule shown in Figure 3.12, with a maximum flip angle of 18.83 radians at the highest $B_1$ point and 322 TRs 7.19 ms-long for a total scan time of 2.3155 sec.

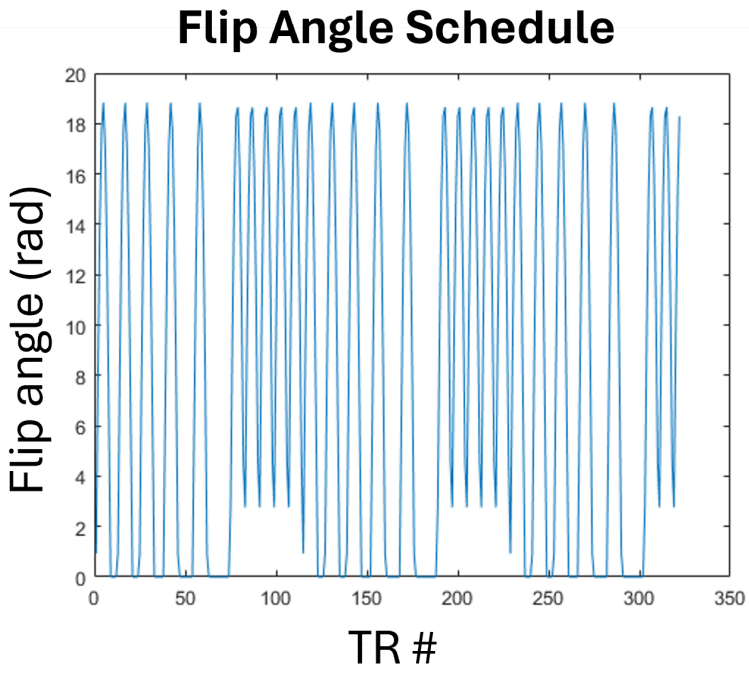


Figure 3.12: A plot of the flip angle schedule used for the hard pulse comparison simulation. This flip angle schedule consisted of 322 TRs with a peak flip angle of 18.83 rad at the highest $B_1$ point.

#### 3.2.3.3 Quadratic Phase Bloch-Siegert SENF Sequence

The qRF SENF sequence was inspired by recent qRF-MRF methods that simultaneously resolve resonance frequency offsets and tissue relaxation parameters (Boyacioglu et al., 2019). A combination of hard pulses with quadratically incremented phase transmitted through a coil with a uniform $B_1$ field and off-resonance Bloch-Siegert (BS) pulses, that induce a frequency shift transmitted through a coil with a linear $B_1$ field, were used to encode spatial information into the time signal. The $B_1$-dependent frequency shift induced by the BS pulses, played through the $B_1$ gradient coil, establishes a mapping from space, to $B_1$ field strength, to temporal frequency. The quadratically incremented phase of the hard pulses then sweeps the sequence's sensitivity repeatedly across a 1/TR Hz spectrum (Figure 3.8). For the 1D simulation, the sequence was

constructed in two halves. The first half consisted of positive polarity BS pulses and the second half consisted of negative polarity BS pulses. This was done so that the accrued phase due to the BS shift changes signs between the two halves of the sequence, enabling disambiguation of spatial encoding phase with off-resonant phase, which is required in practice. A sweep rate of 5.6° times $TR^2$ was used with 125 TRs for each half of the sequence for a total of 250 TRs 9.2 ms-long for a total scan time of 2.3 sec. The BS pulses were 9 ms-long, which caused the TR lengths to be longer, resulting in a smaller number of TRs for the same scan time as the $B_1^+$-selective and hard pulse sequences.

#### 3.2.3.4 Conventional $T_1$ and $T_2$ Mapping

##### 3.2.3.4.1 $T_1$ with Inversion Recovery

An inversion recovery sequence was implemented with 10 inversion times (TI) ranging from 2-3000 ms. The sequence comprised an inversion pulse, followed by wait times dictated by TI, then an 90° excitation pulse and finally an acquisition. An ideal inversion was used to simulate the inversion pulse with crusher gradients. No variable $B_1$ was used and a $B_0$ gradient was added to the Bloch simulation for frequency encoding. A gradient strength of 7 mT/m was used with 81 samples collected using a 125 $\mu$s dwell time (BW = 8 kHz) to match values used for conventional imaging on the 47.5 mT scanner. The simulated signals were collected into a dictionary and used to synthesize experimental data in the same manner as for the SENF sequences.

#### 3.2.3.4.2 $T_2$ with Spin Echo

A spin echo sequence was implemented with 10 echo times (TE) across a 7.5-1000 ms range. This sequence comprised a 90° excitation pulse, a wait time of TE/2, then a 180° refocusing pulse, another wait time of TE/2 and finally a frequency-encoded acquisition. As with the $T_1$ IR sequence, no variable $B_1$ was used and $B_0$ gradients were added to the Bloch simulation for frequency encoding. The same $B_0$ gradient parameters from the $T_1$ IR simulation were used. The signals were collected into a dictionary and used to synthesize experimental data in the same manner as for the SENF sequences.

## 3.3 Results

### 3.3.1 2D Feasibility Simulation

The coefficient maps for the three materials present in the simulated phantom (white matter, gray matter and CSF) have high coefficient values in voxels corresponding to the phantom structure (Figure 3.13A). When selecting the highest coefficient for each voxel with a coefficient rejection threshold, only two voxels (0.05%) outside of the brain were misclassified, that should have been thresholded (Figure 3.13B).

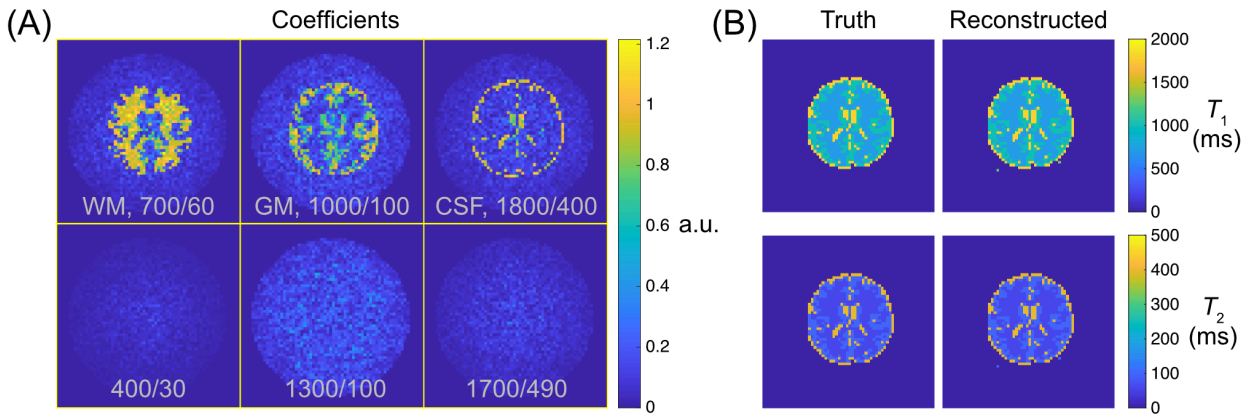


Figure 3.13: A) Coefficient maps for a simulated 64x64 2D SENF reconstruction of a brain phantom. The white matter, gray matter and CSF have high coefficient values, while the three confounding materials have very low coefficients. B) $T_1$ and $T_2$ maps were reconstructed by taking the highest coefficient for each spatial location. Only two voxels were misclassified outside of the brain.

### 3.3.2 Comparison of SENF Sequences

For the $B_1^+$-selective SENF sequence, the resolution achieved was 1 mm and the minimum SNR was 18 SNR. An artifact free reconstruction is shown (Figure 3.14A) with a plot of the sum of the coefficients across the 80 mm FOV versus the SNR level used to synthesize the signal from which they were reconstructed (Figure 3.14B). The delta function reconstruction used to calculate spatial resolution for the SENF sequence is shown (Figure 3.14C).

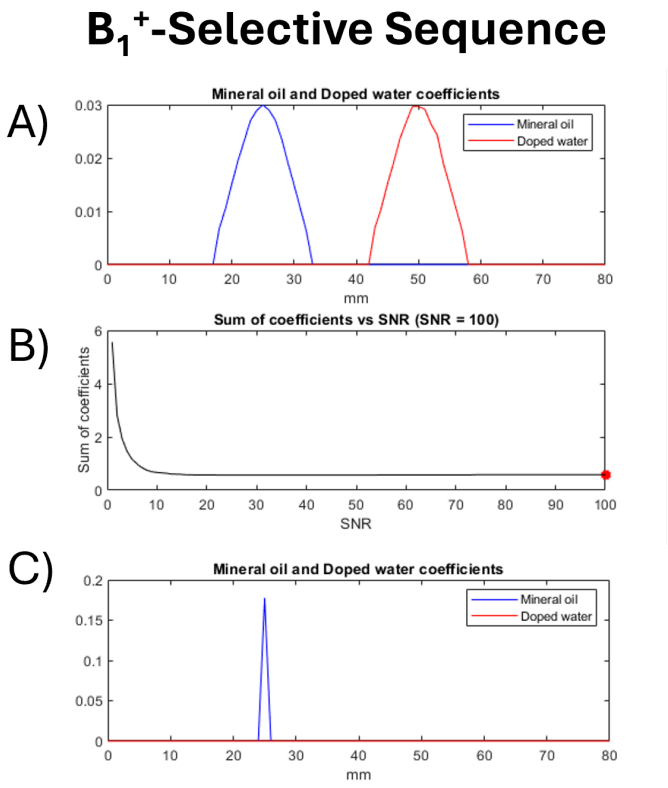


Figure 3.14: $B_1^+$-selective SENF sequence results. A) 1D coefficient map for mineral oil and water, B), a plot of the sum of the coefficients across the FOV vs SNR to visualize the minimum SNR, C) the reconstruction of a mineral oil delta function for resolution calculation (1 mm FWHM).

For the hard pulse SENF sequence, a resolution of 1 mm was achieved with a minimum SNR of 21 SNR (Figure 3.15). An artifact free reconstruction is shown (Figure 3.15A) with a plot of the sum of the coefficients across the 80 mm FOV versus the SNR level used to synthesize the signal from which they were reconstructed (Figure 3.15B). The delta function reconstruction used to calculate spatial resolution for the SENF sequence is shown (Figure 3.15C).

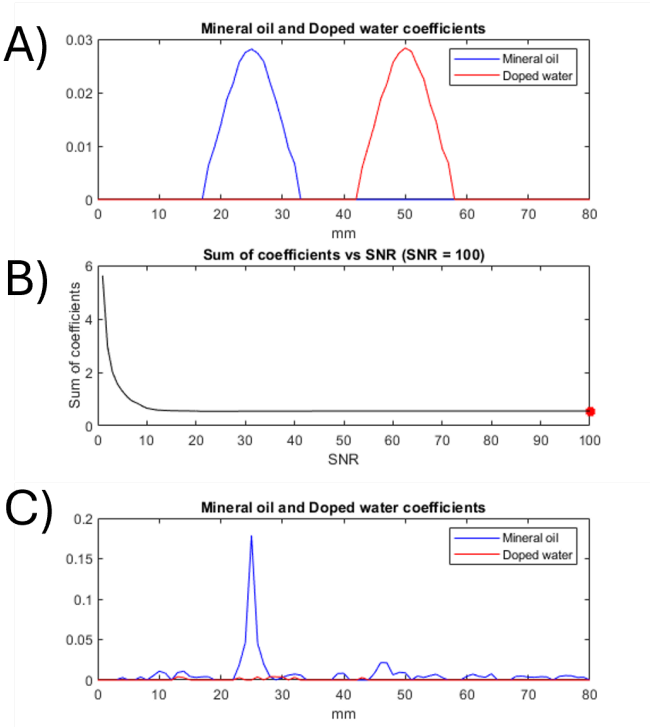


Figure 3.15: A) 1D coefficient map for mineral oil and water, B) a plot of the sum of the coefficients across the FOV vs SNR to visualize the minimum SNR, C) the reconstruction of a single delta function for resolution calculation (1 mm FWHM) for the hard pulse SENF sequence.

For the qRF-BS SENF sequence, the resolution achieved was 3 mm with a minimum SNR of 37 SNR (Figure 3.16). An artifact free reconstruction is shown (Figure 3.16A) with a plot of the sum of the coefficients across the 80 mm FOV versus the SNR level used to synthesize the signal from which they were reconstructed (Figure 3.16B). The delta function reconstruction used to calculate spatial resolution for the SENF sequence is shown (Figure 3.16C). The encoding for the qRF-BS SENF sequence is the most like Fourier encoding, and a higher resolution is asked of the reconstruction (1 mm) than what was encoded (3 mm), resulting in the side lobes seen in Figure 3.16C.

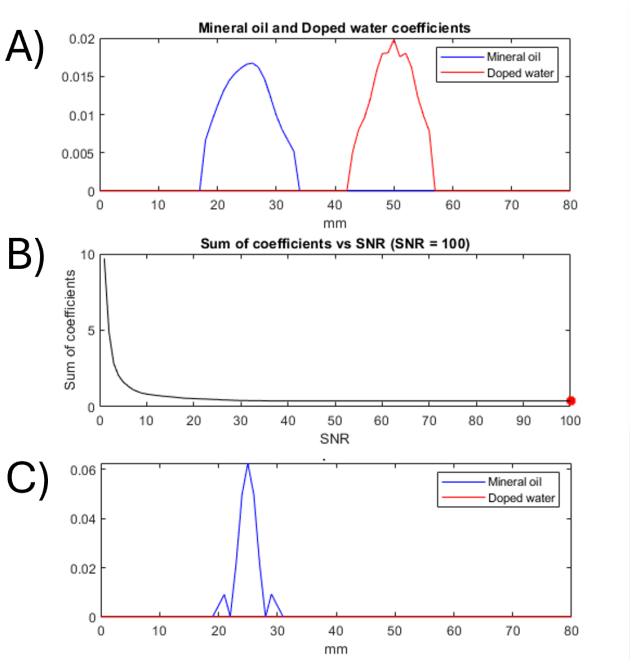


Figure 3.16: A) 1D coefficient map for mineral oil and water, B) a plot of the sum of the coefficients across the FOV vs SNR to visualize the minimum SNR, C) the reconstruction of a single delta function for resolution calculation (3 mm FWHM) for the qRF-BS SENF sequence.

For the $T_1$ IR sequence, a resolution of 1 mm was achieved with a minimum SNR of 6 SNR (Figure 3.17). An artifact free reconstruction is shown (Figure 3.17A) with a plot of the sum of the coefficients across the 80 mm FOV versus the SNR level used to synthesize the signal from which they were reconstructed (Figure 3.17B). The delta function reconstruction used to calculate spatial resolution for the SENF sequence is shown (Figure 3.17C).

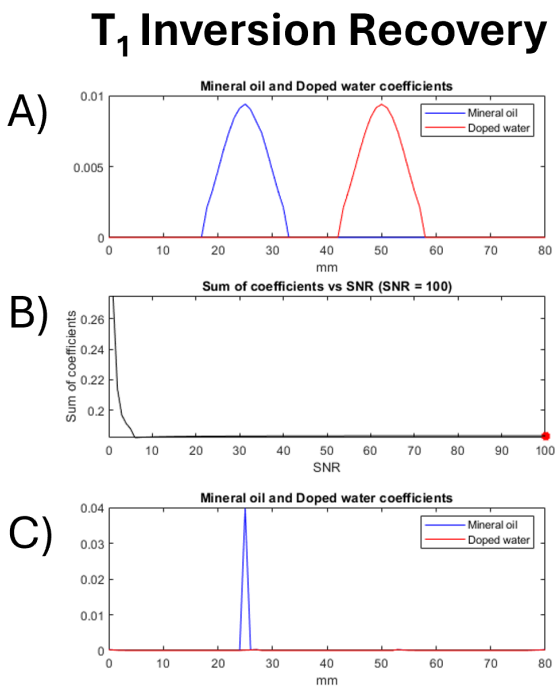


Figure 3.17: A) 1D coefficient map for mineral oil and water, B) a plot of the sum of the coefficients across the FOV vs SNR to visualize the minimum SNR, C) the reconstruction of a single delta function for resolution calculation (1 mm FWHM) for the $T_1$ IR sequence.

For the $T_2$ spin echo sequence, a resolution of 1 mm was achieved with a minimum SNR of 5 SNR (Figure 3.18). An artifact free reconstruction is shown (Figure 3.18A) with a plot of the sum of the coefficients across the 80 mm FOV versus the SNR level used to synthesize the signal from which they were reconstructed (Figure 3.18B). The delta function reconstruction used to calculate spatial resolution for the SENF sequence is shown (Figure 3.18C).

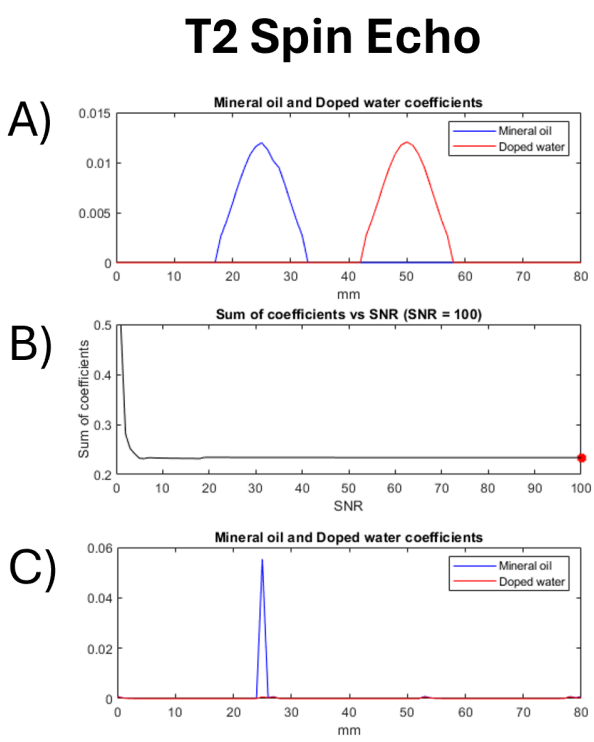


Figure 3.18: A) 1D coefficient map for mineral oil and water, B) a plot of the sum of the coefficients across the FOV vs SNR to visualize the minimum SNR, C) the reconstruction of a single delta function for resolution calculation (1 mm FWHM) for the $T_2$ spin echo sequence.

### 3.4 Discussion and Conclusion

This chapter introduced SENF, a new method of encoding MRI data that alleviates the need for $B_0$ gradients while simultaneously encoding spatial and quantitative parameters in a time-efficient manner. The components that make SENF possible are: an inhomogeneous $B_1$ field, pulses that create $B_1$ dependent effects within this field, a MRF-type sequence that causes signals to be incoherent between different spatial locations and tissues, and a dictionary based reconstruction that simultaneously produces spatial and quantitative information from measured signals.

SENF was validated in a 2D feasibility simulation where a 2D brain slice phantom was encoded and reconstructed using $B_1^+$-selective SENF. With three tissues present in the phantom

and three confounding tissues used to populate the dictionary, only two voxels (0.05%) outside of the brain were misclassified in the $T_1$ and $T_2$ maps that were reconstructed.

Three SENF sequences: $B_1^+$-selective SENF, hard pulse SENF and qRF-BS SENF were introduced and compared in a 1D simulation. According to the chosen metrics of resolution and minimum SNR, the hard pulse (1 mm, 21 SNR) and $B_1^+$-selective (1 mm, 18 SNR) sequences outperformed the qRF-BS (3 mm, 37 SNR) in both. This is most likely due to the 2.3 sec scan time limitation, since qRF-BS SENF requires the sequence to be repeated for two polarities of off-resonance pulses alongside the hard pulse excitations, which limits the number of unique encoding TRs over a fixed scan time period. All SENF sequences had comparable resolution (1-3 mm) to the traditional $B_0$ encoded $T_1$ (1 mm) and $T_2$ (1 mm) mapping sequences, but fell short in minimum SNR by a large margin (18-37 SNR vs 5-6 SNR). This is likely due to the lack of perfectly orthogonal spatial encoding that the fully Fourier encoded $T_1$ and $T_2$ mapping sequences enjoy. However, the SENF sequences provide full spatial and quantitative encoding in 2.3 seconds, while the $T_1$ and $T_2$ mapping sequences require a TR length of 5 $T_1$s (~1.5 seconds for the doped water), resulting in much longer scan times. Higher SNR levels can be achieved with EMI suppression techniques discussed in Chapter 1 and Chapter 4 to mitigate this downside.

The results of the proof-of-concept 2D simulation, as well as the SNR and resolution capabilities of all the SENF sequences were sufficient to move forward with experimental implementation of SENF on a 47.5 mT scanner. The SNR levels of 18-37 are achievable on the 47.5 mT scanner using EMI shielding discussed in Chapter 4. The 1-3 mm resolution is comparable to achievable resolutions with conventional $B_0$ gradient imaging on the 47.5 mT scanner with the ~7 mT/m gradients. The development of the hardware required for the

experiments is discussed in Chapter 4, and the experiments themselves are discussed in Chapter 5.

# CHAPTER 4: HARDWARE FOR EXPERIMENTAL VALIDATION OF SENF ON A 47.5 MT LOW-FIELD SCANNER

## 4.1 Introduction

Several RF gradient methods, in addition to SENF, have been proposed (Hoult, 1979; Sharp, 2010; Wright, 2009; Katscher et al., 2010; Torres et al., 2022), but currently there is no standard hardware platform (RF coils, EMI Shielding, TR switch) to implement these methods. Their high RF power requirements typically limit RF gradient methods to systems with lower $B_0$ field strengths, which are typically custom systems without access to standard clinical MRI hardware (Cooley et al., 2014; Srinivas et al., 2022). Furthermore, low-field scanners aim to make MRI more accessible and are typically not sited in a shielded room, like conventional high-field scanners, and may even be portable. This necessitates custom RF-shielding to reduce EMI levels so that the SNR levels are sufficient for clinically viable images.

RF gradient methods require spatial RF gradients in either magnitude or phase, produced by a variety of RF coil designs Some RF gradient methods require a single $B_1$ magnitude gradient (Hoult, 1979) or an array of $B_1$ magnitude gradients (Katscher et al., 2010; Wright, 2009). Others require one $B_1$ phase gradient (Torres et al., 2022; Hasselwander et al., 2017; Srinivas 2023 et al.; Srinivas 2022 et al.) or multiple phase gradients (Sharp, 2010). The flexible pulse design for SENF makes it compatible with any $B_1$ field gradient, allowing SENF to operate on a variety of hardware platforms.

This chapter will cover the development of phantoms, RF coils and EMI shielding for the experimental implementation of SENF on a 47.5 mT low-field scanner. Custom RF coils were developed to produce specific RF amplitude gradients for SENF spatial encoding. $B_1^+$-selective SENF can use non-linear $B_1$ fields while maintaining uniform encoding by designing pulses with

excitation bands that are uniformly distributed across space as outlined in Chapter 3, allowing for flexibility in coil designs. For hard pulse SENF, a linear $B_1$ amplitude gradient should be used to achieve uniform-resolution spatial encoding. For qRF-BS SENF, a square root $B_1$ field should be used to achieve uniform-resolution spatial encoding due to the squared dependence of the Bloch-Siegert phase shift on $B_1^+$. In this work, since two of the three methods required a linear RF gradient, a linear gradient solenoid was used for the experimental implementation of SENF, as this simplified the design of $B_1^+$-selective pulses for uniform encoding, enabled uniform-resolution encoding for hard pulse SENF, and has quadratically dependent encoding for qRF-BS SENF, which was mapped for reconstruction.

In Chapter 5, the experimental implementation of SENF on a 47.5 mT low-field scanner is reported. These experiments had several unique requirements which necessitated the design and construction of new phantoms, shielding and RF coils. These experiments represent the first implementation of SENF, performing 1D spatial encoding and quantitative encoding of two ball phantoms with different $T_1$ and $T_2$ relaxation properties (mineral oil and gadolinium doped water). The ball phantoms were also used for measuring $B_1$ and $B_0$ values at different points within the imaging field of view. To measure $B_1$ and $B_0$ maps, tube phantoms were also used across the imaging field of view, as well as used for testing spatial encoding when structures that varied over a single direction were included. To enable these experiments and measurements, RF gradient coils were constructed that produce a spatially varying $B_1$ field to allow for spatial encoding. These include simple loop coils and linear gradient solenoids for the testing of $B_1^+$-selective excitation pulses for the $B_1^+$-selective SENF sequence, as well as an optimized linear gradient solenoid providing uniform encoding for HP SENF sequence and quadratic spatial phase gradient for the quadratic RF Bloch-Siegert (qRF-BS) SENF sequence. RF coils

with uniform $B_1$ fields for uniform excitation are also necessary for the quadratic RF Bloch-Siegert (qRF-BS) SENF sequence discussed in Chapter 3. Uniform receive coils that are close-fitting to the ball phantoms for maximal receive signal levels are used for these experiments, with the optimized linear gradient solenoid. Custom EMI shielding was also developed to reduce environmental noise to levels that were low enough to not disrupt the spatial and quantitative encoding of SENF. The experiments further necessitated the repositioning of phantoms between acquisitions. Shielding was constructed that allowed for simple access to repositioning phantoms without disrupting the experimental setup. This chapter describes the 47.5 mT scanner platform used in these studies, followed by the design of the EMI shielding and a Reed relay TR switch, and finally the several RF coils that were used in the above-described experiments as well as an an optimized linear gradient solenoid and its 3D-printed components.

## 4.2 Methods

### 4.2.1 47.5 mT MRI Scanner

The validation experiments were performed on a SIGWA 47.5 mT low-field permanent magnet. The magnet has an open design with a 40 $cm^3$ FOV with a 18.7 ppm homogeneity, corresponding to a 37.8 Hz off-resonance range across the entire imaging volume. The SENF validation experiments took place in a centered 8 $cm^3$ imaging volume, which was centered within the magnet using a patient table. This smaller volume, having reduced $B_0$ inhomogeneity and the position of the imaging volume being near the center of the bipolar magnet, which is more homogeneous, resulted in off-resonance values of < 10 Hz due to the reduced inhomogeneity of $B_0$. The magnet has three orthogonal planar $B_0$ gradient coils that are embedded on the surface of the magnetic plates. These gradients have a maximum strength of 7 mT/M and at this low-field

strength are susceptible to concomitant gradient fields that can produce artifacts with conventional gradient-encoded imaging. Permanent magnets are subject to field strength drift as temperatures change, which were measured on the 47.5 mT magnet by measuring an FID signal produced by a 90° excitation, followed immediately by an acquisition, every 30 min and taking the Fourier transform of the FID to obtain the center frequency. We empirically observed that the center frequency drifted faster when it started at higher Larmor frequencies in an experiment, most likely due to heating of the magnet. If experiments were performed starting at these higher frequencies, then an FID was collected at the beginning of each TR within a sequence so the drift could be accounted for in dictionary simulations. At lower center frequencies the drift was slow enough to be negligible during a SENF sequence and the center frequency could be simply adjusted before each experiment with a standalone FID measurement.

A Tecmag Redstone spectrometer was used with TNMR software for hardware integration. The TNMR software allows for event based sequence programming. An event duration was defined, then outputs or inputs for any channels on the spectrometer (TTL, transmit, receive, gradient) were defined for that event. These outputs were then defined in over multiple dimensions (1D, 2D, 3D, and 4D), which were used along with control looping structures to determine the event ordering of a sequence. Any complex RF pulse (quadratic phase hard pulses, $B_1^+$-selective, Bloch-Seigert) was implemented via phase (0-360°) and amplitude (0-100 a.u.) tables. The spectrometer has two transmit channels, outputting a maximum 1.4 $V_{pp}$ signal fed to Tomco RF amplifiers (250 W, 500 W, 2 kW), as well as three receive channels on which Miteq preamplifiers were used. The amplifiers are connected to a TR switch (passive cross-diode, reed relay) allowing coils to be used in transceiver mode and providing additional isolation for the receive channels when using multiple coils. The TR switches used will be

discussed in a later section. The spectrometer also provided gradient driving signals for AE Techron 2120 gradient amplifiers used for conventional $B_0$ imaging.

### 4.2.2 EMI Shielding

The magnet is sited in an unshielded room in the basement of a hospital, allowing for many sources of electromagnetic interference to be present within the imaging volume of the magnet. While sources within the room can be limited or shielded themselves, external sources from equipment within the hospital are still present. These external sources are operated at different times throughout the day or week resulting in a time of day-dependent EMI within the imaging volume. The time of day-dependent EMI can be accommodated by planning experiments at times of the day where noise levels are lowest and by using adequate shielding within the magnet to reduce the overall impact of EMI. Without any EMI shielding, even a simple FID acquisition using a simple uniform solenoid, housing a 50 ml tube phantom, required over 5000 averages to obtain a visible FID. This equates to an SNR level of only 2 or 3. Even $B_0$ encoded 1D imaging would be impossible at those noise levels, as NMR signal would be further reduced as it is spread across different precession frequencies spatially, while the EMI noise remains approximately constant. While SNR in the presence of stable noise can be improved with a large number of averages, EMI does not generally have stable statistics and time of day-dependent EMI, along with the magnet drift, will further corrupt the measurements made with longer pulse sequences. Therefore, custom shielding had to be developed to house the RF coils and phantoms used for SENF experiments to prevent as much EMI as possible from reaching the receiver.

#### 4.2.2.1 FR4 Box

Two different shields were developed for phantom experiments. These shields were fully closed around the experimental setup with female-to-female BNC feedthroughs for RF coil connections to suppress EMI. The first shield was a 18 $cm^3$ box made of copper-clad FR4. FR4 is woven glass-reinforced epoxy laminate material, which is available with a copper foil coating of a certain thickness. A lid with a 5 cm overlap was used as an opening on one side to allow for positioning of the experimental setup within. This box acted as a Faraday cage, significantly reducing EMI. The box was made with 18 $cm^3$ dimensions to allow for coils to be placed away from the walls of the shield to prevent coupling. To account for any coupling between the coils and the shielding, the coils were fixed within the shield and tuned inside of the shield and magnet before use. The main consideration for the shielding material was the copper thickness, which for the 2 oz copper FR4 used was 0.0696 mm. The skin depth effect describes how deeply EMI of a certain frequency will penetrate a given material (Eq 4.1).

$$\delta_s = \sqrt{\frac{\rho}{\pi f \mu_r \mu_0}} \tag{4.1}$$

Where $\delta_s$ is the skin depth, $f$ is the frequency of the EMI, $\mu_r$ is the relative permeability, $\mu_0$ is the absolute permeability and $\rho$ is the resistivity. The 47.5 mT magnet operates at 2.022 MHz and EMI at this frequency would require a skin depth of 0.047 mm. Therefore a shielded box constructed of FR4 had adequate skin depth for the operating frequency of the magnet. The thin skin depth of the copper was also helpful for reducing eddy currents when $B_0$ gradients were used for imaging. Two grounded BNC feedthroughs were used to connect the transmit and receive coils inside to an external Reed relay TR switch (Figure 4.1), which was connected to the Tecmag Redstone spectrometer.

The FR4 shield was used for two experiments: 1) using 8-subband Hadamard $B_1^+$-selective pulses to perform slice encoding, and 2) a sweeping band 1D spatial encoding experiment. The shield was also used for experimentally measuring $B_1^+$-selective excitation profiles. These uses are discussed further in Chapter 5. For some SENF experiments, it is necessary to reposition the phantom between acquisitions so that data may be taken for multiple phantom positions and configurations within the FOV, according to the experimental protocols that will be discussed in Chapter 5. To accomplish this with the FR4 shield, the lid had to be removed and replaced for each experiment, which significantly increases the time it takes to run a SENF experiment. The structural integrity of the lid was fairly weak, requiring frequent repairs due to the opening and closing of the box. It was also desirable to have a lid that could be easily opened from the front of the magnet rather than the top, so the operator does not have to climb onto the patient bed for each phantom reposition. To overcome these problems, a second shield was constructed as described below.

#### 4.2.2.2 Copper-clad Acrylic Shielded Box

To facilitate experiments, it was pertinent to have a simpler mechanism to open and close the shielding for repositioning of the phantoms. A shield was designed by our group for easier access to experimental setups and with greater structural integrity. A copper-clad acrylic box with a length of 30 cm length and a height of 16 cm with a trapezoidal shaped roof was used with a hinged door. 9 oz copper was used, which has a thickness of 0.3132 mm, and 2 mm acrylic sheets were used. Aluminum slats were used to hold the acrylic plates together along with super glue adhesive. This significantly improved the structural integrity of the shield, allowing for much more use before damage to the lid required repairs. In addition to these shields, copper

cloth and mesh were used to cover any gaps in the shielding to further mitigate EMI. Components for the EMI shielding, TR switch and the RF coils were mostly purchased through McMaster and DigiKey.

### 4.2.3 Reed relay TR switch

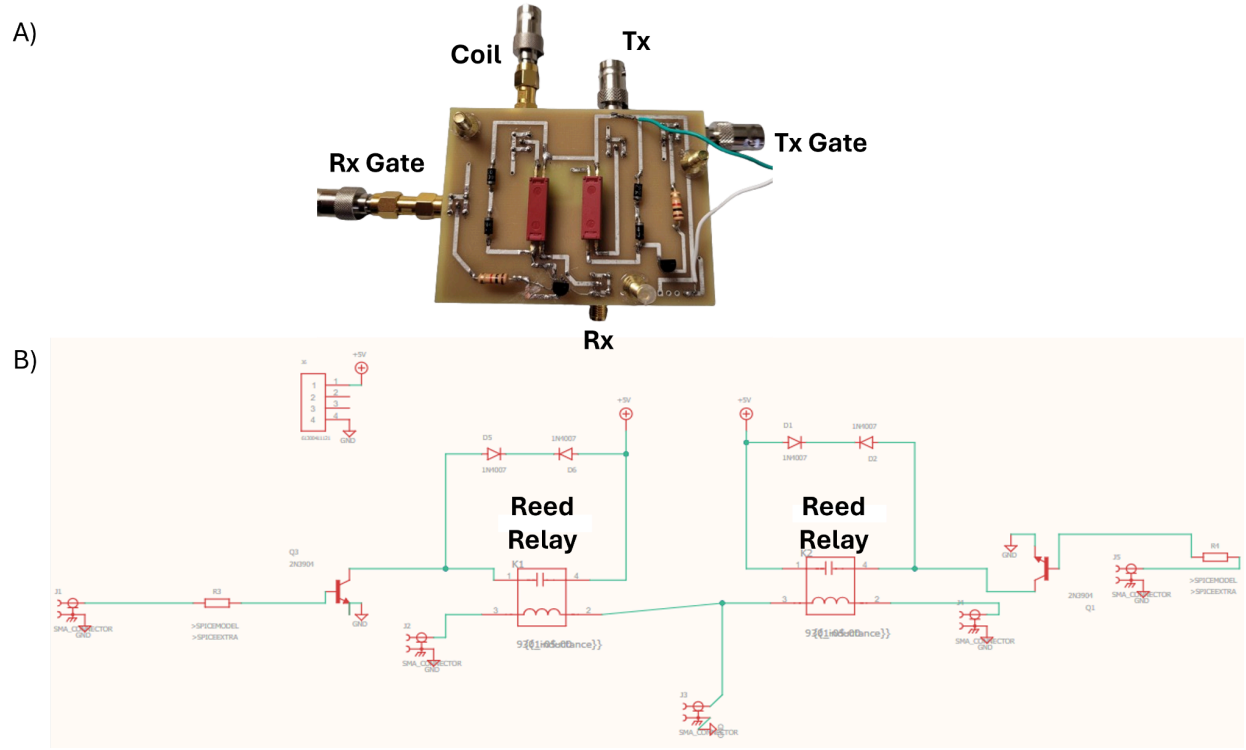


Figure 4.1: A) Reed relay TR switch used for SENF experiments. B) Circuit schematic of the reed relay TR switch.

The reed relays use reed switches, which are ferromagnetic metal housed in glass tubes, and are actuated by an electromagnet to open or close. The physical actuation of the metal takes around 250 ms, making the switch much slower than a pin diode switch, which can switch on the order of microseconds. Pin diodes have low resistances at the Larmor frequencies of low-field magnets, leading to poor isolation when implemented in a switch. Reed relays can operate under

high voltages (200 V) and currents (15 A) when switched on and have strong isolation (~40 dB) when switched off. This 40 dB isolation in addition to the 30 dB geometric decoupling provided 70 dB isolation between transmit and receive coils used in a nested coil design. The nested coil configuration used for SENF experiments will be discussed later in this chapter. Passive crossed-diode TR switches are another option that was used initially, but cause waveform distortions at low power levels (Straney et al., 2021). To operate the reed relay switch,a 5 V TTL signal was sent to either the $R_x$ or $T_x$ gate port, which switched a transistor that connects the 5 V power rail to the leads to the reed relay that closing the switch shorting the $R_x$ or $T_x$ port to the coil port. When the gating signal was not present, the paths were open, providing the 40 dB isolation.

### 4.2.4 RF Hardware Designs

#### 4.2.4.1 Loop Coil: Gradient-Free Imaging Using Hadamard $B_1^+$-Selective Excitation Pulses

RF transmit and receive coils were designed to be placed within this shielding. For SENF, the transmit coil needs to produce an inhomogeneous $B_1$, which can be accomplished with several coil geometries. For testing of the $B_1^+$-selective pulses, two coils were used. The first was a 10 cm diameter single-loop coil, which produced a 1/x $B_1$ field along the x direction. The loop coil was used for a Hadamard $B_1^+$-selective slice encoding experiment reported in Chapter 5. This coil had two limitations, the first of which was a limited $B_1$ strength (~1 G with a rapid ~1/x drop moving away from the coil) due to its large diameter and single winding. The second limitation was that the receive sensitivity decreased rapidly away from the coil, which led to low SNR towards the ends of the FOV.

#### 4.2.4.2 Variable Pitch Solenoid: Verification of $B_1^+$-Selective Pulse Excitation Profile and sweeping band 1D spatial encoding experiment

To solve both of the above problems, a 19-winding smaller 4 cm-diameter linear solenoid 12 cm in length was made. The tighter form-fitting geometry and increased winding density allowed for higher $B_1$ strength with less current and higher signal levels for receive. This gradient solenoid was used for a sweeping-band 1D spatial encoding experiment reported in Chapter 5. However, this coil still had a non-uniform $B_1^-$ field and poor $B_1^+$ linearity toward the outer diameter of the solenoid. This caused reduced SNR towards the lower winding density section of the coil and inhomogeneous excitation in the cross section of the phantoms, which was not desired for the 1D SENF projection experiments.

### 4.2.5 Optimized nested RF coil

#### 4.2.5.1 Winding Optimization

To overcome the limitations of the 12 cm solenoid, a larger linear solenoid was developed that produced a more linear $B_1$ field over a ~3 cm central diameter, accommodating 2.5 cm ball phantoms. The coil was designed with an optimization method adapted from Shen et al., which was a linear programming based optimization. First, a Biot-Savart calculation was performed for a 12 cm single loop to obtain its $B_1^+$ field. This $B_1^+$ field was placed at N = 40 fixed positions along the x-axis of the coil former, which were evenly spaced by 5 mm along the coil's 20 cm length. The 5 mm spacing was the minimum required to print robust grooves for the 20 gauge wire that was to be used. A $B_1^+$ field that was linear along the x-axis and uniform over a 3x3 cm cross section of the yz plane was used as the target field ($B_{targ}$). The number of coils at each

groove ($I_m$) were allowed to be $0 \leq I_m \leq 4$. A normalized error tolerance constant $\delta$=0.05 was used to satisfy Eq 4.2:

$$\frac{1}{n}\sum_{i=1}^{n}\frac{B_{x,i}\cdot I_m - B_{targ}}{B_{targ}} \leq \delta \quad (4.2)$$

The fixed positions for the single loop $B_1^+$ fields for the optimization were along the x-axis $\{(x_i, 0, 0)\}_{i=1}^{n}$ .

#### 4.2.5.2 Nested Coils

A nested 10 cm-long, 3.5 cm-diameter saddle receive coil was constructed for use with the optimized gradient solenoid. This coil produced a uniform $B_1$ field over the 8 cm imaging volume used for SENF experiments. This saddle coil was used as a transmit coil for the hard pulse excitations for qRF-BS SENF and as a receive coil for both hard pulse SENF and qRF-BS SENF. This is further discussed in Chapter 5. The saddle coil was oriented to produce a $B_{1y}$ field, while the optimized gradient solenoid produced a perpendicular $B_{1x}$ field. When oriented in this way, the coils were geometrical decoupled, which was measured via an S21 measurement between the transmit and receive coils.

#### 4.2.5.3 Structural Design

A coil holder was developed to position the saddle coil centrally in the linear solenoid. The holder had a central cylinder to hold the saddle coil, an outer ring with four prongs and a stopper to place the saddle along the correct depth. The inside of the central cylinder of the coil holder was made large enough to fit a phantom holder and had a stopper at the end so the phantom holder could be consistently at the correct depth. The phantom holder was a half cylinder with

2.5 cm-wide compartments that hold the 2.5 cm-diameter ball phantoms. This allowed positioning of up to 4 ball phantoms at different positions and also for the placement of 1 or 2 ball phantoms and sliding the phantom holder to different positions within the gradient coil. The placement of 4 ball phantoms and sliding multiple ball phantoms was used for the SENF 1D projection experiments. The entire setup was positioned inside the shield on a foam pad to prevent strong coupling between the coils and the shield. If coupling occurred it would otherwise shift the coil's tune and match. Additionally, linen sheets were used to stabilize the coil to prevent it from rotating, because the feet that were designed on the former were too small to prevent rotation on their own.

## 4.3 Results

### 4.3.1 47.5 mT magnet properties

The center frequency shifts spanned 1500 Hz over a three-day period (Figure 4.2), with an average drift of 0.42 Hz/min. The drift rate is faster at higher Larmor frequencies. This drift had minimal impact on SENF sequences since the acquisitions were only a few seconds in length per average, with less than 16 averages used causing drifts of <1 Hz over a sequence.

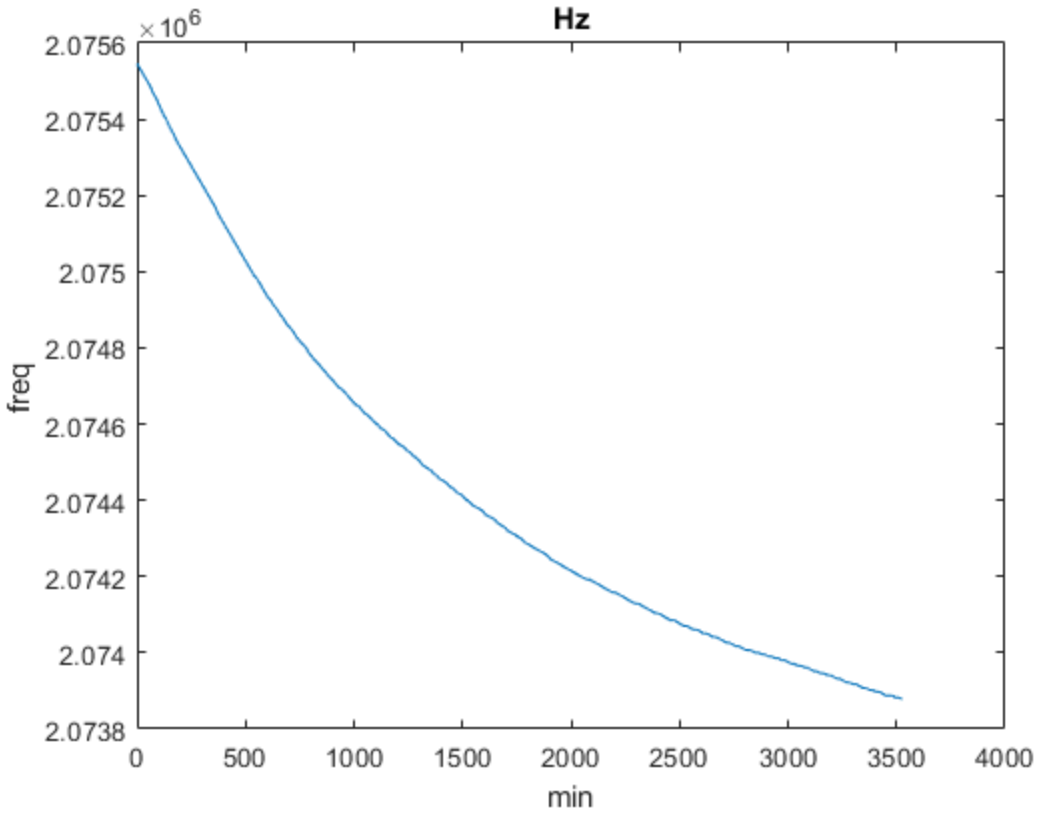


Figure 4.2: A plot of Larmor frequency measurements taken at 30 min intervals over a 60 hour period. Drift occurs at a faster rate at higher Larmor frequencies with an average rate of 0.42 Hz/min.

### 4.3.2 EMI Shielding

Figure 4.3 shows magnitude data from a single readout using identical coil and shielding. The RMS of the noise is 8.8 times higher on Day 2 than Day 1, showing an example of day to day EMI variation described in the methods.

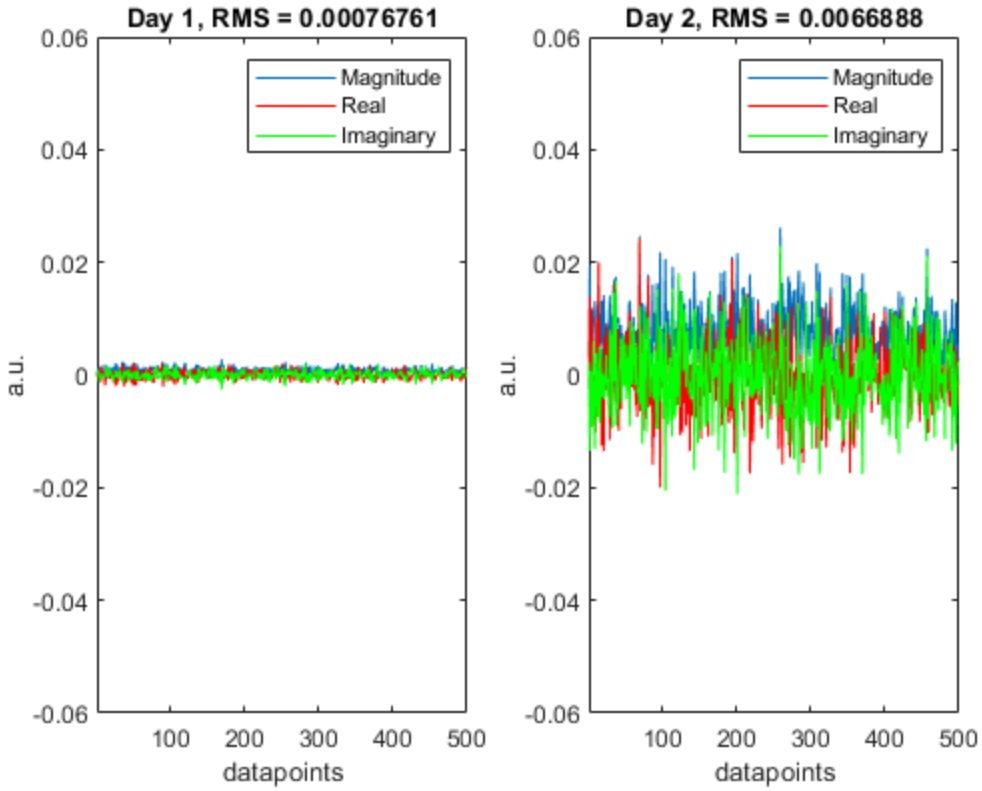


Figure 4.3: Single readout EMI measured on two different days on the 47.5 mT magnet using the same coil and shielding setup. The RMS of the noise is 8.8 times higher on Day 2 than Day 1.

In Figure 4.4, the constructed 18cm$^3$ FR4 shielded box is shown centered in the 47.5 mT low-field magnet. The lid opens at the top of the box, making repositioning of the experimental setup cumbersome.

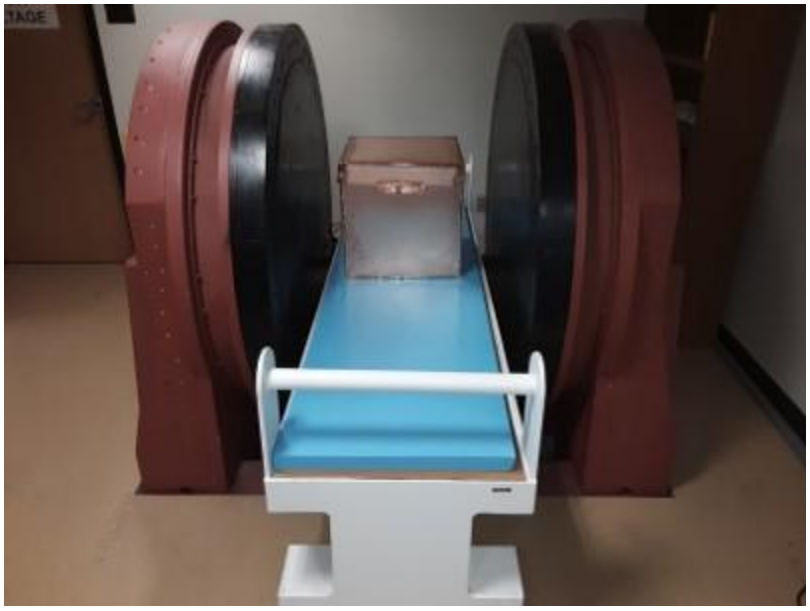

Figure 4.4: The first-generation FR4 shielded box inside of the 47.5 mT low-field scanner.

Figure 4.5 shows the copper-clad acrylic shielded box centered in the 47.5 mT magnet with a front-facing hinged door for easy repositions of phantoms between acquisitions. Repositioning was frequent in the SENF experimental protocols discussed in Chapter 5, where the phantoms were positioned at 5 mm increments throughout and 8 cm imaging volume, collecting data at each position.

Figure 4.5: The copper-clad acrylic shielded box inside of the 47.5 mT low-field scanner.

The EMI levels in the copper-clad box had a RMS that was 2.5 as large as the EMI levels in the FR4 shielded box (Figure 4.6). This was most likely caused by poor electrical connections between sections of the shields leading to ground loops between sections mitigating varying amounts of EMI.

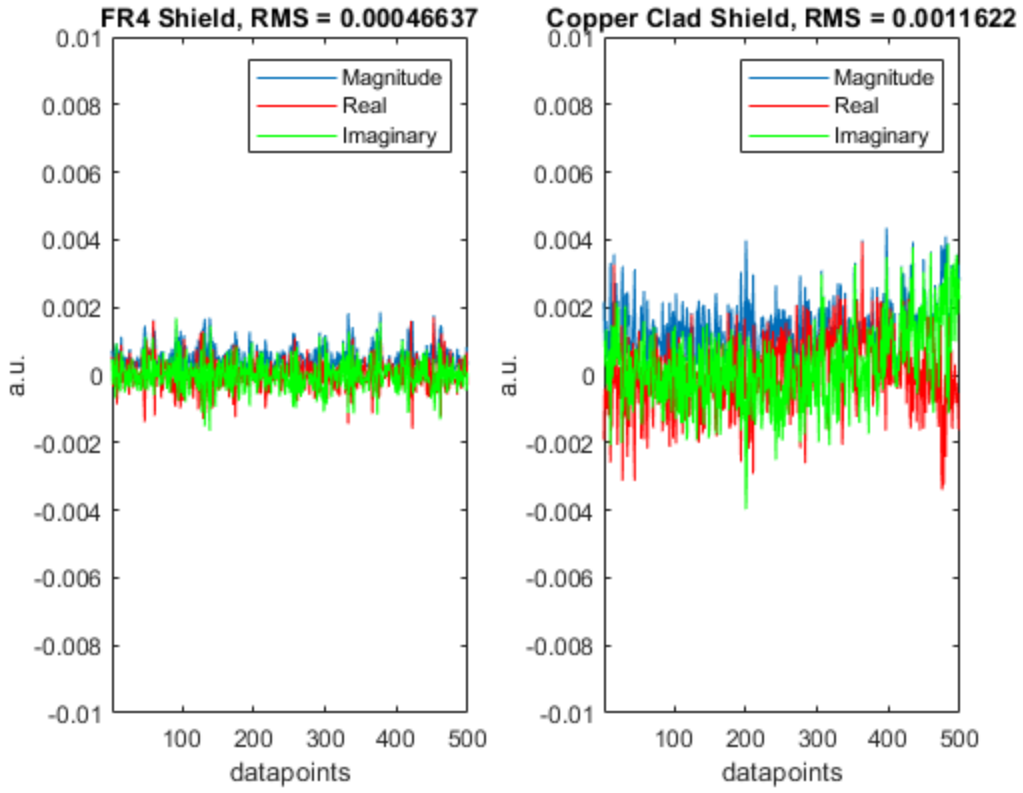


Figure 4.6: Single readout EMI comparison between the FR4 shield and the copper-clad shield. The RMS of the noise is 2.5 times as large in the copper-clad shield.

To achieve comparable SNR, four times the number of averages were used with the copper-clad shield, as the structural improvements outweighed the loss in SNR.

### 4.3.3 RF Hardware Designs

Figure 4.7 shows the final 10 cm loop coil using the tune match circuit described in Chapter 2 positioned inside the FR4 shielded box, providing a $B_{1x}$ field for transmit and receive. The experimentally measured $B_1$ field (0.1 - 1.1 Gauss) with an approximate 1/x shape.

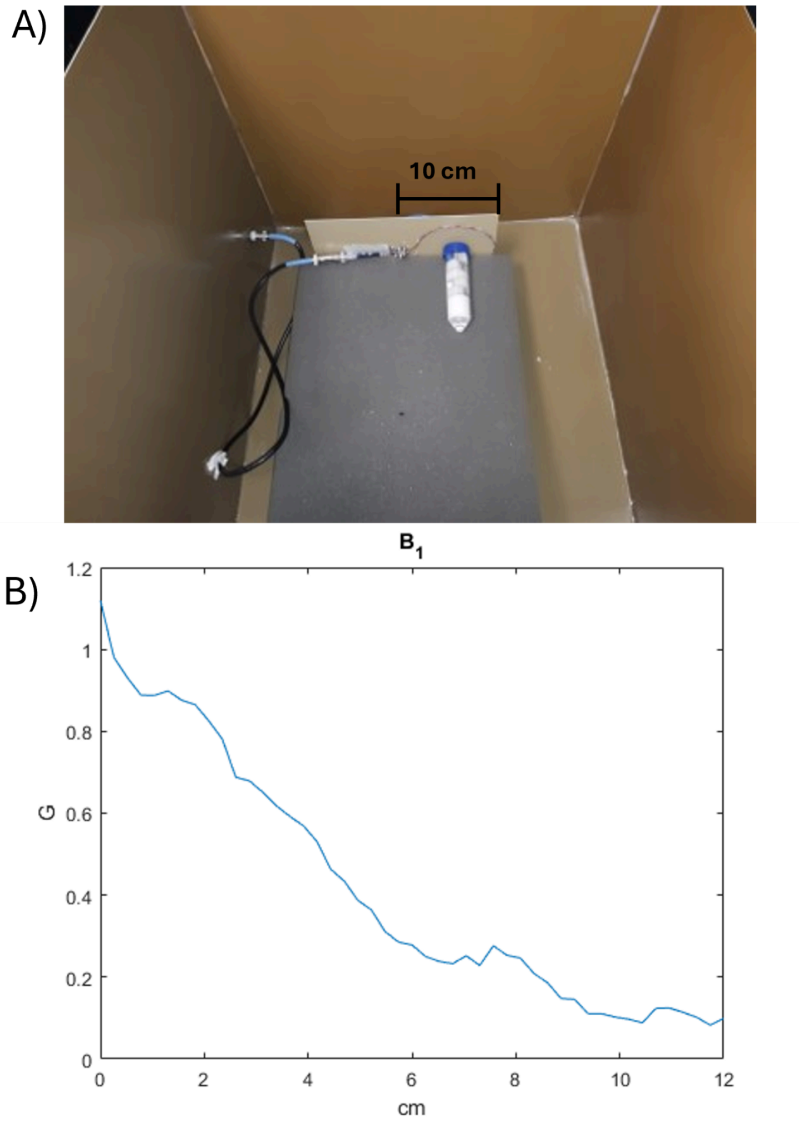


Figure 4.7: A) The 10 cm single loop coil positioned in the FR4 shielded box for imaging a 50 mm mineral oil tube phantom. B) $B_1$ map of the 10 cm single loop coil.

Figure 4.8 shows the constructed 12 cm gradient solenoid, along with its tune and match circuit schematic and its experimentally measured $B_1$ field (0.35-0.95 Gauss). The field is most linear at the 3-12 cm range and phantoms were positioned within this range for experiments outlined in Chapter 5.

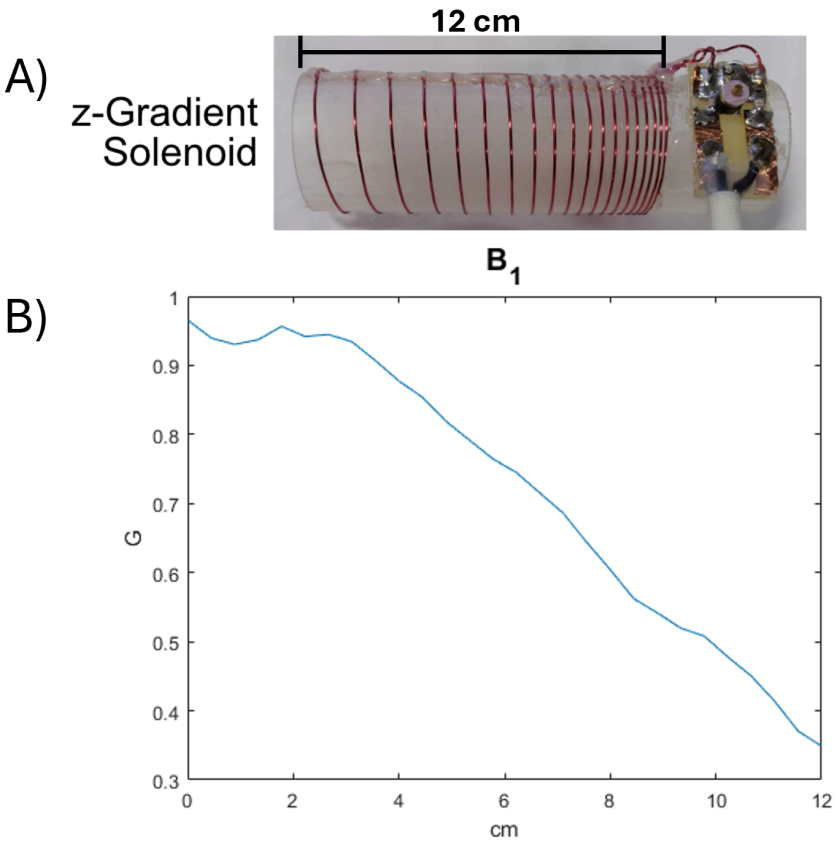


Figure 4.8: A) The 19-winding variable pitch 4 cm diameter solenoid 12 cm in length with a linear $B_1$ field. B) $B_1$ map of the 12 cm solenoid.

### 4.3.4 Optimized nested RF coil

The optimization produced a coil 16cm in length, not placing windings at the final 4 cm (8 positions). The coil was capable of generating a $B_1$ field ranging from 1 to 3 G with 1.4 A of current. When measuring the $B_1$ of the coil, higher power levels caused distortions in the pulses which reduced the available $B_1$ range, however the high linearity of the field was maintained (Figure 4.9).

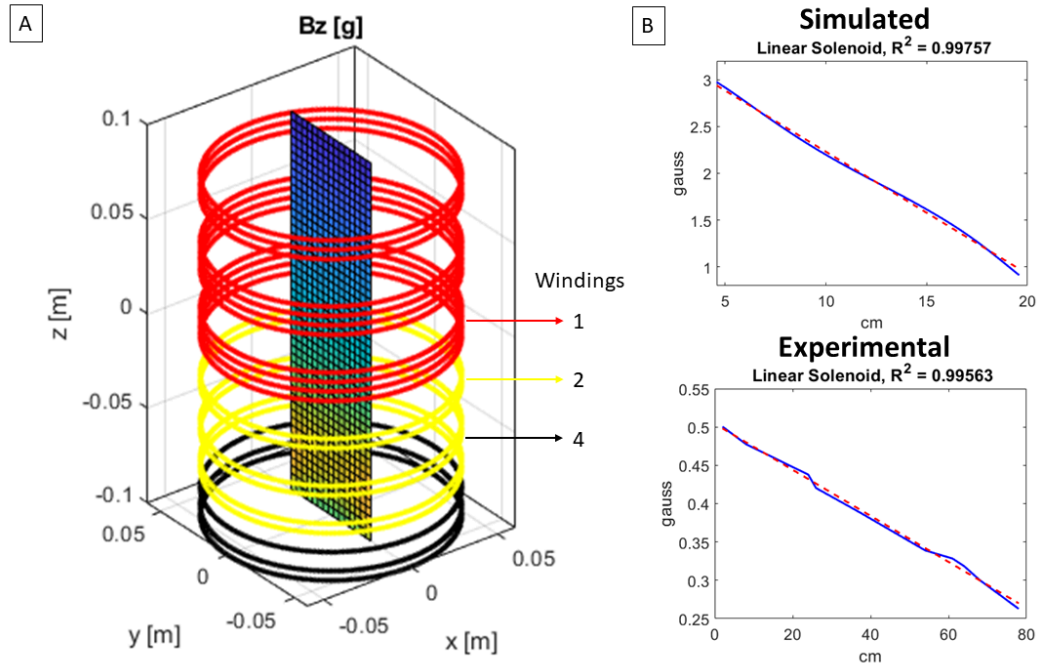


Figure 4.9: A) Windings and $B_1$ field of the optimized linear solenoid. B) Simulated and experimentally measured linear $B_1$ fields from the coil.

The optimized winding pattern produced a $B_1^+$ field with some perturbations caused by multiple windings being present in a single groove, which caused saddle points towards the edge of the 6 cm radius of the coil. To minimize the perturbations, the windings were distributed evenly around their fixed position to surrounding grooves, where possible (Figure 4.10). The sum of squares of residuals (RSS) for the $B_1$ field produced versus the target $B_1$ field over the 16 cm FOV was reduced by 11% by distributing the windings.

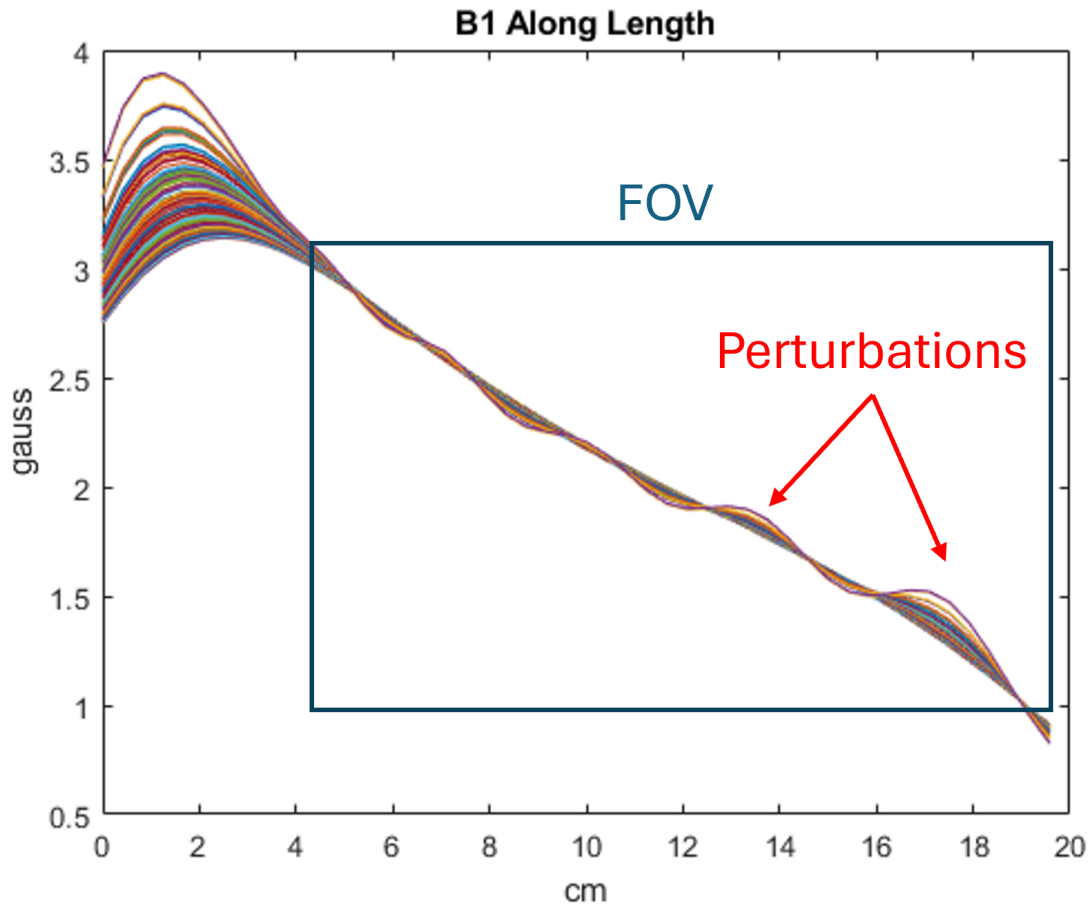


Figure 4.10: 1D $B_1^+$ fields plotted along the x-axis where each line is one 3.3 mm x 3.3 mm pixel of the 3 cm central radius of the optimized coil. The blue box denotes the region of the field that was optimized for and the red arrows point out the minimized perturbations in the field by spreading out the windings.

The saddle and gradient solenoid coils were geometrically decoupled by 30 dB, as seen in the S22 measurement (Figure 4.11B). Further 40 dB decoupling was achieved with the reed relay TR switch. The S11 and S22 measurements show the gradient solenoid and saddle coil, respectively, are tuned to the correct frequency with a good match. This then enabled use of the saddle coil, not only for higher receive signal levels, but also for uniform excitation as well in the qRF-BS SENF sequence.

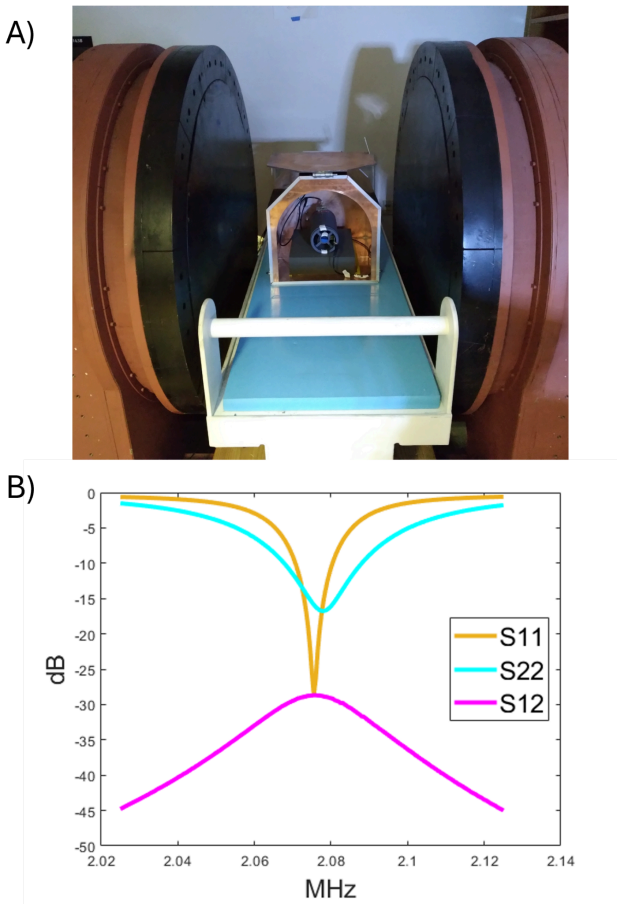


Figure 4.11: A) The nested coil setup inside a shielded box placed in the 47.5 mT magnet. B) S-Parameter plot showing the S11 and S22 of the linear solenoid and saddle coil respectively. S12 plot showing the 30 dB decoupling between the coils.

Figure 4.12 shows the components used for orienting and positioning the saddle coil and phantoms within the optimized gradient solenoid. These components enable positioning of the saddle coil for proper geometric decoupling, as well as positioning the $B_{1y}$ field within the optimized linear region of the gradient solenoid for use as a transmit or receive coil. The phantom holder also allows for positioning of phantoms, by sliding it within the coil holder with 2.5 cm ball phantoms at different compartments within the holder.

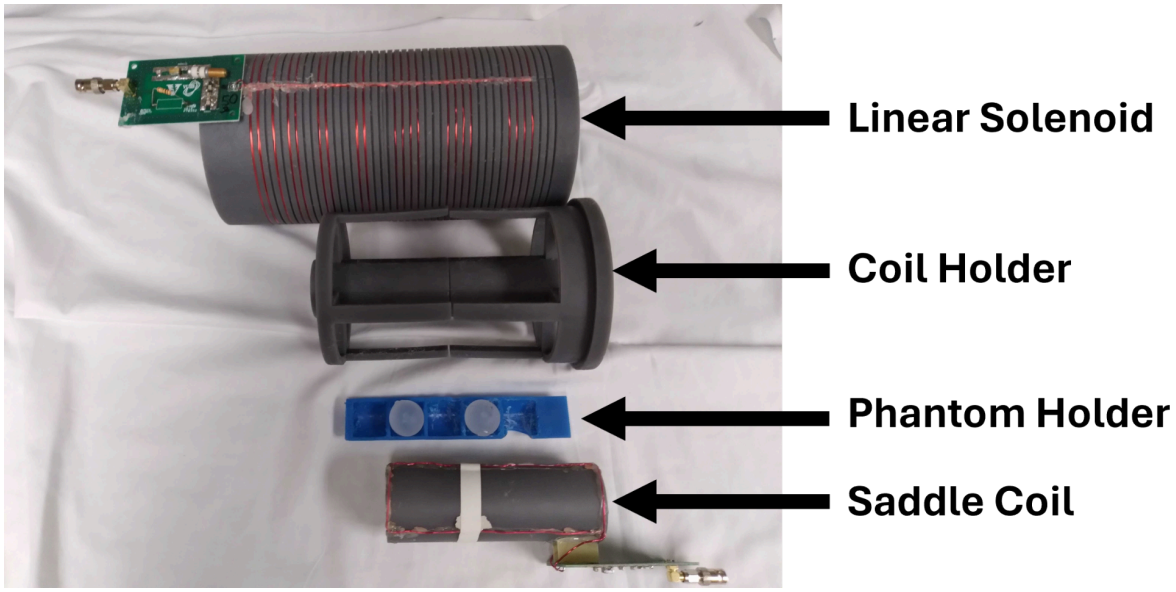


Figure 4.12: Nested coil components including the linear solenoid, coil holder, phantom holder and saddle coil.

### 4.4 Discussion and Conclusion

The proof of principle simulation performed in Chapter 3 applied SENF to encode and reconstruct 64 by 64 $T_1$ and $T_2$ parametric maps of a brain slice phantom with only two voxels (0.05%) misclassified outside of the brain slice. These promising results prompted efforts to experimentally validate SENF on a low-field MRI system, specifically our 47.5 mT SIGWA magnet. Furthermore, three different SENF sequences were developed that used different $B_1$-dependent pulse effects for spatial and quantitative encoding, capable of 1-3 mm spatial resolution at 18-37 SNR: $B_1^+$-selective SENF, hard pulse SENF and qRF-BS SENF. To experimentally implement these SENF sequences and experimental protocols, several hardware components had to be developed as discussed in this chapter. These include FR4 and copper-clad acrylic EMI shielded boxes that provided the EMI reduction necessary for adequate SNR (18-37) allowing for 1D SENF experiments to be performed. The ease of access to the experimental

setup with the copper-clad acrylic EMI shield expedited the experimental protocol used in 1D SENF experiments, where the phantoms were repositioned at 5 mm increments throughout an 8 cm imaging volume, collecting data at each point (Chapter 5). The copper-clad acrylic EMI shield had increased noise levels compared to the FR4 shield (2.5x higher RMS), which was overcome with additional averages, offering 20 SNR for SENF acquisitions with 4 averages. The time of day-dependent noise showed higher noise variations of up to 8.8x higher RMS, which was a larger factor in noise levels, and was overcome by scheduling experiments during times of low noise, or further increasing acquisition averages to achieve required SNR levels of 18-37 SNR. The coils including the 10 cm loop coil and 12 cm gradient solenoid allowed for testing of $B_1^+$-selective pulse testing and implementation as well as a 1D spatial encoding experiment using $B_1^+$-selective pulses and a dictionary based reconstruction, which is discussed further in Chapter 5. The optimized gradient solenoid with a nested saddle receive coil was used for hard pulse SENF experiments, where the high linearity of the field ($R^2$=0.99563) allowed for uniform excitation patterns to be produced with hard pulses enabling uniform spatial encoding over the imaging volume. The uniform encoding allowed for reconstructions of phantoms throughout the imaging volume without variable resolution. The optimized gradient solenoid was also used for qRF-BS SENF experiments, where a square root $B_1$ field would be ideal to allow for uniform encoding, but the high linearity of the $B_1$ field made the variations in spatial resolution over the field of view and easily quantifiable and could be accounted for in reconstructions. Both of these uses of the optimized gradient solenoid are discussed further in Chapter 5.

Overall, the hardware developed in this chapter was used to perform 1D SENF experiments on a 47.5 mT low-field scanner, resulting in $B_0$ gradient-free dictionary reconstructions of using $B_1^+$-selective pulses and 1D SENF projections for hard pulse SENF and

qRF-BS SENF sequences, which will be discussed in Chapter 5. The materials used are easily available for purchase through McMaster and Digikey, among other vendors. Further improvements could have been made by developing a square root solenoid to enable uniform encoding for qRF-BS SENF or use of RF amplifiers optimized for flat amplitude pulses that limit RF waveform distortions to enable a more robust implementation of $B_1^+$-selective excitation pulses. These improvements would be developed for future work on improving the experimental implementation of SENF.

# CHAPTER 5: IMPLEMENTATION OF SENF ON A 47.5 MT LOW-FIELD SCANNER

## 5.1 Introduction

Introduced in Chapter 3, Selective Encoding through Nutation and Fingerprinting (SENF) is a quantitative RF encoding technique that simultaneously encodes spatial and quantitative information. SENF uses inhomogeneous $B_1$ fields with RF pulses that create $B_1$-dependent effects within these fields to produce incoherent encoding patterns over an imaging volume. These encoding patterns are implemented into each TR of an MRF- type sequence to produce signals that are unique for different spatial locations and quantitative parameters. A dictionary-based reconstruction is then done to simultaneously extract spatial and quantitative information, producing multiple parametric maps.

In Chapter 3, a proof-of-principle simulation was performed to show the viability of SENF, where $B_1^+$-selective SENF was used to encode a brain slice phantom using an 8-coil pTx array. $T_1$ and $T_2$ 64 by 64 voxel parametric maps of a brain slice phantom were reconstructed, and only 2 voxels outside of the brain were misclassified. Additionally, comparison simulations were performed for three different SENF sequences: $B_1^+$-selective SENF, hard pulse SENF, and qRF-BS SENF. The three SENF sequences were compared between each other and conventional $T_1$ IR and $T_2$ spin echo sequences. The results of the feasibility simulation showed that SENF can reconstruct 2D parametric maps with minimal error (0.05%), and the comparison simulation revealed the SENF sequences had comparable resolution (1-3 mm) to 7 mT/m gradients (1 mm) used on the 47.5 mT scanner, and comparable minimum SNR (18-37 SNR) to what was achieved for SENF sequences (24 SNR), further improved with additional averages. These results support moving forward with experimental implementation.

To experimentally validate SENF, it must be implemented on a real MRI system, preferably at low-field due to its high RF duty cycle, much like other RF gradient methods (Hoult, 1979; Sharp, 2010; Wright, 2009; Katscher et al., 2010; Torres et al., 2022). For this, a 47.5 mT SIGWA bipolar low-field magnet was used. This magnet was described in Section 4.2.1. Several hardware components (EMI shielding, TR switches, and RF coils) had to be developed for the experiments as outlined in Chapter 4. The 12 cm gradient solenoid was used to verify the excitation profiles of the $B_1^+$-selective pulses and for a sweeping-band 1D spatial encoding experiment along with the copper-clad acrylic EMI shield and the reed relay TR switch. The 10 cm loop coil was used to test the spatial encoding capabilities of the $B_1^+$-selective pulses along with the FR4 shielded box and a passive crossed-diode TR switch. The optimized gradient solenoid was used to test hard pulse and qRF-BS SENF sequences along with the copper-clad acrylic EMI shield and the reed relay TR switch. These experiments are reported in this chapter.

This chapter reports the experimental development and implementation of three SENF sequences: $B_1^+$-selective SENF, hard pulse SENF, and qRF-BS SENF on a 47.5 mT magnet. The challenges and the successful experimental implementations of each SENF sequence presented and the limitations of each sequence are discussed. The different SENF sequences were developed to overcome a specific limitation of the previous sequence, apart from the $B_1^+$-selective SENF sequence which was the first conceptualization of SENF. These limitations were a result of the encoding mechanisms of the SENF sequence accompanied by the non-ideal conditions of the scanner and hardware. The limitation of the previous sequence as well as how the next sequence overcame that limitation are discussed. The sequences are presented in the order that they were developed, which is: $B_1^+$-selective SENF, hard pulse SENF, and qRF-BS

SENF. An overview of each SENF sequence is provided, including the components that comprise and differentiate the different sequences such as the inhomogeneous $B_1$ field used, the $B_1$ dependent pulse effect, the sequence design and the reconstruction technique used. Since this was the first experimental implementation of SENF, a simplified 1D embodiment with two materials was implemented to demonstrate the spatial and quantitative encoding of each SENF sequence. The experimental results presented showcase the best spatial and quantitative encoding achieved by the first experimental implementation of each SENF sequence. The results were not directly comparable between each sequence, since different challenges were encountered in each of their implementations which led to different levels of success. A simulated direct quantitative comparison of the three SENF sequences was reported in Chapter 3, which assessed the minimum SNR and resolution of each sequence. The experimental results presented here were quantitative in nature, but the quality of the best result for each SENF sequence varies.

## 5.2 Methods

### 5.2.1 $B_1^+$-Selective SENF Sequence: RF Pulse Testing

The $B_1^+$-selective SENF sequence was the first conceptualization of SENF, combining the ideas of MRF (Ma et al., 2013) and $B_1^+$-selective excitation pulses (Grissom et al., 2014) to perform spatial and quantitative RF encoding discussed in Chapter 3. Each SENF sequence consists of four components: an inhomogeneous $B_1$ field, pulses that create $B_1$ dependent effects, an MRF-type sequence and a dictionary reconstruction that simultaneously extracts quantitative and spatial information. The pulse dependent effect used was $B_1^+$-selective excitation pulses, which produce a constant amplitude excitation over a designed $B_1$ range with constant phase. Experiments were performed with $B_1^+$-selective excitation pulses to verify the excitation profiles,

perform gradient-free imaging, and a 1D spatial encoding experiment with a dictionary based reconstruction. The distortions of the $B_1^+$-selective pulse excitation profiles due to these RF waveform distortions will be discussed to show the limitations that prevented a two material $B_1^+$-selective SENF sequence experiment, and necessitated the development of the hard pulse SENF sequence discussed in the next section until improved transmit fidelity can be achieved.

#### 5.2.1.1 Verification of $B_1^+$-Selective Pulse Excitation Profile

With the first conceptualization of $B_1^+$-selective SENF in Chapter 3 and the coils and hardware developed in Chapter 4, the first step for experimental implementation was to evaluate whether the excitation patterns of a $B_1^+$-selective pulse could be accurately produced by the 47.5 mT scanner. To do this, a 2D GRE sequence was implemented, which used either a hard pulse excitation or a $B_1^+$-selective excitation with the same echo time (TE) of 30 ms and repetition time (TR) of 400 ms and 1 average. The hard pulse used for the control excitation was 50 us long to produce a maximum flip angle of 90° at the highest $B_1$. A 2-band Hadamard $B_1^+$-selective excitation pulse was designed of length 3.76 ms, a passband center of 0.5 Gauss, a passband width of 1 Gauss, and a flip angle of 90°. The 2 by 2 Hadamard matrix contains +1/+1 and +1/-1 entries in its first and second rows, which define the polarity of the subbands produced by the two $B_1^+$-selective pulses designed from it that were used. The sequence used conventional $B_0$ encoding to frequency encode the x-axis, which was along the $B_1$ gradient, while the z-axis was phase-encoded. The sequence projected signal across the y-axis. The RF coil used was the 12 cm gradient solenoid with a peak $B_1$ of 1.3 Gauss. The copper-clad acrylic EMI shield was used along with a reed relay TR switch. An 11.5 cm-long 50 ml tube filled with mineral oil was used as a phantom. A conventional Fourier transform reconstruction produced proton density images

of the excitation produced by the hard pulse or $B_1^+$-selective pulse. A complex division of the hard pulse excitation data was performed with the $B_1^+$-selective excitation data to remove any unwanted phase distortions and the receive sensitivity. The images were directly compared to the expected profiles of the $B_1^+$-selective pulses produced by a Bloch simulation to assess their fidelity.

#### 5.2.1.2 Gradient-Free Imaging Using Hadamard $B_1^+$-Selective Excitation Pulses

After verifying the Hadamard $B_1^+$-selective excitation profiles, the next step was to use the pulses for spatial encoding. The 10 cm-loop coil with the ~1/x $B_1$ field was used at an RF power level that produced a peak $B_1$ of 1 Gauss. The coil was used for both transmit and receive. The FR4 EMI shield and a passive cross-diode TR switch was used. For the phantom, an 11.5 cm-long 50 ml tube was filled with mineral oil and offset-crescent-shaped plastic fillers were placed inside to produce structure along the length of the tube. The tube was then oriented perpendicular to the loop coil along the x-axis. A 3D GRE sequence with TE of 31.46 ms, a TR of 100 ms and a 10 $\mu$s hard pulse excitation was used to acquire a fully $B_0$ encoded image of the phantom. A set of eight 7.52 ms-long 8-band Hadamard $B_1^+$-selective pulses with a passband center of 0.5 Gauss and a passband width of 1 Gauss were designed. Each of these eight pulses were used as the excitation pulse in the 3D GRE sequence and eight data sets were acquired. The second encoding pulse had subbands that alternate in polarity between each subband, allowing for easy spatial localization of the subbands within the excitation pattern. Using this pulse for excitation in a 1D GRE sequence, a $B_0$ frequency encoded 1D projection was taken of the excitation pattern produced. Each of these subbands constituted a single slice in the final image, as they were used

to encode the slice dimension along the x-axis that was $B_0$ frequency encoded in the 1D projection.

To produce the control image, the complex image data from the 3D GRE sequence with the hard pulse excitation was summed across the slice dimension (x-axis) in eight different bins, each corresponding to a single subband of the 8-band Hadamard $B_1^+$-selective acquisition. The width of each slice was determined by the width of each subband produced by the Hadamard pulse as measured in the 1D projection. There were 8 slices, each covering one of the subbands of the 8-subband Hadamard pulses used, and each subband had increasing widths as local $B_1$ gradient decreased along the ~1/x $B_1$ field of the 10 cm loop coil. This produced eight 2D images, one for each slice encoded by the 8-band Hadamard $B_1^+$-selective pulse. The 2D complex data from the k=0 point in the frequency encoded dimension was taken from the eight data sets from the 3D GRE sequence that used each of the Hadamard $B_1^+$-selective pulses as excitation. These data were concatenated and multiplied by the inverse of the Hadamard matrix (Eq. 5.1), then a 3D Fourier transform was done to reconstruct each slice.

$$D_S = H^{-1} D_H, \tag{5.1}$$

where $D_S$ is the 3D k-space data ready to be Fourier transformed for an image, $H$ is the 8 by 8 Hadamard matrix, and $D_H$ is a 3D matrix of the concatenated 2D data taken from the k=0 point in the frequency encoded dimension of the 3D GRE data.

#### 5.2.1.3 Sweeping-band 1D Spatial Encoding

The first two experiments showed the fidelity of the excitation profiles of a 2-band Hadamard $B_1^+$-selective pulse and the use of an 8-band Hadamard $B_1^+$-selective pulse for encoding the slice dimension of an image with in-plane $B_0$ phase encoding. The next step towards a full

$B_1^+$-selective SENF implementation was to use excitation patterns from a set of Hadamard $B_1^+$-selective pulses to perform 1D spatial encoding with a dictionary based reconstruction that relied on no $B_0$ encoding, using a single material (mineral oil).

For this experiment, the 12 cm gradient solenoid was used, since the linear $B_1$ field simplified the design of the Hadamard $B_1^+$-selective pulses for uniform encoded spatial resolution. The copper-clad acrylic EMI shield was used with a reed relay TR switch. A 2-band Hadamard $B_1^+$-selective pulse was designed with a passband center of 0.5 Gauss, a passband width of 2 Gauss, and a duration of 3.76 ms. The passband center of the two encoding pulses were varied across the 0 to 1 Gauss range in 32 steps to produce a set of 64 Hadamard $B_1^+$-selective pulses. These 64 pulses were used as excitation pulses in an MRF-type sequence with 64 TRs 10 ms-long and a constant flip angle of 90°. These pulses had a signal null 7.5 mm in width at the passband center that was swept across the object by using the 64 pulses. This acted as the basis for spatial encoding, along with the opposite phase of the excitation bands on either side of the null for the second encode. For the phantom, a 2.5 cm mineral oil ball was used. The mineral oil ball was placed at two different positions (6 cm, 0.5 Gauss and 9 cm, 0.75 Gauss) within the 12 cm coil, and data were collected with the MRF-type sequence for each position. For the reconstruction, a Bloch simulation of the sequence using the 64 excitation patterns was performed for mineral oil relaxation parameters at 1 mm spatial resolution over a 12 cm FOV. The simulated signals were collected into a dictionary for all spatial locations. A regularized pseudoinverse of the dictionary was multiplied into the collected signal for the mineral oil ball data for each phantom position to yield coefficients for all simulated spatial locations. The coefficients were then plotted along the x-axis as a 1D projection reconstruction of the two different mineral oil ball data sets.

#### 5.2.1.4 RF Fidelity Limitations

$B_1^+$-selective pulses require precise envelope areas to produce a desired excitation profile, which was not possible on the 47.5 mT scanner. This section will discuss the sources of RF waveform distortions present on the 47.5 mT system, and the correction methods used to attempt to reduce these distortions. Simulations of the distortions were performed to show their effect on the excitation profiles of the $B_1^+$-selective pulses.

##### 5.2.1.4.1 Transmit chain distortions

The transmit chain on the 47.5 mT scanner was described in Section 4.2.1. It started with the Tecmag Redstone Spectrometer, which synthesized a 1.4 $V_{pp}$ max waveform at the center frequency with the phase and amplitude defined in the TNMR software that operated the spectrometer. The spectrometer output was then input into a 2kW, 500W, or 250W Tomco RF power amplifier. The RF output from the amplifier was then connected to a TR switch to allow for operating a single coil in both transmit and receive mode or to provide additional isolation between two coils operating in either transmit or receive mode. The output from the TR switch was then connected to the transmit RF coil.

The RF amplifiers caused some distortion of the RF waveform due to amplifier droop, where the amplifier cannot maintain full RF power over the duration of a long pulse. To show an example of this, a simulation of a 20% droop over a 1.38 ms-long pulse with a passband center of 0.8 Gauss and a passband width of 1.6 Gauss and a flip angle of 90° was performed. A Bloch simulation was performed over a 0 to 2 Gauss $B_1$ range in 512 steps, and the $|M_{xy}|$ was reported for each $B_1$.

Each RF coil had a center frequency and a bandwidth over which there was a < 3dB difference in power transmission. The bandwidth of the coils were increased by adding spoiling resistors in series with the coil to minimize frequency dependent power attenuation; however, these effects were still present and caused distortions to the RF pulse. To show this, a simulation was performed using a 1.38 ms-long 2-band Hadamard $B_1^+$-selective pulse with a passband center of 0.6 Gauss and passband width of 1.2 Gauss distorted by the frequency dependent amplitude response of the 12 cm gradient solenoid, which was computed based on the coil's frequency dependent reflection coefficient (S11). A Bloch simulation was performed over a 0 to 2 Gauss $B_1$ range in 512 steps, and the $|M_{xy}|$ was reported for each $B_1$.

**5.2.1.4.2 RF Waveform Corrections: Envelope Modulation and Pre-emphasis**

The distortions in the $B_1^+$-selective RF waveforms were larger with larger phase transitions between time points in the pulse. These were largest when the envelope had sign changes from + to -, indicating a 180° change in phase. To minimize this distortion the pulse envelope was modulated with hyperbolic tangent (tanh) functions. Each section of the envelope of a single sign used two tanh functions to produce a single lobe that approached 0 at the beginning and end of the section, and max amplitude in the center. This smoothed the envelope of the pulse and caused the envelope to approach zero when it changed signs, where the largest phase changes occur. Using a procedure known as variable-rate selective excitation (VERSE) (Conolly et al., 1969), implemented in MATLAB code developed by John Pauley in 1992 (verse.m), the frequency waveform was then mapped onto the modulated envelope waveform to maintain the excitation profile.

To further account for the RF waveform distortions, the RF waveforms were pre-emphasized. A wideband coil probe was coupled to the RF transmit coil and connected to a receive channel on the Tecmag spectrometer with attenuation to acquire loopback measurements of the $B_1^+$-selective pulses. Loopback measurements were then taken of the $B_1^+$-selective pulses to be corrected. A complex division of the ideal RF waveform and the loopback measurement was taken to produce a pre-emphasized RF waveform with amplitude and frequency distortions that opposed the measured distortions. These pre-emphasized waveforms corrected for any RF waveform distortions that were static and not time-dependent.

### 5.2.2 Hard pulse SENF Sequence

Hard pulse SENF uses the four core SENF components: an inhomogeneous $B_1$ field, pulses that create $B_1$ dependent effects, an MRF-type sequence and a dictionary reconstruction that simultaneously extracts quantitative and spatial information. Hard pulse excitations were used for this sequence's $B_1$ dependent effect. Three experiments are reported where the hard pulse SENF sequence was used to reconstruct two materials in 1D: 1) in four 2.5 cm voxels with an experimentally measured dictionary, 2) using a simulated dictionary, and 3) with 1 mm resolution over an 80 mm FOV with a simulated dictionary. Finally, challenges with optimization of the encoding power of the sequence were discussed.

#### 5.2.2.2 Two Material 1D Hard Pulse SENF Experiments

For the hard pulse SENF experiments, the copper-clad acrylic shielded box was centered inside of the 47.5 mT magnet and the optimized gradient solenoid was placed inside with the nested saddle receive coil. The reed relay TR switch was used. The gradient solenoid was used to

transmit the high flip angle hard pulses to produce excitation patterns over the 3 by 3 cm cross section 10 cm-long imaging FOV, while the nested saddle receive coil was used to acquire data. The sequence structure was an adiabatic inversion pulse followed by a repeated block of an excitation pulse followed by an acquisition and a dwell time to produce the desired TR length. The flip angle and TR length at each TR followed pre-defined schedules and the values were varied at each TR.

For the first experiment, a flip angle schedule was designed with a peak flip angle of 18.4 radians produced at the highest $B_1$ producing 7.8 signal peaks and nulls across the 10 cm imaging volume, which corresponded to an encoded spatial resolution of 6.41 mm, measured as the imaging FOV divided by the number of signal peaks and nulls of the highest RF power, as these will differentiate the signal between adjacent spins with the smallest spatial separation. It is analogous to the highest k-space location representing the most phase twists across a slice. The flip angle was varied in lobes of 30 TRs (455 TRs total) and with increasing downtime between each lobe to allow for signal evolution, followed by four back-to-back lobes (Figure 5.1). Four 2.5 cm ball phantoms were placed into the phantom holder at fixed positions and contained either mineral oil ($T_1$=104 ms, $T_2$=96 ms) or gadolinium doped water ($T_1$=330 ms, $T_2$=220 ms). The goal of the experiment was to reconstruct four 2.5 cm voxels, each containing a single ball phantom, making the 6.41 mm resolution sufficient for this purpose. To further differentiate the signals the TR was varied for each flip angle lobe (average TR = 25 ms) so that different amounts of free evolution of the spins could occur between excitations (Figure 5.1). The overall schedule structure was decided somewhat arbitrarily other than the considerations mentioned above as a starting point for the sequence design.

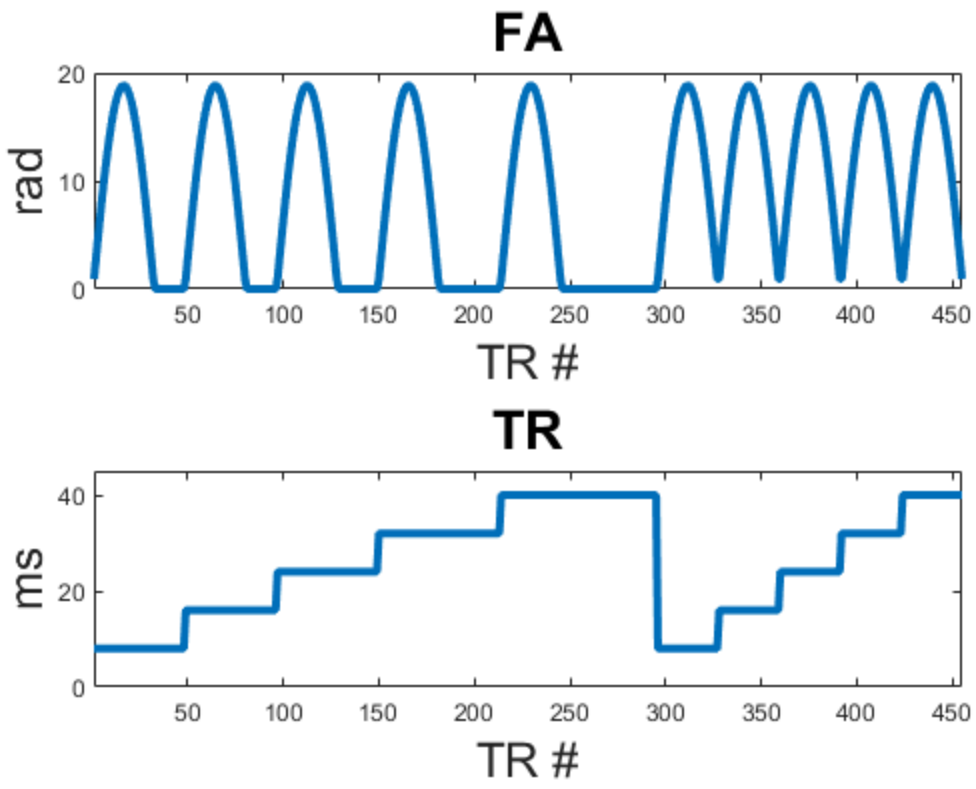


Figure 5.1: Flip angle with a peak flip angle of 18.83 rad and TR schedule with an average TR of 25 ms, both 455 TRs-long. The flip angle and TR schedules were used for the 4-voxel hard pulse SENF validation experiment.

The four ball phantoms were set into three configurations: 1) two doped water phantoms; 2) two mineral oil phantoms; and 3) alternating mineral oil and doped water phantoms. For this first implementation, the dictionary was measured experimentally by placing a mineral oil or doped water phantom in each of the four possible spatial positions and collecting a data set for each. These data sets were collected into one column of the dictionary each, exactly like a Bloch simulated signal would be. This experimentally accounted for any parasitic $B_1$ or $B_0$ inhomogeneities in the dictionary construction. Data was then collected from the three different ball phantom configurations and reconstructed with a regularized pseudoinverse of the

experimentally measured dictionary and the data. The maximum coefficient between the two materials was chosen for each voxel and coefficients below a certain threshold were rejected and reconstructed as air, similar to the proof of principle simulation discussed in Chapter 3.

The second experiment improved upon the first by accurately simulating the signal dictionary, rather than experimentally measuring it. This was done by measuring the $B_1$ map of the coil, as well as the $B_0$ distribution for the ball phantoms in each position. A spin echo sequence was used to measure the $B_0$ distribution. An FFT of the data was taken to obtain the center frequency and the full width at half max (FWHM) of the frequency distribution. The $B_1$ was measured by sliding a mineral oil ball through the FOV at 5 mm increments and modulating the excitation pulse width until signal was maximized corresponding to a 90° excitation at each location. The $B_1$ values were calculated from this and a linear fit was performed to determine the $B_1$ values at 1 mm increments throughout the 10 cm FOV. A Bloch simulation was performed at 1 mm spatial resolution for both mineral oil and doped water over the 10 cm FOV accounting for a single $B_1$ value and a $B_0$ distribution for each 1 mm point. To synthesize each dictionary entry, corresponding to one material and one of the four voxels, the simulated signals for each 1 mm point within the 2.5 cm voxel were summed together using weights of the expected spin distribution of the phantom. These simulated signals were then collected into a dictionary. A regularized pseudoinverse of the simulated dictionary was performed against the measured data and the three phantom configurations were reconstructed. Again, the maximum coefficient between the two materials was chosen for each voxel and coefficients below a certain threshold were rejected and reconstructed as air.

For the third experiment, the data were reconstructed at 1 mm resolution reconstruction rather than the four 2.5 cm voxels. To do this full $B_0$ and $B_1$ maps were measured across the 8 cm

long imaging volume. This was done by placing a 2.5 cm mineral oil ball phantom at the highest $B_1$ position and sliding it at 5 mm increments through the 8 cm FOV. At each position and $B_1$ calibration sequence and a spin echo sequence were measured to determine the $B_1$ and $B_0$ value at each position. A first order polynomial fit was used to fit the measured $B_1$ values at 1 mm spatial resolution for dictionary Bloch simulations. A second order polynomial fit was used to fit the center frequency and FWHM for the measured $B_0$ values at 1 mm spatial resolution for dictionary Bloch simulations. The chemical shift of the doped water (7.243 Hz) relative to the mineral oil was measured as well and accounted for in dictionary Bloch simulations. A dictionary was simulated for mineral oil and doped water at 1 mm spatial resolution using the corresponding $B_0$ and $B_1$ value for each position resulting in 81 columns for each material, instead of the 4 columns used for each material in the previous experiment. The TR length was shortened as much as was possible (8 ms) with the reed relay switching times (500 us) and the minimum hard pulse length (690 us) needed to produce the required flip angles at peak power. The flip angle schedule was also downsampled by four to reduce the number of TRs to 114 (Figure 5.2). These sequence modifications were done to limit the effects of accrued phase due to off-resonance as discussed in the previous subsection. For the collected data, a mineral oil and doped water ball were placed adjacent to each other with the mineral oil ball towards the higher $B_1$ field. The mineral oil ball was centered at the edge of the 8 cm imaging volume and the two adjacent phantoms were slid at 5 mm increments through the entire imaging volume, collecting data at each position. Each of these data sets were reconstructed using a regularized pseudoinverse of the data set and the simulated dictionary with 1 mm spatial resolution. Rather than rejecting any of the coefficients as air, the coefficients were simply plotted for each material over the 8 cm imaging volume.

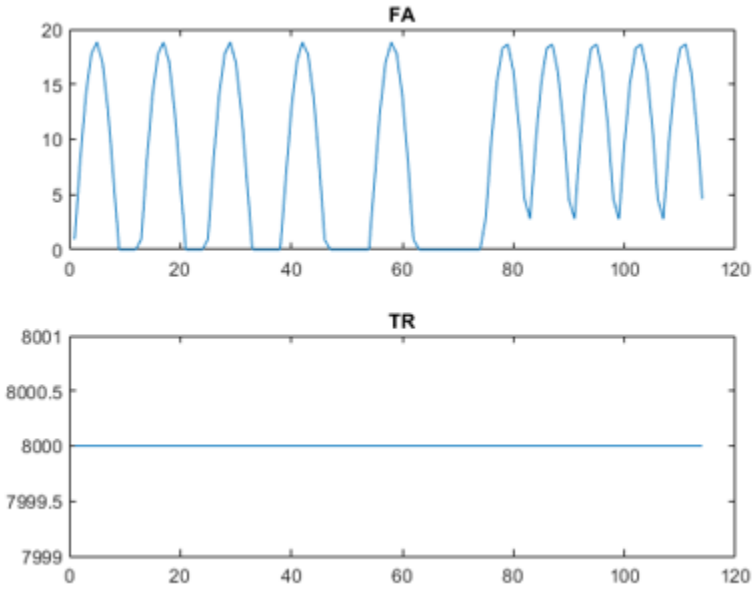


Figure 5.2: Flip (rad) angle with a peak flip angle of 18.83 rad and TR (ms) schedule with a constant TR of 8 ms, both 114 TRs-long. The flip angle and TR schedules were used for the 1 mm spatial resolution two material hard pulse SENF experiment.

#### 5.2.2.3 Encoding Optimization Limitations

As discussed previously, the excitation pattern for a hard pulse transmitted through a linear gradient solenoid will vary depending on the RF power of the pulse, and was the basis of spatial encoding with a hard pulse SENF sequence. However, the modulation of the flip angle and TR schedules was fundamental for encoding quantitative information as seen in MRF (Ma et al., 2013), specifically $T_1$ and $T_2$ relaxation values. Therefore, the spatial and quantitative encoding were not independent. This presents challenges when optimizing the encoding power of a hard pulse SENF sequence.

For sequence optimization the flip angle and TR schedules can be constructed using sine functions with variables for the amplitude and frequency of the schedules. A full dictionary of the sequence was then simulated at 1 mm spatial resolution over the 8 cm imaging volume for mineral oil and doped water. The correlation matrix was then taken from the dictionary and the off-diagonal entries were summed to produce an error metric. This error metric was then minimized using a Nelder-Mead multidimensional unconstrained nonlinear minimization ( (fminsearch() in MATLAB) with the amplitude and frequency of the flip angle and TR schedules as the input variables. Due to the flip angle schedule modulating the excitation patterns fundamental for spatial encoding as well as the quantitative encoding, the solution space becomes complex and the optimization fails to produce sequences with improved encoding as measured by the sum of the off-diagonal entries of the dictionary correlation matrix.

### 5.2.3 Quadratic Phase Bloch-Siegert (qRF-BS) SENF Sequence

qRF-BS SENF was inspired by quadratic RF MRF (Boyacioglu et al., 2019), which has been used to encode off-resonance information alongside relaxation parameters. qRF-BS SENF uses the four core SENF components: an inhomogeneous $B_1$ field, pulses that create $B_1$ dependent effects, an MRF-type sequence and a dictionary reconstruction that simultaneously extracts quantitative and spatial information. The $B_1$ dependent pulse effect was created by off-resonance pulses via the Bloch-Siegert shift. Quadratic phase modulation of the hard pulse excitations encoded the off-resonance information into the time signal as outlined in Chapter 3. This section will cover the independent encoding optimization that was possible with qRF-BS SENF and the two 1D qRF-BS SENF sequence experiments performed. Finally, the effects of susceptibility on the experiments were discussed.

#### 5.2.3.1 Independent Encoding Optimization

With qRF-BS SENF, the spatial encoding was performed by the off-resonance pulses, taking advantage of the Bloch-Siegert shift, as well as the quadratic phase modulation of the hard pulse excitations to effectively encoding spatial information into the signal. This allows for parameter modulation of the flip angle schedule, as was done in MRF (Ma et al., 2013), to assist in quantitative encoding of relaxation parameters. Therefore, within the framework of the sequence optimization discussed in the hard pulse SENF section, the flip angle schedule can be optimized independently of the spatial encoding. This simplified solution space allowed for the nonlinear optimization to reach a solution outlining the flip angle schedule for the final qRF-BS SENF experiment discussed later in this section.

#### 5.2.3.2 One Material 1D SENF experiment

For the first 1D qRF-BS SENF experiment, the copper-clad acrylic EMI shield was centered in the 47.5 mT magnet, and the optimized gradient solenoid with the nested saddle receive coil was placed inside. The reed relay TR switch was used. The sequence consisted of a 15 ms-long adiabatic inversion pulse, followed by a repeated block (250 TRs) of hard pulse excitations with a flip angle of 50° and a phase of $5.6°*TR^2$ and a 9.004 ms-long 10kHz off-resonance pulse designed to produce an accrued phase range of $2\pi$ across the 8 cm imaging volume (Figure 5.3). The off-resonant pulses were transmitted through the optimized gradient solenoid and the hard pulses were transmitted through the saddle coil for uniform excitation. The saddle coil was also used as the receive coil. The phantom was a single 2.5 cm mineral oil ball phantom moved at 5 mm increments through the 8 cm FOV, similar to the hard pulse SENF experimental protocol, where data were collected at each position.

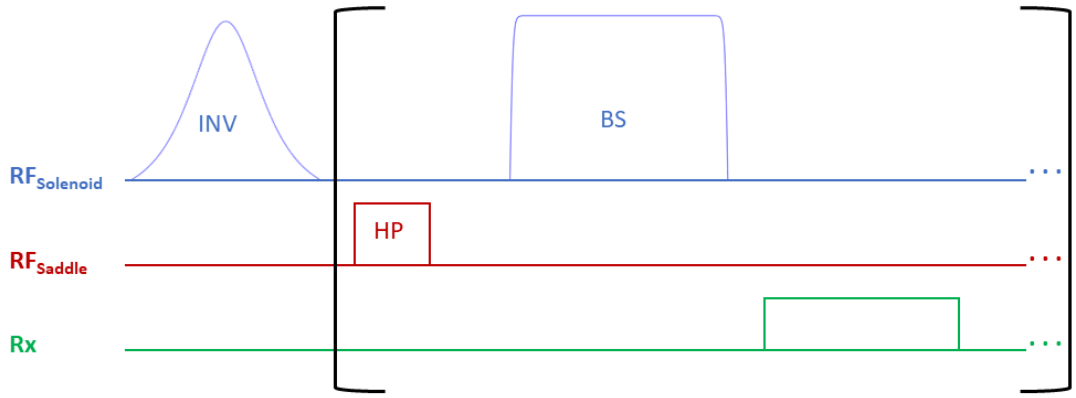


Figure 5.3: Sequence diagram for the BS quadratic phase SENF method including an inversion pulse followed by a repeated block of HP, BS pulse, and acquisition.

A dictionary was calculated with a 1 mm spatial resolution accounting for measured $B_1$ and $B_0$ spatial maps over the 8 cm FOV, similar to the hard pulse SENF sequence. Reconstructions were performed with a regularized pseudoinverse of the dictionary with the measured data, and the coefficients for each material were plotted over the 8 cm FOV without coefficient thresholding.

A simulated two material qRF-BS experiment was performed using adjacent 2.5 cm mineral oil and water ball phantoms slid through the 8 cm imaging volume in 5 mm increments. The measured data was synthesized by projecting the phantom's expected spin distribution through the simulated dictionary used to reconstruct the mineral oil ball phantom experiment described above. The synthesized data were reconstructed using a regularized pseudoinverse of the dictionary to obtain coefficients for each 1 mm spatial position for each material. These coefficients were plotted over the 8 cm imaging volume without coefficient thresholding.

For the second experiment, the sequence design was then improved to increase its quantitative encoding power. The first improvement was to add a second 250 TR repeated block

to the sequence using an off-resonance pulse with opposite polarity. This was done so that the accrued phase due to the BS shift changes signs between the two halves of the sequence, enabling disambiguation of spatial encoding phase with off-resonant phase, as discussed in Chapter 3. Next the flip angle schedule was optimized as outlined previously. This resulted in a flip angle schedule with an average flip angle of 6°, and a constant short 16 ms-long TR.

The dictionary calculation was also improved by accounting for the susceptibility effect between mineral oil and doped water, which will be discussed in the next section. With these improvements, the mineral oil only experiment was repeated to test the sequence, where the mineral oil phantom was slid through the 8 cm imaging volume at 5 mm increments and data were taken at each position. The measured data was reconstructed using a regularized pseudoinverse of the updated dictionary simulation that accounted for susceptibility, and the coefficients for mineral oil and water were calculated for each 1 mm spatial position. These coefficients were then plotted over the 8 cm imaging volume without coefficient thresholding.

#### 5.2.3.3 Susceptibility

One factor that had not been accounted for in the first SENF experiments was the susceptibility between the two materials. The $B_0$ distortion produced by the susceptibility between the mineral oil and doped water phantom was measured with two acquisitions of a 1D GRE sequence with a $T_E$=105 ms and $T_E$= 115 ms. The susceptibility was then calculated by subtracting the phase of these two projections, and inputting it into Eq 5.2.

$$f = \frac{\Delta\phi}{2\pi \cdot \Delta T_E} \tag{5.2}$$

where $\Delta\phi$ is the subtracted phase between the two projections and $\Delta T_E$ is the difference between the echo times of the two sequences. The measured susceptibility was added to the measured $B_0$

map and used in the Bloch simulation of the signal dictionary for the final qRF-BS SENF experiment.

## 5.3 Results

### 5.3.1 $B_1^+$-Selective SENF Sequence: RF Pulse Testing

The expected excitation profiles of the 3.76 ms-long Hadamard pulse with a passband center of 0.5 Gauss and a passband width of 1 Gauss and a flip angle of 90° using the 12 cm gradient solenoid is shown in Figure 5.4.

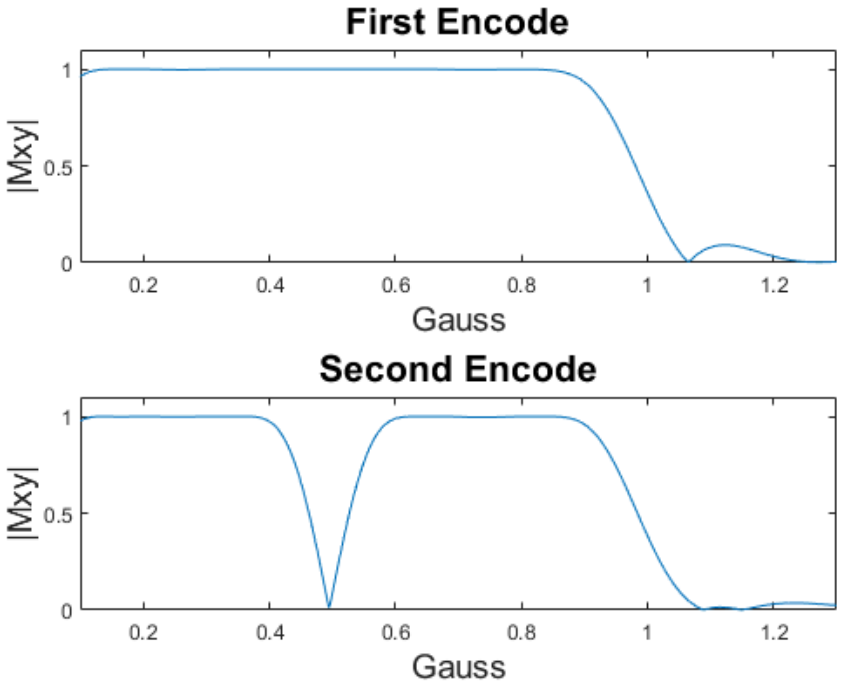


Figure 5.4: Excitation profiles of 3.76 ms-long Hadamard pulse with a passband center of 0.5 Gauss and a passband width of 1 Gauss and a flip angle of 90° plotted over the $B_1$ range of the 12 cm gradient solenoid. The excitation profile for the first and second encoding pulse are shown.

Figure 5.5 shows the excitation bands of both encodes of a 2-band Hadamard pulse, alongside a hard pulse excitation for a control. The hard pulse excitation linearly decreased with the $B_1$ strength as its peak flip angle at the highest $B_1$ point on the coil was less than or equal to 90°. For the Hadamard pulses, some excitation was still present outside of the desired bands, specifically on the right side of the image, and the amplitude of the excitations were not entirely uniform, as seen by the non-uniform color gradient across the image within the bands. These were most likely artifacts caused by the complex division of the data by the hard pulse control data for removal of unwanted phase and receive sensitivity. The expected band locations match the experimental measured excitation bands.

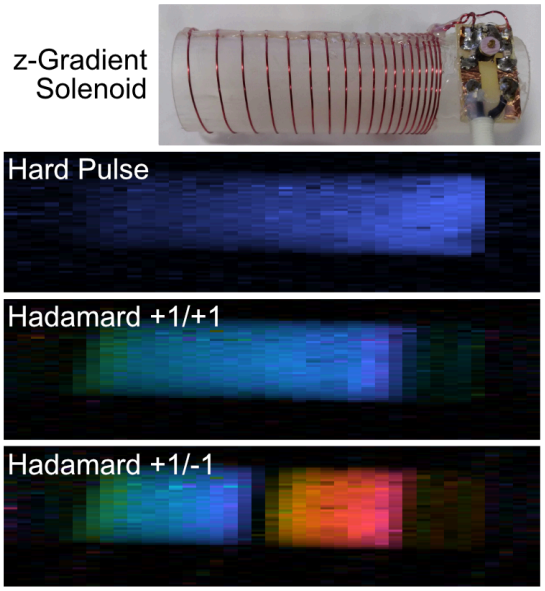


Figure 5.5: Image of excitation patterns produced by hard pulse and a 2-band $B_1^+$-selective Hadamard pulse. The Hadamard pulse does not excite the high $B_1$ because it was designed for a specific range of $B_1$, whereas the hard pulse does. A clear separation of the two bands can be seen in the excitation produced by the second pulse.

Figure 5.6 shows the 1D projection measured with the second encoding pulse of the 7.52 ms-long 8-subband Hadamard $B_1^+$-selective pulse with a passband center of 0.5 Gauss and a

passband width of 1 gauss and a flip angle of 90°. The projection was plotted over the length of the 11.5 cm mineral oil tube phantom used. The projection drops in amplitude along the length of the tube phantom, due to the receive sensitivity of the 10 cm loop coil. The distinguishable peaks represent each of the 8-subbands excited by the pulse, and were used to create the control hard pulse images by summing the complex image data over the bands locations.

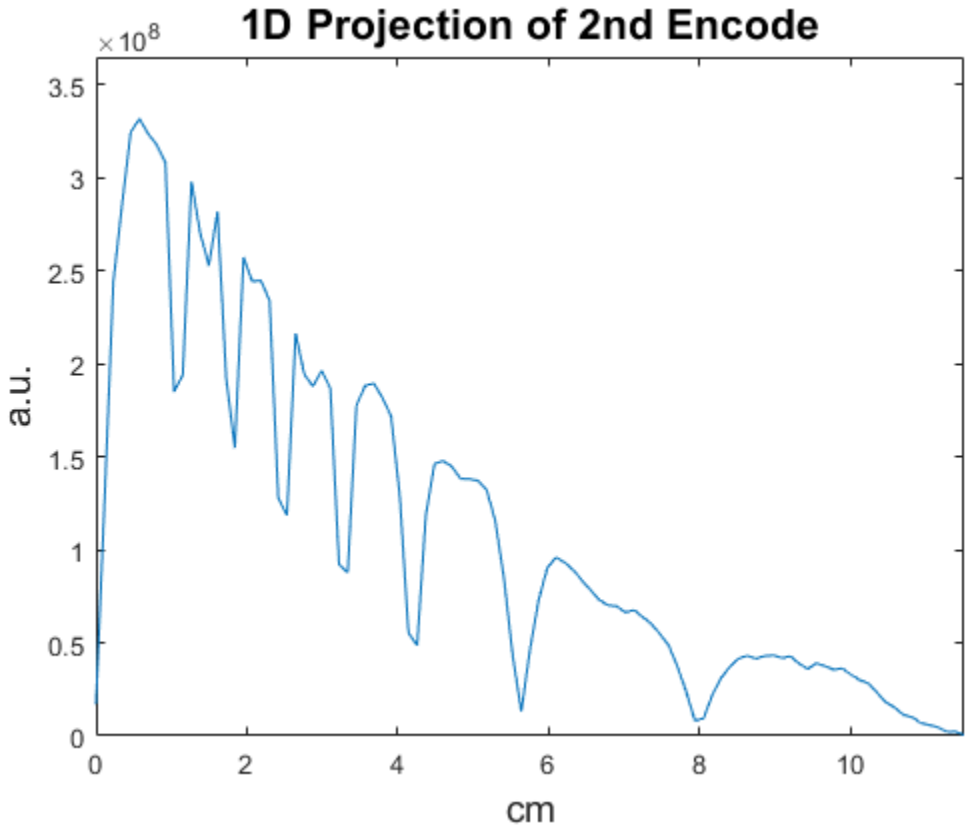


Figure 5.6: 1D projection measured with the second encoding pulse of the 7.52 ms-long 8-subband Hadamard $B_1^+$-selective pulse with a passband center of 0.5 Gauss and a passband width of 1 gauss and a flip angle of 90°. The projection was plotted over the length of the 11.5 cm mineral oil tube phantom used. The projection drops in amplitude along the length of the tube phantom due to the receive sensitivity of the 10 cm loop coil. The distinguishable peaks represent each of the 8-subbands excited by the pulse, and were used to create the control hard pulse images by summing the complex image data over the bands locations.

For the Hadamard $B_1^+$-selective spatial encoding experiment, the structure of each slice was consistent with the control images with the exception of higher signal levels at lower $B_1$ (Figure 5.7). This was expected due to the uniform excitation produced by the Hadamard pulses across $B_1$, versus the varying flip angle of the hard pulse excitation across the quadratic $B_1$ field. There was still some shading across the slices moving away from the coil and this was caused by the receive sensitivity of the loop coil.

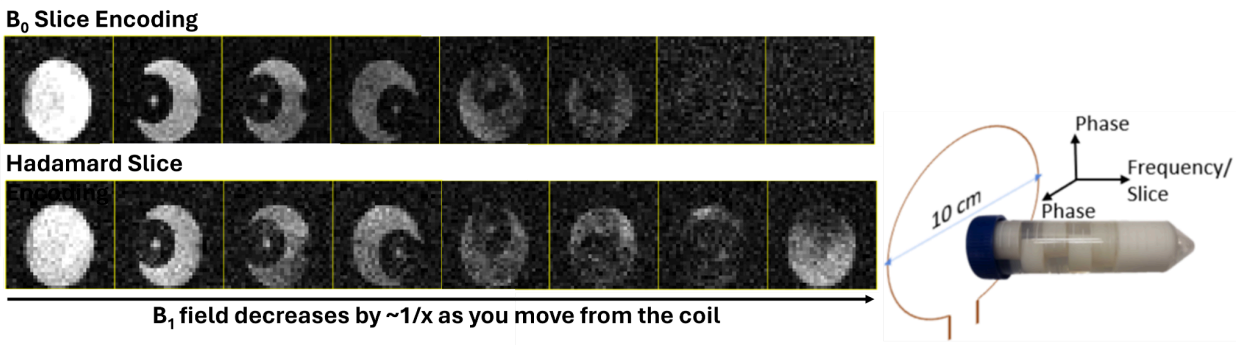


Figure 5.7: Results of an experiment using an 8 sub band $B_1^+$-selective Hadamard pulse for the encoding of the slice dimension in a GRE scan.

For the sweeping-band 1D spatial encoding experiment, the coefficients for the data sets collected for the two different positions of the mineral oil balls were plotted in Figure 5.8. The ball phantoms within this 1D projection were expected to have a Lorentzian shape, and this was what was observed in the reconstructed coefficients. The reconstructed coefficients have peaks centered at the expected phantom positions (6 cm, 0.5 Gauss and 9 cm, 0.75 Gauss) as well, showing proper spatial localization. The coefficients were a consistent amplitude for both phantom positions, meaning they reflect the spin density. This shows the capability of the $B_1^+$-selective pulses to perform spatial encoding and be reconstructed with a signal dictionary.

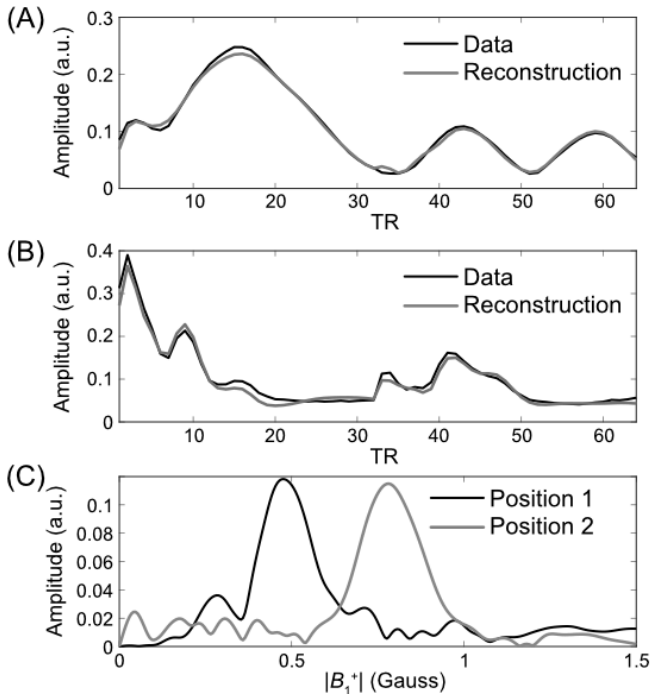


Figure 5.8: A) The measured signal from the mineral oil ball in position 1 plotted with the coefficients from the reconstruction of that phantom projected through the signal dictionary. B) The measured signal from the mineral oil ball in position 2 plotted with the coefficients from the reconstruction of that phantom projected through the signal dictionary. C) The coefficients for the mineral oil ball phantoms in positions 1 and 2.

Figure 5.9A shows the excitation bands for a 1.38 ms-long tanh-modulated control pulse with a passband center of 0.8 Gauss,a passband width of 1.6 Gauss, and a flip angle of 90°, and its undistorted excitation profile (Figure 5.9C). The same pulse, but with 20% amplifier droop applied over its duration is shown (Figure 5.9B) and the distorted excitation profile it produced (Figure 5.9D).

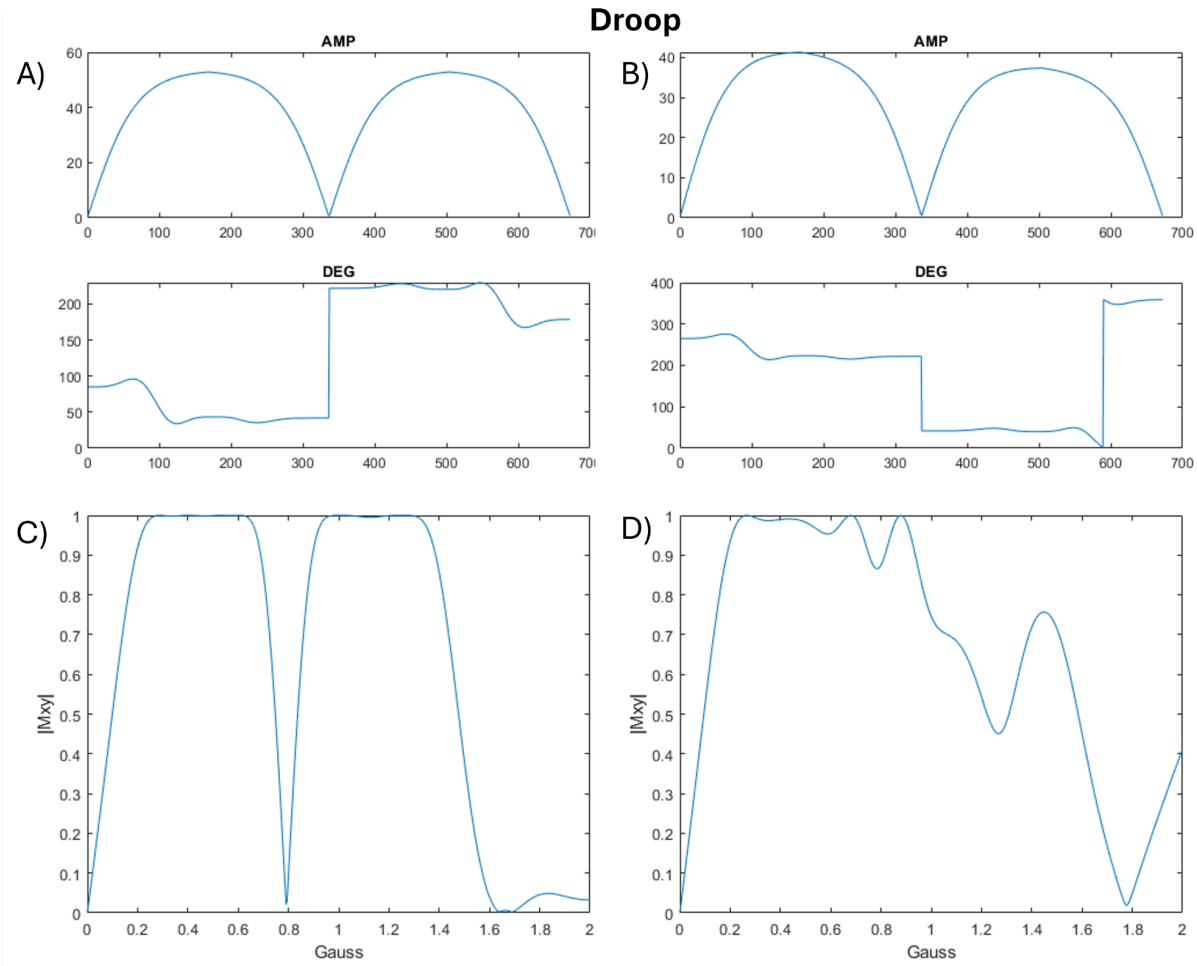


Figure 5.9: A) The amplitude (a.u.) and phase (°) of an ideal tanh modulated 2-subband Hadamard $B_1^+$-selective pulse. B) The amplitude and phase of a tanh modulated 2-subband Hadamard $B_1^+$-selective pulse distorted by 20% amplifier droop over the 1.38 ms pulse duration. C) The 2-subband $B_1$ profile of the ideal $B_1^+$-selective pulse. D) The profile of the distorted $B_1^+$-selective pulse. Even the seemingly insignificant pulse distortion leads to a massive profile distortion that makes the intended spatial encoding impossible.

Figure 5.10A shows the excitation bands for a 1.38 ms-long tanh-modulated control pulse with a passband center of 0.5 Gauss, a passband width of 1 Gauss, and a flip angle of 90°, and its undistorted excitation profile (Figure 5.10C). The same pulse distorted by the frequency response of the 12 cm gradient coil as measured by the $S_{11}$ reflection coefficient is shown (Figure 5.10B) and the distorted excitation profile it produced (Figure 5.10D).

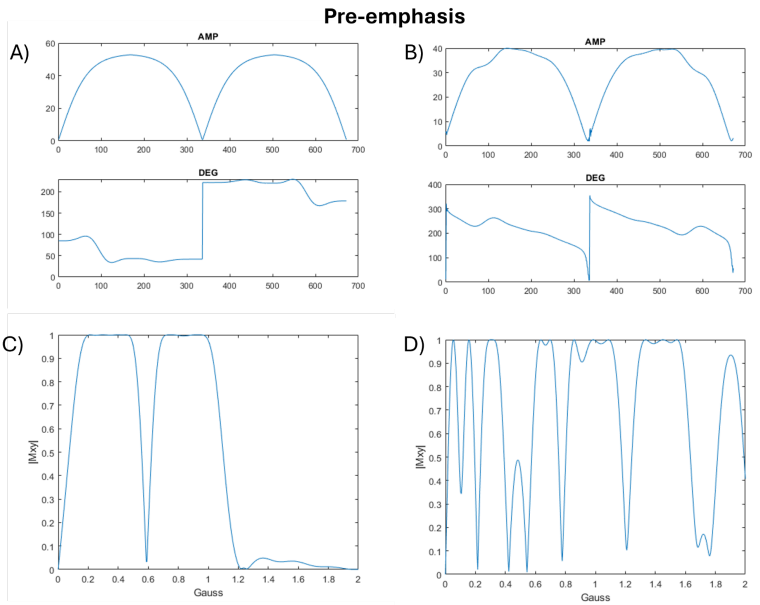


Figure 5.10: A) The amplitude (a.u.) and phase (°) of an ideal tanh modulated 2-subband Hadamard $B_1^+$-selective pulse. B) The amplitude and phase of a tanh modulated 2-subband Hadamard $B_1^+$-selective pulse distorted by the frequency response of the 12 cm gradient coil. C) The 2-subband $B_1$ profile of the ideal $B_1^+$-selective pulse. D) The profile of the distorted $B_1^+$-selective pulse. Even the seemingly insignificant pulse distortion leads to a massive profile distortion that makes the intended spatial encoding impossible.

As discussed in Chapter 3, $B_1^+$-selective pulses were designed to have a balanced amplitude waveform so that the final excitation created by the pulse was within the desired $B_1$ passband. However, RF waveform distortions caused by droop from the RF amplifier, frequency dependent amplitude attenuation of the RF coil, and higher order time-dependent distortions cause amplitude modulations that lead to an imbalanced waveform. When the amplitude waveforms were imbalanced, the excitation bands shift in $B_1$, and have variable flip angles over the excitation band and out of band excitations.

As a thought experiment, consider an object placed at 1.4 Gauss within the 0 to 2 Gauss range shown in Figure 5.10D. If this pulse in Figure 5.10B were used as an excitation in the first TR of a SENF sequence, the $|M_{xy}|$ acquired during that TR would be ~1, instead of the ~0

expected in Figure 5.10C if the pulse in Figure 5.10A was used. If a dictionary were constructed, this first data point would be strongly correlated to the 0 to 1.2 Gauss positions, even though there was no object present there.Therefore, the experimentally measured signal from that point forward would not match the correct dictionary entries for its $B_1$ position and the reconstruction could fail.

### 5.3.2 Hard pulse SENF Sequence

The three phantom configurations were accurately reconstructed within the four 2.5 cm voxel reconstruction, as shown in Figure 5.12, for the experimentally measured (Figure 5.11) and simulated dictionary reconstructions.

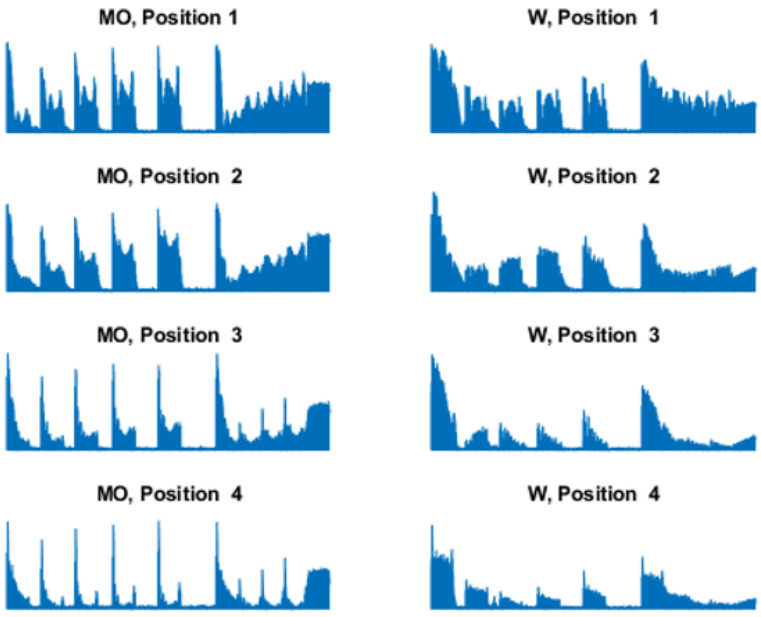


Figure 5.11: Experimentally measured dictionary entries for the first hard pulse SENF sequence experiment. There are eight entries equal to the four 2.5 cm voxels times the two materials, mineral oil and doped water.

Each reconstruction matched the experimental ball configuration in position and material type in both experiments, showing that spatial and quantitative encoding was possible with hard pulse SENF (Figure 5.12).

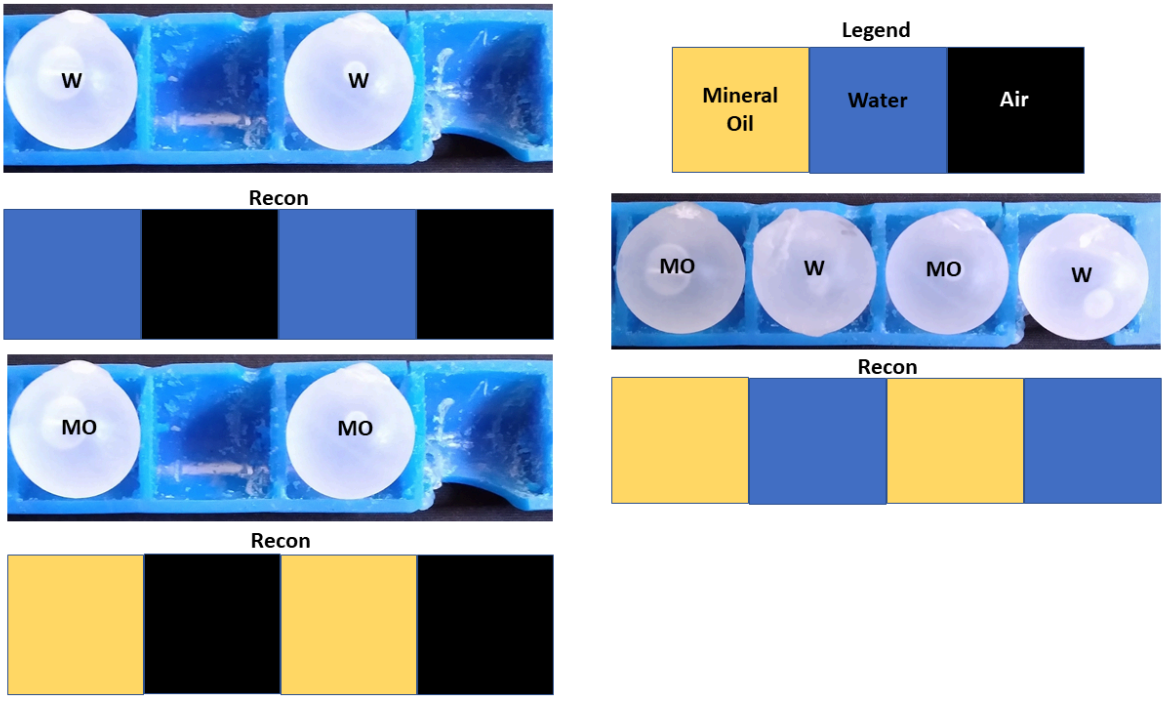


Figure 5.12: Three 4-voxel 1D reconstructions for the first two hard pulse SENF sequence experiments. The first was two water phantoms, the second was two mineral oil phantoms and the third was alternating mineral oil and water. Coefficients were thresholded. Any value below this threshold was considered to be air.

The two material hard pulse SENF experiment for adjacent water and mineral oil ball phantoms slid through the 8 cm imaging volume at 5 mm increments were reconstructed with a dictionary simulated for mineral oil and doped water at 1 mm spatial resolution. The reconstruction for the central position is shown in Figure 5.13. The coefficient peaks for mineral oil and water were centered properly at their expected positions and the amplitude of the coefficients were consistent implying they reflect spin density. The coefficients for the correct

material were also largest over their expected positions other than the 38-42 mm and 68-70 mm ranges where the materials were misclassified. There were also some coefficients present outside of the expected positions as well due to the imperfection of the spatial and quantitative encoding.

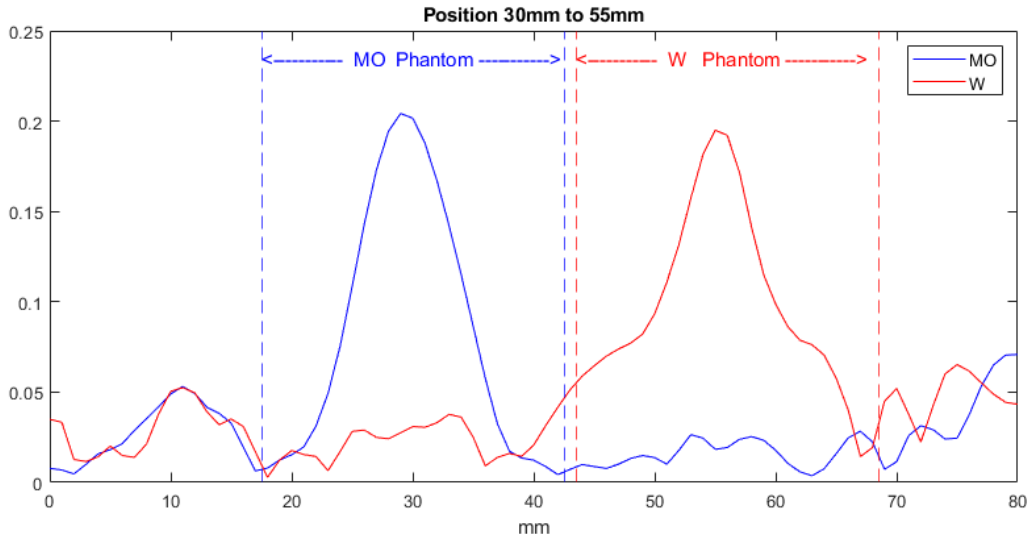


Figure 5.13: Reconstruction of a central position of the mineral oil and doped water phantoms. The dotted lines indicate the bounds of the expected positions of the ball phantoms.

### 5.3.3 Quadratic Phase Bloch-Siegert (qRF-BS) SENF Sequence

For the first qRF-BS SENF experiment, the mineral oil only ball phantom was reconstructed for the central position shown in Figure 5.14. The reconstruction coefficients were centered within its expected position, however the reconstruction coefficients were wider than the expected bounds of the phantom. This could be due to over-regularization or insufficient spatial resolution causing a broadening of the coefficient peak. The reconstruction coefficients for the simulated reconstruction for adjacent mineral oil and water phantoms were centered and filled the expected bounds of the phantoms, other than a small misclassification of doped water as mineral oil at the 36-38 mm range.

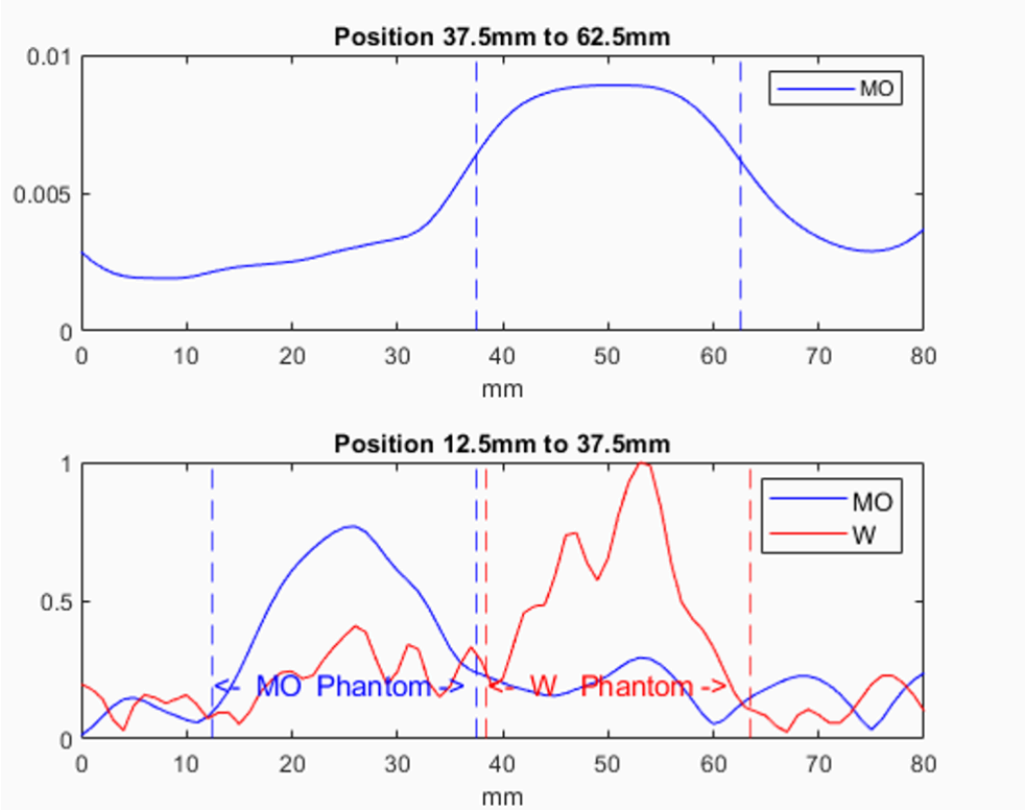


Figure 5.14: Top) Reconstruction of a centrally positioned mineral oil ball using the BS quadratic phase SENF method. Bottom) Simulated reconstruction of centrally positioned mineral oil and doped water balls using the BS quadratic phase SENF method.

The optimized flip angle schedule for the final qRF-BS SENF experiment reduced the error metric by 74.5% compared to the constant 50° flip angle sequence (Figure 5.15).

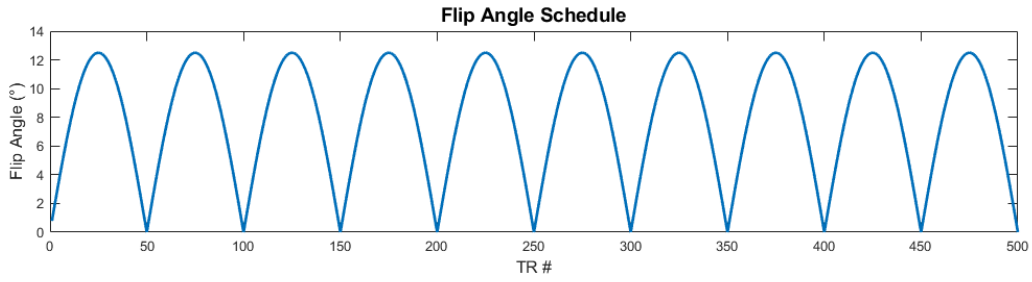


Figure 5.15: Optimized flip angle schedule with an average flip angle of 5° for the qRF-BS SENF experiment.

For the final qRF-BS SENF experiment, the mineral oil ball phantom was accurately reconstructed in the central position of the imaging volume (Figure 5.16). The reconstruction coefficients were centered properly within the expected bounds of the phantom, and no voxels were misclassified as doped water within the bounds of the phantom. The coefficients outside of the bounds cannot be removed with a single coefficient threshold, implying a limitation of the spatial and quantitative encoding of the sequence or a limitation of the reconstruction.

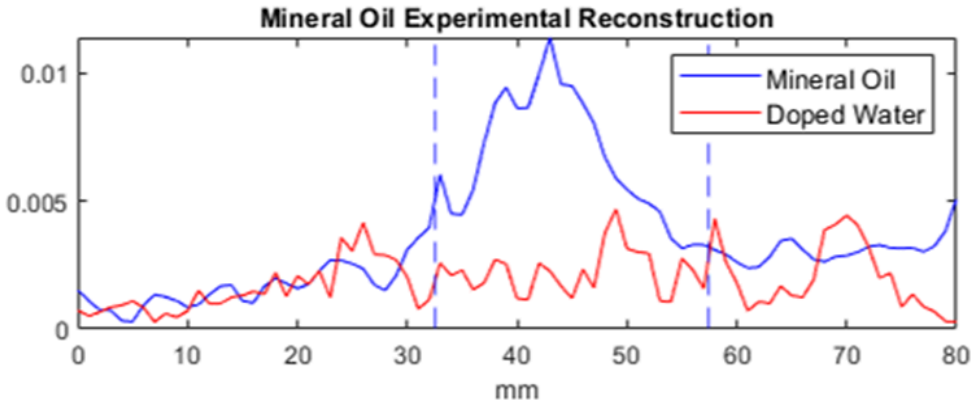


Figure 5.16: Reconstruction of a mineral oil ball phantom centered at 45 mm using a dictionary containing confounding doped water signals. Within the expected bounds of the phantom 0% of voxels are misclassified.

Figure 5.17 shows the susceptibility between a mineral oil 2.5 cm ball phantom centered at 25 mm and a doped water 2.5 cm ball phantom centered at 50 mm. The $B_0$ distribution was two opposing linear gradients across each phantom that span ~5 Hz each. The offset between the distributions was caused by the 7.243 Hz chemical shift between the materials.

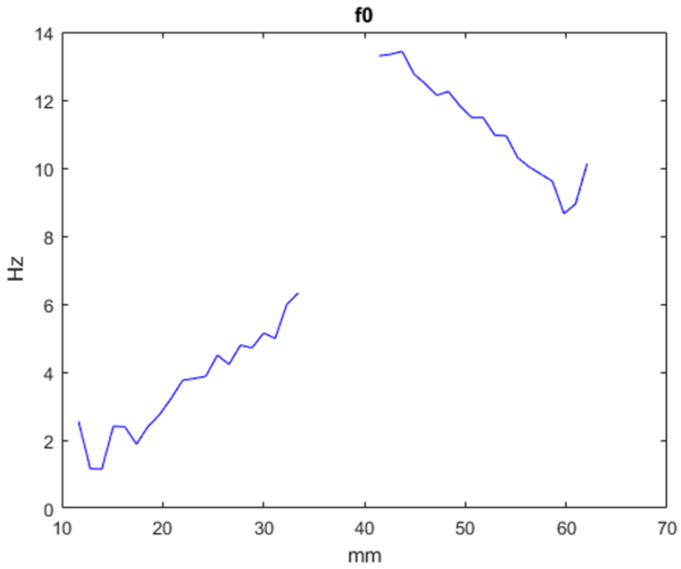


Figure 5.17: Susceptibility map between a mineral oil and doped water 2.5 cm ball phantom centered at 25 mm and 50 mm respectively. The result was an opposing linear $B_0$ gradient across the objects with a range of ~5 Hz, and an offset caused by chemical shift of 7.243 Hz.

### 5.4 Discussion and Conclusions

The first conceptualization of SENF discussed in Chapter 3 was the combination of work on $B_1^+$-selective excitation pulses (Grissom et al., 2014), Magnetic Resonance Fingerprinting (Ma et al., 2013) and a proof of principle simulation was performed to test the viability of SENF. In this simulation, a $T_1$ and $T_2$ 64 by 64 voxel parametric maps of a brain slice phantom were encoded and reconstructed. These reconstructions matched the brain slice phantom used to synthesize measured signals except for two voxels (0.05%) outside of the brain that were misclassified. Comparison simulations were performed for the three SENF sequences: $B_1^+$-selective SENF, hard pulse SENF, and qRF-BS SENF. These revealed the SENF sequences had comparable resolution (1-3 mm) to 7 mT/m gradients (1 mm) used on the 47.5 mT scanner, and comparable minimum SNR (18-37 SNR) to what was achieved for SENF sequences (24 SNR), which was further improved with additional averages. These promising results led to the desire to implement SENF

experimentally on our 47.5 mT low-field system. To do this, several pieces of hardware had to be constructed, including EMI shielding to achieve acceptable SNR; RF coils to produce inhomogeneous $B_1$ fields; uniform receive coils designed to acquire higher NMR signals; and a reed relay TR switch to enable high power non-distorted switching with strong isolation using an optimized gradients solenoid, with a nested saddle receive coil in combination with their innate geometric decoupling.

With all of this hardware in place, the implementation of the $B_1^+$-selective SENF sequence began with the goal of reproducing the proof of principle simulation results. This involved implementing the $B_1^+$-selective pulses onto our Tecmag Redstone Spectrometer and verifying the excitation patterns they created (Figure 5.5), as well as their ability to be used for spatial encoding in a slice encoding experiment (Figure 5.7) as well as a using $B_1^+$-selective pulses for spatial encoding with a dictionary reconstruction without the use of $B_0$ gradients (Figure 5.8). RF waveform distortions caused by the frequency dependent amplitude response of the coils, amplifier droop, and some uncharacterized higher order distortions limited the usability of the $B_1^+$-selective pulses despite attempts to correct for these with wide bandwidth coils, tanh envelope modulation and pre-emphasis of the pulses. The tanh envelope modulation, and wide $B_1$ passband widths allowed for the three successful $B_1^+$-selective pulse experiments that minimized unwanted excitation outside of the passband. However, these RF waveform distortions prevented the successful implementation of a two material $B_1^+$-selective SENF sequence experiment. To overcome these problems, our group began development on an AI based pre-emphasis that would account for these time-dependent effects (Albert et al., 2023). At the same time, low-cost on-coil amplifiers optimized for flat amplitude $B_1^+$-selective pulses were also in development at Case Western Reserve University that will minimize RF waveform distortions (Bolding et al.,

2022). Both of these approaches to correcting the RF waveform distortions are still in development, and RF waveform distortions are still a challenge on the 47.5 mT system.

The flexibility of SENF sequence design was used to overcome the RF waveform distortions. This was done by developing hard pulse SENF, which used constant amplitude zero phase pulses to create signal peaks and nulls throughout the imaging volume that were not sensitive to RF waveform distortions present on the system. These hard pulses have no phase modulation, therefore any RF waveform distortions only change the integrated area of the pulse, which can be corrected for with a global amplitude scalar which can be determined by sweeping through RF powers in a flip angle calibration FID sequence. Off-resonance dephasing during the pulse would break this assumption, but was minimal (< 10 Hz) on the 47.5 mT scanner. This effect was further reduced by minimizing the hard pulse lengths (~690 us). Three experiments were performed with hard pulse SENF. The first and second experiment reconstructed two materials in four 2.5 cm voxels for multiple phantom configurations using a measured and simulated dictionary respectively (Figure 5.13). The third experiment boasts a 1 mm resolution reconstruction of mineral oil and gadolinium doped water ball phantoms that was entirely SENF encoded and used a dictionary based reconstruction with only 9.9% of the FOV misclassified. This marked the first fully successful SENF experimental implementation where spatial and quantitative encoding were achieved. However, the coupling of the spatial and quantitative encoding mechanisms of the hard pulse SENF sequence proved a challenge when pursuing sequence optimization to further improve the spatial and quantitative resolution of SENF.

Again the flexibility of the SENF sequence design, inspired by quadratic RF MRF work (Boyacioglu et al., 2019), was leveraged to create qRF-BS SENF. This SENF sequence used quadratic phase modulation of hard pulse excitations and off-resonance pulses that imparted

spatially dependent phase onto spins to encode spatial information into the signals. Since the Bloch-Seigert pulses used were so far off-resonance, there was no excitation imparted onto the spins, and any RF waveform distortions that were time-dependent, like amplifier droop, simply affected the accrued phase imparted onto the spins, which could be corrected with a global RF power adjustment. Ideally, a square root $B_1$ field would be used to produce a linear phase across the imaging volume, giving uniform spatial resolution. However, over the 8 cm imaging volume the resolution only varied between 3-5 mm, and was not a limiting factor in reconstructions, and the optimized gradient solenoid was used. Two experiments were performed with the qRF-BS SENF sequence. The first reconstructed a mineral oil ball phantom with correct positioning, but a wider spin distribution than expected and a simulated adjacent mineral oil and doped water phantom with only the 36-38 mm positions misclassified (3.7% of the FOV) (Figure 5.15). The second experiment used an optimization to improve the flip angle schedule thanks to the independent spatial and quantitative encoding mechanisms. Using this optimized flip angle schedule, a mineral oil ball reconstruction with the presence of a confounding material in the dictionary with no misclassification within the expected phantom bounds. Further qRF-BS SENF experiments were attempted with adjacent mineral oil and doped water ball phantoms, however the dictionary simulations still differed by some unknown factor from experimental conditions causing failure in the reconstructions.

Overall, SENF was conceptualized and realized on a real world 47.5 mT system using the flexibility in the sequence design to create multiple SENF sequences to overcome practical limitations of the system it was implemented on. Simultaneous quantitative and spatial encoding using this new method of encoding MRI data was achieved on the 47.5 mT scanner. Each SENF sequence had varying degrees of success due to limitations in system knowledge, limiting

accurate dictionary construction, but promising results were achieved all the same. The ultimate goal of this work was to create an encoding method that can be implemented on cheap and portable MRI systems to improve accessibility of MRI and therefore the impact of MRI on health outcomes in a variety of low resource environments, and this work has laid the foundation for achieving this goal.

# CHAPTER 6: CONTRIBUTIONS AND FUTURE WORK

## 6.1 Summary and Conclusions

This thesis introduced a new method of encoding MRI data called Selective Encoding through Nutation and Fingerprinting (SENF). SENF allows for simultaneous encoding of spatial and quantitative information without the need for $B_0$ gradients. This was accomplished by using inhomogeneous $B_1$ fields, where pulses with $B_1$ dependent effects were transmitted during an MRF-type sequence to produce signals that were incoherent for different spatial locations and quantitative parameters. Quantitative maps could then be reconstructed using a dictionary based reconstruction and a regularized pseud- inverse. Quantitative maps are easily interpretable results that increase the usability of MRI alongside the increased accessibility that methods like SENF bring on low-field systems. Hardware components including EMI shielding and RF coils were developed to experimentally validate SENF on a low-field 47.5 mT scanner.

Chapter 3 reported a proof of concept simulation of SENF in which $T_1$ and $T_2$ maps of a 64 by 64 voxel brain slice were reconstructed with two misclassified voxels (0.05 %) outside the brain. That simulation used 64 modes of an 8-channel parallel transmit array to produce different inhomogeneous $B_1$ fields, through which 32-subband Hadamard $B_1^+$-selective excitation pulses were transmitted during an MRF-type sequence. A dictionary was constructed for six different $T_1$ and $T_2$ pairs for all 64 by 64 voxels and a simulated signal was constructed using a sum of entries from the dictionary that corresponded to a simulated brain phantom containing white matter, gray matter, and CSF. This was the first conceptualization of SENF that combined the ideas of $B_1^+$-selective excitation pulses with MRF. Three different SENF sequences were introduced: $B_1^+$-selective SENF, hard pulse SENF, and qRF-BS SENF. These three SENF sequences were compared in simulation with conventional $T_1$ IR and $T_2$ spin echo sequences

using resolution and minimum SNR metrics. These comparisons showed SENF has comparable resolution to conventional $B_0$ gradient methods and lower minimum SNR, although the minimum SNR was sufficient to experimentally implement SENF on a 47.5 mT scanner.

Chapter 4 covers the development of RF coils, EMI shielding and TR switches for the experimental validation of SENF with 1D projection imaging as the first implementation. Two iterations of EMI shielding were developed to provide adequate noise cancellation and ease of use for the experimental protocol. This shielding also improved conventional imaging on the 47.5 mT scanner, as none existed prior leading to excessive noise in acquisitions. A loop coil and gradient solenoid were used for $B_1^+$-selective pulse experiments before developing an optimized gradient solenoid with a nested saddle coil for receive. The high linearity of the optimized gradient solenoid combined with the high signal uniform receive facilitated the first implementation of SENF. The ability to use the uniform saddle coil for transmit made qRF SENF possible.

As shown in Chapter 5, limitations of the experimental setup including practical limitations of RF fidelity and encoding optimizations necessitated the development of three different SENF sequences, each overcoming a specific limitation. First, $B_1^+$-selective SENF was used since this was the sequence used in the proof of concept simulation. The RF fidelity of the transmit chain created distortions in the pulse profile that were too significant to implement the method beyond simple spatial encoding experiments. Hard pulse SENF was then developed as a sequence that would be insensitive to poor RF fidelity, allowing for 1D projection SENF reconstructions of mineral oil and doped water simultaneously at multiple locations within the experimental FOV. The independent optimization of spatial and quantitative encoding was not possible for hard pulse SENF, as the excitation patterns responsible for spatial encoding were

changed if the flip angle schedules used for quantitative encoding were changed. This led to the development of qRF SENF, which used the Bloch-Siegert shift and quadratic phase modulation of the excitation pulses for spatial encoding, leaving the flip angle schedule and therefore, the quantitative encoding decoupled from the spatial encoding.

The proof of principle simulation in Chapter 3 showed promising results for the first conceptualization of SENF, making the next logical step experimental implementation of SENF on a low-field scanner. Chapter 4 outlines the hardware developed for the experiments to allow for the experiments performed in Chapter 5. Limitations of the 47.5 mT scanner and hardware led to the development of three different SENF sequences for which experiments were performed in Chapter 5. A comparison simulation of the three SENF sequences was shown in Chapter 3 to evaluate the resolution and minimum SNR for each sequence, and compare them to conventional $T_1$ IR and $T_1$ spin echo sequences. The work done in this thesis has taken SENF from an idea to an experimentally realized quantitative encoding technique, which lays the foundation for future improvements to SENF, ultimately leading to clinical applications that improve health outcomes.

### 6.2 Future Work

The work in this thesis includes the conceptualization of SENF and a preliminary proof of concept simulation as well as the first experimental implementation of SENF in the form of 1D projection experiments. However, the potential clinical applications for SENF are broad and exciting. SENF can be implemented on a range of low-field scanner systems without $B_0$ gradients with different $B_0$ field geometries and inhomogeneous $B_1$ fields, due to SENF's flexibility. This leads to increased accessibility to MRI, specifically using SENF to simultaneously encode spatial and quantitative information. SENFallows for multiple parametric maps to be acquired

simultaneously, and these parameters could be combined and used as a biomarker of different diseased tissues without the need for subjective interpretation of conventional MRI. The development of SENF increases usability along with accessibility of MRI to have larger impacts on patient outcomes. SENF could be used for low-cost screening applications that can be implemented in low resource environments. This section will cover some short term experimental improvements that will further the development of SENF, as well as some potential clinical applications.

### 6.2.1 Low-cost on-coil amplifiers for $B_1^+$-selective pulses

SENF does not require $B_0$ gradients, lowering the cost requirements of the low-field systems it can be implemented on. This cost can further be reduced using low-cost on-coil amplifiers that are optimized for flat pulses using frequency modulation are being developed by colleagues at Case Western Reserve University. These allow for highly efficient amplifiers with a simplified design due to no required amplitude modulation, but simply the faithful replication of frequency variations. These amplifiers are specially developed for flat amplitude pulses like $B_1^+$-selective pulses used for $B_1^+$-selective SENF. This improved RF fidelity will reduce distortions of the excitation profiles of the $B_1^+$-selective pulses reducing variations between experimental encoding patterns and the assumed encoding patterns used in dictionary calculations, which ultimately improved the SENF reconstructions. This will allow for improvements upon the current $B_1^+$-selective experiments, as the RF waveform distortions were the main limitation to improving the achieved experimental implementation.

### 6.2.2 2D $B_1^+$-Selective SENF experiments

A 0.1 T scanner with good $B_0$ homogeneity and stability will be available for SENF experiments at Case Western Reserve University. The improved $B_0$ homogeneity will reduce distortions of the $B_1^+$-selective pulses, which are a limitation to improving upon the achieved experimental implementation. These inhomogeneities were small over the 8 $cm^3$ imaging volume, but would be much larger over a full head volume on the 47.5 mT scanner, leading to excitation profile distortions. The improved $B_0$ stability will alleviate the need to account for scanner drift, reducing overall scan time by removing the FID drift navigator and reducing any dissonance between the dictionary calculations and experimental measurements $B_0$ instability can cause. Using the low-cost on-coil amplifiers and a parallel transmit array, a 2D $B_1^+$-selective SENF experiment can be performed similar to the proof of concept simulation reported in this thesis. With the improved $B_0$ homogeneity and stability alongside the high RF waveform fidelity, provided by the amplifiers and their implementation on a pTx array, the assumptions of the proof of concept 2D SENF simulation are more accurately met, which will allow for a 2D $B_1^+$-selective SENF experiment.

### 6.2.3 Implementation of different SENF sequences on 0.1 T scanner

The 0.1 T scanner can also be used to improve implementations of hard pulse and qRF-BS SENF and potentially expand the experiments to 2D. Hard pulse and qRF-BS SENF are less sensitive to $B_1$ distortions, meaning the improved RF fidelity from the amplifiers will have a smaller impact. That being said, the RF waveform distortions will not be significantly different from assumed ideal conditions in the simulations of different sequence designs for these sequences. This will reduce the need to reoptimize sequence designs based on measured RF fidelity imperfections.

The qRF-BS SENF sequence is fairly insensitive to off-resonance, thanks to the two polarities of off-resonance pulses used for the sequence currently. With improved $B_0$ homogeneity, the need for both polarities will be reduced, which can lead to shorter sequences, or more TRs being used for uniquely encoding information. Again, the improved $B_0$ stability will reduce sequence time and the accuracy of dictionary calculations as discussed above.

### 6.2.4 3D SENF for phantoms and in vivo

Following the 2D SENF experiments that will adhere to a protocol similar to the proof of concept simulation, 3D SENF will be explored. This will require additional encoding of the third dimension. This may be accomplished using the Bloch-Siegert shift and an inhomogeneous RF coil. This coil would be constructed of many loops placed around a cylindrical former or be a gradient solenoid depending on the level of geometric decoupling necessary alongside active decoupling methods to perform experiments. Transmitting an off-resonant pulse through this coil would produce a phase gradient across the spins analogous to traditional $B_0$ gradients. This would allow for potentially a full dictionary reconstruction or some sort of combined reconstruction of 3D quantitative maps. The addition of a third dimension for encoding brings SENF's capabilities closer to standard $B_0$ encoded MRI techniques. These would be initially performed on phantoms and eventually in vivo. Performing these experiments in vivo is a necessary step for SENF to be clinically useful since it will be used for imaging patients. The challenges for in vivo imaging have to be overcome, including increased physiological noise and SAR limitations for high quality and safe patient imaging. Overcoming these challenges then opens up the use of SENF for different clinical applications.

### 6.2.5 Improvements to SENF encoding

Within this thesis, SENF was used for a proof of principle simulation to reconstruct a 64 by 64 voxel brain slice phantom. While resolution is harder to define in 2D, with SENF encoding as the point spread functions of different voxels vary across space, the brain was reconstructed with only two misclassified voxels outside of the brain. The dictionary used for this reconstruction only used three materials present in the phantom: white matter, gray matter and CSF, as well as three confounding materials that were not present. This leads to a total of six $T_1$ and $T_2$ pairs. Ideally, a range of $T_1$ and $T_2$ values would be used to allow for identification of many different tissues. For example not only white matter, gray matter and CSF, but also infarct white matter to identify stroke, or different types of brain tumors. If SENF is used for asymptomatic screening applications, a wide range of parameters would need to be covered, so that different healthy and diseased tissues could be identified. This presents two challenges: 1) the sequence design for SENF must be improved to be capable of encoding $T_1$ and $T_2$ values with small separations; and 2) dictionary calculation and SENF reconstructions must be improved to deal with the multiplicative increase in size that more quantitative parameters bring. To address the first challenge, optimization of encoding patterns and sequence parameter schedules are required to improve the encoding power of SENF. Increased dictionary size can initially be addressed by using virtual machines with high amounts of RAM, but moving forward will require some variation of mini-batching or singular value decomposition compression to reduce memory requirements for calculations. .

### 6.2.6 Potential clinical applications

SENF will be implemented on low-field systems that do not require $B_0$ gradients and use low-cost on-coil amplifiers. These lower cost systems along with all the general benefits of low-field as discussed in Chapter 1, improve the accessibility of MRI. With this increased accessibility, the results of SENF must be easier to interpret than traditional MRI images that require radiologists to interpret, so it can be used in low resource environments, such as outpatient care, rural settings, or low-income countries. The multiple quantitative parameters provided by SENF, such as $T_1$, $T_2$ and potentially other metrics, can be combined to make a biomarker for different disease states. These biomarkers could be uniquely identifiable for different diseases, while being purely quantitative, removing the need for subjective interpretation of contrast images. This would make SENF an ideal tool for screening for diseases that have improved outcomes if diagnosed earlier such as heart disease or cancers. A SENF scan for screening could be done during routine medical exams, at lower cost, to screen for heart disease and cancers. The results of the SENF scan would not have to be a set of quantitative maps, but rather, provide a likelihood of a certain disease state being present based on the biomarkers identified in a scan. This could then serve as a recommendation for a followup diagnosis using more precise albeit more expensive established methods in a hospital setting. This would serve as preventative care that is not currently viable with the cost of MRI, which can be upwards of $1600 per scan.

## REFERENCES


Albert M. M., Vaughn C. E., Martin J. B., Srinivas S. A., and Grissom W. A. (2023). RF Pulse Predistortion for Low-Field MRI Based on Spin Physics Using a Neural Network Amplifier-to-Bloch Equation Model. In *ISMRM*, pages 4563-4563.

American Cancer Society. (2022). Risk of Dying from Cancer Continues to Drop at an Accelerated Pace. https://www.cancer.org/research/acs-research-news/facts-and-figures-2022.html#:~:text=Cancer%20continues%20to%20be%20the,about%201%2C670%20deaths%20a%20day.

Arnold, T. C., Freeman, C. W., Litt, B., & Stein, J. M. (2023). Low-field MRI: Clinical promise and challenges. Journal of magnetic resonance imaging : JMRI, 57(1), 25–44. https://doi.org/10.1002/jmri.28408

Arnold, T. C., Tu, D., Okar, S. V., Nair, G., By, S., Kawatra, K. D., Robert-Fitzgerald, T. E., Desiderio, L. M., Schindler, M. K., Shinohara, R. T., Reich, D. S., & Stein, J. M. (2022). Sensitivity of portable low-field magnetic resonance imaging for multiple sclerosis lesions. *NeuroImage. Clinical, 35*, 103101. https://doi.org/10.1016/j.nicl.2022.103101

Badve, C., Yu, A., Rogers, M., Ma, D., Liu, Y., Schluchter, M., Sunshine, J., Griswold, M., & Gulani, V. (2015). Simultaneous T1 and T2 Brain Relaxometry in Asymptomatic Volunteers using Magnetic Resonance Fingerprinting. *Tomography (Ann Arbor, Mich.), 1*(2), 136–144. https://doi.org/10.18383/j.tom.2015.00166

Badve, C., Yu, A., Dastmalchian, S., Rogers, M., Ma, D., Jiang, Y., Margevicius, S., Pahwa, S., Lu, Z., Schluchter, M., Sunshine, J., Griswold, M., Sloan, A., & Gulani, V. (2017). MR Fingerprinting of Adult Brain Tumors: Initial Experience. *AJNR. American journal of neuroradiology, 38*(3), 492–499. https://doi.org/10.3174/ajnr.A5035

Baker, M. A., & MacKay, S. (2021). Please be upstanding - A narrative review of evidence comparing upright to supine lumbar spine MRI. *Radiography (London, England : 1995), 27*(2), 721–726. https://doi.org/10.1016/j.radi.2020.11.003

Bercovich, E., & Javitt, M. C. (2018). Medical Imaging: From Roentgen to the Digital Revolution, and Beyond. *Rambam Maimonides medical journal, 9*(4), e0034. https://doi.org/10.5041/RMMJ.10355

Bolding N. R., Vaughn C. E., Blades-Thomas C., Grissom W. A., and Griswold M. A. (2022). Low-cost Modular RFPA Platform for Gradient-Free Quantitative Imaging. In *ISMRM Low-field Workshop*.

Boyacioglu R., Wang C., Ma D., McGivney D., Yu X., and Griswold M. (2019). 3D Magnetic Resonance Fingerprinting with Quadratic RF Phase. In *ISMRM*, pages 0806-0806.

Bray, F., Ferlay, J., Soerjomataram, I., Siegel, R. L., Torre, L. A., & Jemal, A. (2018). Global cancer statistics 2018: GLOBOCAN estimates of incidence and mortality worldwide for 36 cancers in 185 countries. *CA: a cancer journal for clinicians, 68*(6), 394–424. https://doi.org/10.3322/caac.21492

Burgio, E., Piscitelli, P., & Migliore, L. (2018). Ionizing Radiation and Human Health: Reviewing Models of Exposure and Mechanisms of Cellular Damage. An Epigenetic Perspective. *International journal of environmental research and public health, 15*(9), 1971. https://doi.org/10.3390/ijerph15091971

Chiragzada, S., Hellman, E., Michael, D., Narayanan, R., Nacev, A., & Kumar, D. (2021). Initial phantom studies for an office-based low-field MR system for prostate biopsy. *International journal of computer assisted radiology and surgery, 16*(5), 741–748. https://doi.org/10.1007/s11548-021-02364-7

Cooley, C. Z., Stockmann, J. P., Armstrong, B. D., Sarracanie, M., Lev, M. H., Rosen, M. S., & Wald, L. L. (2015). Two-dimensional imaging in a lightweight portable MRI scanner without gradient coils. *Magnetic resonance in medicine, 73*(2), 872–883. https://doi.org/10.1002/mrm.25147

.

Conolly, S., Nishimura, D., Macovski, A., & Glover, G. (1988). Variable-rate selective excitation. *Journal of Magnetic Resonance, 78*(3), 440–458. https://doi.org/10.1016/0022-2364(88)90131-x

de Graaf R. A. , Juchem C. (2016). B0 shimming technology. In: Webb AG, editor. *Magn Reson Technol Hardw Syst Compon Des.* Royal Society of Chemistry;. pp. 166–207. http://dx.doi.org/10.1039/9781782623878.

Dean, K. I., & Komu, M. (1994). Breast tumor imaging with ultra low field MRI. *Magnetic resonance imaging, 12*(3), 395–401. https://doi.org/10.1016/0730-725x(94)92532-1

Deoni, S. C. L., Bruchhage, M. M. K., Beauchemin, J., Volpe, A., D'Sa, V., Huentelman, M., & Williams, S. C. R. (2021). Accessible pediatric neuroimaging using a low field strength MRI scanner. *NeuroImage, 238*, 118273. https://doi.org/10.1016/j.neuroimage.2021.118273

Deoni, S. C. L., Medeiros, P., Deoni, A. T., Burton, P., Beauchemin, J., D'Sa, V., Boskamp, E., By, S., McNulty, C., Mileski, W., Welch, B. E., & Huentelman, M. (2022). Development of a mobile low-field MRI scanner. *Scientific reports, 12*(1), 5690. https://doi.org/10.1038/s41598-022-09760-2

Does, M. D., & Snyder, R. E. (1996). Multiexponential T2 relaxation in degenerating peripheral nerve. *Magnetic resonance in medicine, 35*(2), 207–213. https://doi.org/10.1002/mrm.1910350212

Does, M. D., & Snyder, R. E. (1995). T2 relaxation of peripheral nerve measured in vivo. *Magnetic resonance imaging, 13*(4), 575–580. https://doi.org/10.1016/0730-725x(94)00138-s

Dupuis, A., Chen, Y., Hansen, M., Chow, K., Sun, J. E. P., Badve, C., Ma, D., Griswold, M. A., & Boyacioglu, R. (2024). Quantifying 3D MR fingerprinting (3D-MRF) reproducibility across subjects, sessions, and scanners automatically using MNI atlases. *Magnetic resonance in medicine, 91*(5), 2074–2088. https://doi.org/10.1002/mrm.29983

FDA. (1998). Guidance for industry: Guidance for the submission of premarket notifications for magnetic resonance diagnostic devices

Feigin, V. L., Norrving, B., & Mensah, G. A. (2017). Global Burden of Stroke. *Circulation research, 120*(3), 439–448. https://doi.org/10.1161/CIRCRESAHA.116.308413

Ferlay, J., Colombet, M., Soerjomataram, I., Parkin, D. M., Piñeros, M., Znaor, A., & Bray, F. (2021). Cancer statistics for the year 2020: An overview. *International journal of cancer,* 10.1002/ijc.33588. Advance online publication. https://doi.org/10.1002/ijc.33588

Fry, A., Littlejohns, T. J., Sudlow, C., Doherty, N., Adamska, L., Sprosen, T., Collins, R., & Allen, N. E. (2017). Comparison of Sociodemographic and Health-Related Characteristics of UK Biobank Participants With Those of the General Population. *American journal of epidemiology, 186*(9), 1026–1034. https://doi.org/10.1093/aje/kwx246

Garavan, H., Bartsch, H., Conway, K., Decastro, A., Goldstein, R. Z., Heeringa, S., Jernigan, T., Potter, A., Thompson, W., & Zahs, D. (2018). Recruiting the ABCD sample: Design considerations and procedures. *Developmental cognitive neuroscience, 32*, 16–22. https://doi.org/10.1016/j.dcn.2018.04.004

Grissom, W. A., Cao, Z., & Does, M. D. (2014). |B1(+)|-selective excitation pulse design using the Shinnar-Le Roux algorithm. *Journal of magnetic resonance (San Diego, Calif. : 1997), 242*, 189–196. https://doi.org/10.1016/j.jmr.2014.02.012

Guerini, H., Omoumi, P., Guichoux, F., Vuillemin, V., Morvan, G., Zins, M., Thevenin, F., & Drape, J. L. (2015). Fat Suppression with Dixon Techniques in Musculoskeletal Magnetic Resonance Imaging: A Pictorial Review. *Seminars in musculoskeletal radiology, 19*(4), 335–347. https://doi.org/10.1055/s-0035-1565913

Hamilton, J. I., Jiang, Y., Eck, B., Griswold, M., & Seiberlich, N. (2020). Cardiac cine magnetic resonance fingerprinting for combined ejection fraction, T1 and T2 quantification. *NMR in biomedicine, 33*(8), e4323. https://doi.org/10.1002/nbm.4323

Hasselwander C. J. and Grissom W. A. (2017). Bloch-Siegert Phase-Encoded MRI with a Single RF Coil and Frequency-Swept Pulses. In *ISMRM*, pages 5047-5047.

Hori, M., Hagiwara, A., Goto, M., Wada, A., & Aoki, S. (2021). Low-Field Magnetic Resonance Imaging: Its History and Renaissance. *Investigative radiology, 56*(11), 669–679. https://doi.org/10.1097/RLI.0000000000000810

Hoult D. I. (1980). Rotating frame zeugmatography. *Philosophical transactions of the Royal Society of London. Series B, Biological sciences, 289*(1037), 543–547. https://doi.org/10.1098/rstb.1980.0074

Jaubert, O., Cruz, G., Bustin, A., Schneider, T., Koken, P., Doneva, M., Rueckert, D., Botnar, R. M., & Prieto, C. (2020). Free-running cardiac magnetic resonance fingerprinting: Joint T1/T2 map and Cine imaging. *Magnetic resonance imaging, 68*, 173–182. https://doi.org/10.1016/j.mri.2020.02.005

Jiang, Y., Ma, D., Seiberlich, N., Gulani, V., & Griswold, M. A. (2015). MR fingerprinting using fast imaging with steady state precession (FISP) with spiral readout. *Magnetic resonance in medicine, 74*(6), 1621–1631. https://doi.org/10.1002/mrm.25559

Manso Jimeno, M., Vaughan, J. T., & Geethanath, S. (2023). Superconducting magnet designs and MRI accessibility: A review. *NMR in biomedicine*, e4921. Advance online publication. https://doi.org/10.1002/nbm.4921

Johansen-Berg, H., & Behrens, T. E. (2006). Just pretty pictures? What diffusion tractography can add in clinical neuroscience. *Current opinion in neurology, 19*(4), 379–385. https://doi.org/10.1097/01.wco.0000236618.82086.01

Kasban H., El-Bendary M., and Salama D. (2015). A Comparative Study of Medical Imaging Techniques. *International Journal of Information Science and Intelligent System. 4.* 37-58.

Katscher, U., & Börnert, P. (2006). Parallel RF transmission in MRI. *NMR in biomedicine, 19*(3), 393–400. https://doi.org/10.1002/nbm.1049

Katscher, U., Lisinski, J., & Börnert, P. (2010). RF encoding using a multielement parallel transmit system. *Magnetic resonance in medicine, 63*(6), 1463–1470. https://doi.org/10.1002/mrm.22439

Keenan, K. E., Ainslie, M., Barker, A. J., Boss, M. A., Cecil, K. M., Charles, C., Chenevert, T. L., Clarke, L., Evelhoch, J. L., Finn, P., Gembris, D., Gunter, J. L., Hill, D. L. G., Jack, C. R., Jr, Jackson, E. F., Liu, G., Russek, S. E., Sharma, S. D., Steckner, M., Stupic, K. F., … Zheng, J. (2018). Quantitative magnetic resonance imaging phantoms: A review and the need for a system phantom. *Magnetic resonance in medicine, 79*(1), 48–61. https://doi.org/10.1002/mrm.26982

Körzdörfer, G., Kirsch, R., Liu, K., Pfeuffer, J., Hensel, B., Jiang, Y., Ma, D., Gratz, M., Bär, P., Bogner, W., Springer, E., Lima Cardoso, P., Umutlu, L., Trattnig, S., Griswold, M., Gulani, V., & Nittka, M. (2019). Reproducibility and Repeatability of MR Fingerprinting Relaxometry in the Human Brain. *Radiology, 292*(2), 429–437. https://doi.org/10.1148/radiol.2019182360

Lento, P. H., & Primack, S. (2008). Advances and utility of diagnostic ultrasound in musculoskeletal medicine. *Current reviews in musculoskeletal medicine, 1*(1), 24–31. https://doi.org/10.1007/s12178-007-9002-3

Ma, D., Gulani, V., Seiberlich, N., Liu, K., Sunshine, J. L., Duerk, J. L., & Griswold, M. A. (2013). Magnetic resonance fingerprinting. *Nature, 495*(7440), 187–192. https://doi.org/10.1038/nature11971

Martin, J. B., Srinivas, S. A., Vaughn, C. E., Sun, H., Griswold, M. A., & Grissom, W. A. (2022). Selective excitation localized by the Bloch-Siegert shift and a B1+ gradient. *Magnetic resonance in medicine, 88*(3), 1081–1097. https://doi.org/10.1002/mrm.29271

Mateen, F. J., Cooley, C. Z., Stockmann, J. P., Rice, D. R., Vogel, A. C., & Wald, L. L. (2021). Low-field portable brain MRI in CNS demyelinating disease. *Multiple sclerosis and related disorders, 51*, 102903. https://doi.org/10.1016/j.msard.2021.102903

Miloushev, V. Z., Keshari, K. R., & Holodny, A. I. (2016). Hyperpolarization MRI: Preclinical Models and Potential Applications in Neuroradiology. Topics in magnetic resonance imaging : *TMRI, 25*(1), 31–37. https://doi.org/10.1097/RMR.0000000000000076

Mittendorff, L., Young, A., & Sim, J. (2022). A narrative review of current and emerging MRI safety issues: What every MRI technologist (radiographer) needs to know. *Journal of medical radiation sciences, 69*(2), 250–260. https://doi.org/10.1002/jmrs.546

Nasri J., Wagaskar V. G., Parekha S., Adams J. D., Jr., Kumar D., Venkataraman S. S., Tewari A. K. (2021). Office‐based, point‐of‐care, low‐field MRI system to guide prostate interventions: Recent developments. *EMJ Urol. 2021;9*[1]:83-90.

NIH. (2021). Overweight & Obesity Statistics https://www.niddk.nih.gov/health-information/health-statistics/overweight-obesity

Nogueira, R. G., Jadhav, A. P., Haussen, D. C., Bonafe, A., Budzik, R. F., Bhuva, P., Yavagal, D. R., Ribo, M., Cognard, C., Hanel, R. A., Sila, C. A., Hassan, A. E., Millan, M., Levy, E. I., Mitchell, P., Chen, M., English, J. D., Shah, Q. A., Silver, F. L., Pereira, V. M., … DAWN Trial Investigators (2018). Thrombectomy 6 to 24 Hours after Stroke with a Mismatch between Deficit and Infarct. *The New England journal of medicine, 378*(1), 11–21. https://doi.org/10.1056/NEJMoa1706442

Noyes, K., & Weinstock-Guttman, B. (2013). Impact of diagnosis and early treatment on the course of multiple sclerosis. *The American journal of managed care, 19*(17 Suppl), s321–s331.

Ogbole, G. I., Adeyomoye, A. O., Badu-Peprah, A., Mensah, Y., & Nzeh, D. A. (2018). Survey of magnetic resonance imaging availability in West Africa. *The Pan African medical journal, 30*, 240. https://doi.org/10.11604/pamj.2018.30.240.14000

Pääkkö, E., Reinikainen, H., Lindholm, E. L., & Rissanen, T. (2005). Low-field versus high-field MRI in diagnosing breast disorders. *European radiology, 15*(7), 1361–1368. https://doi.org/10.1007/s00330-005-2664-6

Panda A., Chen Y., Vinayak S., and Griswold M. A. (2017). 3D Magnetic Resonance Fingerprinting for Quantitative Imaging in Breast Cancer. In *ISMRM Workshop on Magnetic Resonance Fingerprinting*.

Panda, A., Obmann, V. C., Lo, W. C., Margevicius, S., Jiang, Y., Schluchter, M., Patel, I. J., Nakamoto, D., Badve, C., Griswold, M. A., Jaeger, I., Ponsky, L. E., & Gulani, V. (2019). MR Fingerprinting and ADC Mapping for Characterization of Lesions in the Transition Zone of the Prostate Gland. *Radiology, 292*(3), 685–694. https://doi.org/10.1148/radiol.2019181705

Parker, S. A., Bowry, R., Wu, T. C., Noser, E. A., Jackson, K., Richardson, L., Persse, D., & Grotta, J. C. (2015). Establishing the first mobile stroke unit in the United States. *Stroke, 46*(5), 1384–1391. https://doi.org/10.1161/STROKEAHA.114.007993

Preston D. C. (2016). Magnetic Resonance Imaging (MRI) of the Brain and Spine: Basics https://case.edu/med/neurology/NR/MRI%20Basics.htm

Raschle, N., Zuk, J., Ortiz-Mantilla, S., Sliva, D. D., Franceschi, A., Grant, P. E., Benasich, A. A., & Gaab, N. (2012). Pediatric neuroimaging in early childhood and infancy: challenges and practical guidelines. *Annals of the New York Academy of Sciences, 1252*, 43–50. https://doi.org/10.1111/j.1749-6632.2012.06457.x

Riis T., Webb T., & Kubanek J.. (2021). Acoustic properties across the human skull. *Ultrasonics. 119*. 106591. 10.1016/j.ultras.2021.106591.

Rioux, J. A., Levesque, I. R., & Rutt, B. K. (2016). Biexponential longitudinal relaxation in white matter: Characterization and impact on T1 mapping with IR-FSE and MP2RAGE. *Magnetic resonance in medicine, 75*(6), 2265–2277. https://doi.org/10.1002/mrm.25729

Sarracanie, M., LaPierre, C. D., Salameh, N., Waddington, D. E. J., Witzel, T., & Rosen, M. S. (2015). Low-Cost High-Performance MRI. *Scientific reports, 5*, 15177. https://doi.org/10.1038/srep15177

Serai S. D. (2022). Basics of magnetic resonance imaging and quantitative parameters T1, T2, T2*, T1rho and diffusion-weighted imaging. *Pediatric radiology, 52*(2), 217–227. https://doi.org/10.1007/s00247-021-05042-7

Seton, H. C., Hutchison, J. M., & Bussell, D. M. (1999). Gradiometer pick-up coil design for a low field SQUID-MRI system. *Magma (New York, N.Y.), 8*(2), 116–120. https://doi.org/10.1007/BF02590528

Sharafi, A., Chang, G., & Regatte, R. R. (2018). Biexponential T2 relaxation estimation of human knee cartilage in vivo at 3T. *Journal of magnetic resonance imaging : JMRI, 47*(3), 809–819. https://doi.org/10.1002/jmri.25778

Sharp, J. C., & King, S. B. (2010). MRI using radiofrequency magnetic field phase gradients. Magnetic resonance in medicine, 63(1), 151–161. https://doi.org/10.1002/mrm.22188

Shen, S., Xu, Z., Koonjoo, N., & Rosen, M. S. (2021). Optimization of a Close-Fitting Volume RF Coil for Brain Imaging at 6.5 mT Using Linear Programming. *IEEE transactions on bio-medical engineering, 68*(4), 1106–1114. https://doi.org/10.1109/TBME.2020.3002077

Sheth, K. N., Mazurek, M. H., Yuen, M. M., Cahn, B. A., Shah, J. T., Ward, A., Kim, J. A., Gilmore, E. J., Falcone, G. J., Petersen, N., Gobeske, K. T., Kaddouh, F., Hwang, D. Y., Schindler, J., Sansing, L., Matouk, C., Rothberg, J., Sze, G., Siner, J., Rosen, M. S., … Kimberly, W. T. (2020). Assessment of Brain Injury Using Portable, Low-Field Magnetic Resonance Imaging at the Bedside of Critically Ill Patients. *JAMA neurology, 78*(1), 41–47. Advance online publication. https://doi.org/10.1001/jamaneurol.2020.3263

Smith, S. M., & Nichols, T. E. (2018). Statistical Challenges in "Big Data" Human Neuroimaging. *Neuron, 97*(2), 263–268. https://doi.org/10.1016/j.neuron.2017.12.018

Srinivas, S. A. (2023). *Gradient-Free Low-Field MRI using the Bloch-Siegert Shift for RF Spatial Encoding*. [Doctoral dissertation, Vanderbilt University]

Srinivas, S. A., Cauley, S. F., Stockmann, J. P., Sappo, C. R., Vaughn, C. E., Wald, L. L., Grissom, W. A., & Cooley, C. Z. (2022). External Dynamic InTerference Estimation and Removal (EDITER) for low field MRI. *Magnetic resonance in medicine, 87*(2), 614–628. https://doi.org/10.1002/mrm.28992

Srinivas S. A., Griswold M. A., Grissom W. A. (2023). RF Frequency-Encoded MRI Using the Bloch Siegert Shift. *I2i Workshop*.

Srinivas S. A., Vaughn C. E., Martin J. B., and Grissom W. A. (2022). EMI-Suppressed Gradient-Free Phase-Encoded Imaging at 47.5mT Using an Optimized Square-Root Solenoid for Encoding and a Saddle Coil for Imaging. In *ISMRM,* pages 0062-0062.

Stockmann, J. P., & Wald, L. L. (2018). In vivo B0 field shimming methods for MRI at 7T. *NeuroImage, 168*, 71–87. https://doi.org/10.1016/j.neuroimage.2017.06.013

Straney D., Cooley C. Z., and Rosen M. S. (2021). An Improved Power Handling Active Transmit/Receive Switch for Low Field MRI using Reed Relays. In *ISMRM,* pages 1395-1395.

Thiim, K. R., Singh, E., Mukundan, S., Grant, P. E., Yang, E., El-Dib, M., & Inder, T. E. (2022). Clinical experience with an in-NICU magnetic resonance imaging system. *Journal of perinatology : official journal of the California Perinatal Association, 42*(7), 873–879. https://doi.org/10.1038/s41372-022-01387-5

Torres, E., Froelich, T., Wang, P., DelaBarre, L., Mullen, M., Adriany, G., Pizetta, D. C., Martins, M. J., Vidoto, E. L. G., Tannús, A., & Garwood, M. (2022). B1 -gradient-based MRI using frequency-modulated Rabi-encoded echoes. *Magnetic resonance in medicine, 87*(2), 674–685. https://doi.org/10.1002/mrm.29002

Tullman M. J. (2013). Overview of the epidemiology, diagnosis, and disease progression associated with multiple sclerosis. *The American journal of managed care, 19*(2 Suppl), S15–S20.

Watchmaker J. M., Xia D., Dayan E., Corcuera-Solano I., Ngeow J. E., By S. T., Chen G., Kaye E., Pitts J., O'Halloran R., Fayad Z. A., Huang M., and Feng L. (2022). Portable, Low-Field MRI for Evaluation of the Knee Joint. In *ISMRM,* pages 1689-1689.

Webb, A.G. and Collins, C.M. (2010), Parallel transmit and receive technology in high-field magnetic resonance neuroimaging. *Int. J. Imaging Syst. Technol., 20*: 2-13. https://doi.org/10.1002/ima.20219

Whitworth, M., Bricker, L., & Mullan, C. (2015). Ultrasound for fetal assessment in early pregnancy. *The Cochrane database of systematic reviews, 2015*(7), CD007058. https://doi.org/10.1002/14651858.CD007058.pub3

Whelan, B., Kolling, S., Oborn, B. M., & Keall, P. (2018). Passive magnetic shielding in MRI-Linac systems. *Physics in medicine and biology, 63*(7), 075008. https://doi.org/10.1088/1361-6560/aab138

Wilcox M. , Srinivas S. A., Vaughn C. E., Sappo C. R., and Grissom W. A. (2021). A Linear Gradient Solenoid for Slice-Selective Brain Imaging using B1+-Selective RF Pulses. In *ISMRM*, pages 4035-4035.

Wood, J. R., Pedersen, R. C., & Rooks, V. J. (2021). Neuroimaging for the Primary Care Provider: A Review of Modalities, Indications, and Pitfalls. *Pediatric clinics of North America, 68*(4), 715–725. https://doi.org/10.1016/j.pcl.2021.04.014

Wright, S. M., & McDougall, M. P. (2009). Single echo acquisition MRI using RF encoding. *NMR in biomedicine, 22*(9), 982–993. https://doi.org/10.1002/nbm.1399

Zaccagna, F., Grist, J. T., Deen, S. S., Woitek, R., Lechermann, L. M., McLean, M. A., Basu, B., & Gallagher, F. A. (2018). Hyperpolarized carbon-13 magnetic resonance spectroscopic imaging: a clinical tool for studying tumour metabolism. *The British journal of radiology, 91*(1085), 20170688. https://doi.org/10.1259/bjr.20170688

Zhu, B., Liu, J. Z., Cauley, S. F., Rosen, B. R., & Rosen, M. S. (2018). Image reconstruction by domain-transform manifold learning. *Nature, 555*(7697), 487–492. https://doi.org/10.1038/nature25988